UNIVERSITY OF LONDON THESIS

Degree PhD Year 2006 Name of Author COTTESWORTH, William Robert

Calcium Signals in the Cell Bodies of Avian Neurones

William Robert Coatesworth

A thesis submitted for the degree of

Doctor of Philosophy

In the

University of London

Department of Physiology

University College London

2005

ProQuest LLC
789 East Eisenhower Parkway
P.O. Box 1346
Ann Arbor, MI 48106-1346

ABSTRACT

In this thesis I have looked at the spatial dynamics of calcium signals in nerve cell bodies. Through this simple second messenger, cells can activate a variety of pathways controlling their growth, secretion and even death. Which pathway is activated depends on the temporal and spatial dynamics of the intracellular calcium signal.

I performed measurements on chick dorsal root ganglion neurones using a combination of whole-cell patch clamping and confocal microscopy. Following a 50 msec depolarisation of the neurone, a resulting calcium influx across the plasma membrane is seen to rapidly diffuse to the centre of the cell within 24 ± 2 msec, contrary to previous studies on the diffusion limit of intracellular calcium. The results from these experiments were modelled as a three-dimensional spatial model, solved via finite volume methods within The Virtual Cell modelling environment. This has allowed me to simulate the intracellular calcium dynamics in an unperturbed cell without the inclusion of the calcium indicator dye to see if the inclusion of this additional calcium buffer was responsible for the observed fast diffusion. From this model I have shown that the experimental technique of including a calcium indicator dye in cells does not adversely affect the spatial and temporal properties of the calcium signal it is intended to observe. Furthermore, predictions made from the model have prompted me to look at role of mitochondria in intracellular calcium regulation, clearly demonstrating that significant levels of calcium are accumulated in these organelles following 50 msec depolarisations.

CONTENTS: **Page:**

LIST OF FIGURES AND TABLES

CHAPTER 6:

CHAPTER 7:

CHAPTER 8:

Figure 8.4 Use of mitochondrial Ca^{2+} uptake to modulate intracellular Ca^{2+} signals

Figure 8.5 Intracellular Ca^{2+} dynamics modulated by mitochondrial Ca^{2+} uptake

APPENDIX B:

Table B1 Model Parameters

ABBREVIATIONS

Ach	acetylcholine
ADP	adenosine 5'-diphosphate
AM	acetoxymethyl
AOTF	acousto-optical tuning filter
ATP	adenosine 5'-triphosphate
BAPTA	1,2-*bis*(2-aminophenoxy)ethane-*N,N,N.,N'*-tetra acetic acid
Ca^{2+}	calcium
Ca^{2+}-ATPase	ATP-dependent Ca^{2+} pump
CaBP	calcium-binding protein
cADPR	cyclic adenosine 5´-diphosphoribose
CaM	calmodulin
CAMK	calmodulin kinase
cAMP	cyclic adenosine 5'-monophosphate
CaR	calcium-sensing receptor
CCCP	carbonyl cyanide *m*-chlorophenylhydrazone
CCK	cholecystokinin
CICR	calcium-induced calcium release
CaB	calbindin-D_{28k}
CBP	CREB binding protein
CLSM	confocal laser scanning microscope
CNS	central nervous system
CREB	cAMP response element binding protein
DAG	diacylglycerol
DMEM	Dubecco's modified Eagles' medium
DMSO	ditmethylsulphoxide
DNA	deoxyribonucleic acid
DR	dynamic range
DRG	dorsal root ganglion
E12	twelve day embryonic
EGTA	ethylene glycol *bis*(beta-aminoethyl ether)-*N,N,N',N'*-tetra acetic acid
ER	endoplasmic reticulum

FCCP	carbonyl cyanide *p*-trifluoromethoxyphenylhydrazone
HBS	HEPES buffered saline
HEPES	N-2 hydroxyethylpiperazine-*N'*-2-ethanesulphonic acid
HVA	high voltage-activated
IP_3	inositol 1,4,5 *tris*phosphate
IP_3R	IP_3 receptor
LP	long-pass
LSM	laser scanning microscope
LVA	low voltage-activated
MAPK	Ras/mitogen-activated protein kinase
Mn^{2+}	magnesium
MTDR	mitotracker deep red
MTG	mitotracker green
Na^+	sodium
NA	numerical aperture
NAADP	nicotinic acid adenine dinucleotide phosphate
NAD^+	nicotinamide adenine dinucleotide
NGF	nerve growth factor
NPC	nuclear pore complex
NTR	nuclear transport receptor
ODE	ordinary differential equation
OG488BD	Oregon Green 488 BAPTA-1 dextran
PBS	phosphate buffered saline
PDE	partial differential equation
PIP_2	phosphatidylinositol-4,5-biphosphate
PKC	protein kinase C
PLC	phospholipase C
PMCA	plasma membrane calcium-ATPase
PMT	photo-multiplier tube
PTH	parathyroid hormone
PTP	permeability transition pore
RaM	rapid uptake mode
Rh123	rhodamine 123
ROCC	receptor-operated calcium channel
ROI	region of interest
RyR	ryanodine receptor
SEM	standard error of the mean
SERCA	sarco- and endoplasmic reticulum Ca^{2+} ATPase
SOCC	store-operated calcium channel
SR	sarcoplasmic reticulum
TCA	tricarboxylic acid
TEA	tetra-ethylamonium
TMRM	tetramethylrhodamine ester
TRITCD	tetramethylrhodamine dextran
TTX	tetrodotoxin
UV	ultra violet

VCMDL	Virtual Cell mathematical description language
VOCC	voltage-operated calcium channel

PREFACE

The modelling environment within which my diffusion models were created was designed at the University of Connecticut Health Center. The patch clamping experiments described in this thesis required the help of an additional person to operate the imaging computer while I performed the patch-clamp experiments. This help was provided by my supervisor Steve Bolsover.

All other work including the creation of models, performing and analysing experiments and writing the thesis were performed by myself under normal supervision.

ACKNOWLEDGEMENTS

I would like to thank Emma whose support, patience and love has helped me through everything.

I would like to thank my parents for their constant support in everything I do. I would like to thank family and friends for their patience.

Steve Bolsover, my supervisor has provided invaluable guidance and help throughout my work and I thank the both the Bolsover and Patel laboratories for both their help through lab meetings and creating an enjoyable working environment.

I would like to thank Sandip Patel who has helped guide my work with insightful comments and ideas.

I would like to thank the MRC for providing the fellowship that supported me throughout my thesis work.

Finally I thank the people at the University of Connecticut Health Center for designing and maintaining the modelling environment The Virtual Cell and answering my questions

1 INTRODUCTION

1.1 Calcium

The importance of calcium (Ca^{2+}) in cells has long been known. In 1883 Sidney Ringer, while studying frog heart muscle, became the first to observe the importance of Ca^{2+} in muscle contraction (Ringer, 1883).

Nowadays, Ca^{2+} is a known as an ubiquitous intracellular messenger controlling a broad range of cellular functions including growth, differentiation and proliferation (Bading *et al.*, 1993; Petersen *et al.*, 1994; Bootman and Berridge, 1995; Clapham, 1995; Berridge *et al.*, 2000). Ca^{2+} is particularly suited to this role for a number of reasons including its ability to penetrate intracellular organelles such as the mitochondria and the nucleus as well as its ability to bind tightly, yet reversibly, to a large range of proteins, so called Ca^{2+}-binding proteins (CaBPs).

1.2 Calcium Signalling

Calcium signalling is one of the major routes through which information at the cell surface is translated to specific cellular processes.

Signals are communicated through rises in cytosolic Ca^{2+} concentrations ($[Ca^{2+}]_c$) enabling Ca^{2+} ions to bind to specific target proteins such as calmodulin which translate the changes in $[Ca^{2+}]_c$ to cellular functions such as gene transcription (Berridge *et al.*, 2000).

Throughout this thesis I will use $[Ca^{2+}]_c$ to refer to cytosolic Ca^{2+} concentrations, $[Ca^{2+}]_n$ to refer to nucleoplasmic Ca^{2+} concentrations and $[Ca^{2+}]_i$ to refer to intracellular Ca^{2+} concentrations, made up of combined cytosolic and nucleoplasmic Ca^{2+} concentrations.

Increases in $[Ca^{2+}]_c$ generally arise from two sources: entry from the extracellular medium through plasma membrane Ca^{2+} channels or release from intracellular Ca^{2+} stores, usually the endoplasmic reticulum (ER) or, in muscle, the sarcoplasmic reticulum (SR) (Berridge *et al.*, 1999). Both of these methods produce localised concentrations of Ca^{2+} which can then diffuse throughout the cytoplasm through a variety of pathways. Inside the cell, the majority of Ca^{2+} is quickly buffered, either by protein-based mobile buffers or by intracellular organelles, such as the endoplasmic reticulum and mitochondria, which I will refer to as Ca^{2+} sinks or non-mobile buffers, leaving only a small proportion of intracellular Ca^{2+} as free Ca^{2+}.

The way Ca^{2+} is used in signalling pathways differs between cell types. Varying the amplitude, frequency, kinetics and spatial patterns of the Ca^{2+} signal allows cells to use

Ca^{2+} to control a wide variety of cellular events to such an extent that within the same cells Ca^{2+} signals control processes as opposed as proliferation and apoptosis (Berridge *et al.*, 1999, 2000; Bootman *et al.*, 2001a).

1.2.1 Elementary Calcium Signals

Local Ca^{2+} signals can be produced by release from intracellular stores through what have been termed elementary events. Named blips, puffs, quarks and sparks depending on whether they are produced from IP_3 receptors (blips and puffs) or ryanodine receptors (quarks and sparks) and whether they result from single channel opening (blips and quarks) or a group of channels (puffs and sparks), these events produce highly localised Ca^{2+} changes providing specific control over many physiological functions (Berridge *et al.*, 1999; Bootman *et al.*, 2001b; Tovey *et al.*, 2001).

These elemental signals can be combined with Ca^{2+} entry across the plasma membrane to produce global effects such as waves and oscillations capable of spreading throughout the cell. The mechanisms and relationships between Ca^{2+} entry and release are cell specific. In non-excitable cells, the primary contribution to Ca^{2+} levels comes from release from intracellular stores. In excitable cells this is combined with Ca^{2+} entry across the plasma membrane.

1.2.2 Nuclear Calcium Signalling

In the nucleus, changes in Ca^{2+} concentration modulate many specific functions such as gene transcription, cell division and apoptosis (Bootman *et al.*, 2001a; Dolmetsch *et al.*, 2001).

Increases in nuclear Ca^{2+} concentration ($[Ca^{2+}]_n$) generally follow from rises of $[Ca^{2+}]_c$ resulting from release from intracellular stores or Ca^{2+} influx across the plasma membrane (Lipp *et al.*, 1997). In addition to this, many neuronal nuclear functions are regulated by proteins such as calmodulin that bind Ca^{2+} from the cytosol before relocating to the nucleus where they are able to activate many nuclear signalling pathways such as the Ras/mitogen-activated protein kinase (MAPK) pathway leading to the transcription of genes essential for neuronal survival and plasticity (Dolmetsch *et al.*, 2001).

Work by Lipp *et al.* using HeLa cells demonstrates the principle of 'nuclear tunnelling', whereby the low buffering capacity of the nucleus allows Ca^{2+} signals propagating through it to diffuse over significantly greater distances enabling them to spread them over larger volumes. Such a phenomenon is observed from Ca^{2+} puffs, elementary Ca^{2+} signals associated with the opening of small groups of IP_3 receptors, originating from intracellular stores in close association with the nuclear envelope, which when compared with puffs originating remote from the nucleus were seen to have their volume and duration increased up to 10-fold (Lipp *et al.*, 1997).

1.2.3 Extracellular Calcium

While most attention has been focused on intracellular Ca^{2+} in cell signalling, recent work has also studied the role of extracellular Ca^{2+}.

The extracellular Ca^{2+} concentration ($[Ca^{2+}]_{ec}$) has been measured at values of 1.25 mM in rat neocortex (Pumain and Heinemann, 1985) and approximately 1.4 mM in blood (Brown and Macloed, 2001). This is closely regulated by 2 hormones; calcitonin acts to lower the Ca^{2+} concentration while parathyroid hormone (PTH) raises it (Schwaller, 2001; Hofer and Brown, 2003).

A variety of cell-surface detectors and ion channels have been found to be sensitive to changes in extracellular Ca^{2+} (Hofer, 2005). These include the well-characterised extracellular-Ca^{2+}-sensing receptor (CaR); a G-protein-coupled receptor found in a variety of cell types in the peripheral and central nervous system, glial cells and epithelial cells throughout a range of organisms (Brown and Macloed, 2001). This receptor conveys information about the local extracellular Ca^{2+} concentration to the interior of the cell. Elevation of $[Ca^{2+}]_{ec}$ activates the associated G-protein structure on the interior side of the plasma membrane and hence the IP_3 pathway, described later in more detail.

1.3 Calcium Signalling in Neurones

Nearly all neuronal functions are regulated, either directly or indirectly, by Ca^{2+}. These functions range from gene expression to neuronal growth and even apoptosis (Augustine *et al.*, 2003). The neuronal Ca^{2+} signals generally occur in response to an external stimulus, be it depolarisation, causing the entry of Ca^{2+} across the plasma membrane through Ca^{2+}-permeable channels, or stimulation of a receptor by an extracellular agonist either opening a plasma membrane Ca^{2+} channel or activating a pathway leading to the release of Ca^{2+} from intracellular Ca^{2+} stores. These events create spatial Ca^{2+} gradients which then dissipate into the cytoplasm. The free Ca^{2+} ions bind to a range of intracellular Ca^{2+} sensors communicating the increase in $[Ca^{2+}]_c$ into neuronal processes.

1.4 Calcium Entry Pathways and Removal Systems

Which cellular systems are activated by the initial increase in $[Ca^{2+}]_c$ depends on the origin of the Ca^{2+} signal, the shape of the Ca^{2+} transients, as determined by the spatial and temporal variations in the Ca^{2+} influx or release, and how the increase in $[Ca^{2+}]_c$ is dealt with once inside the cell. This can include uptake into intracellular organelles, binding to Ca^{2+}-binding proteins inside the cell or extrusion from the cell across the plasma membrane via Ca^{2+} pumps such as the Ca^{2+}-ATPase or the Na^+ / Ca^{2+} exchanger which use ATP or the sodium gradient across the plasma membrane respectively to actively pump Ca^{2+} out of the cell.

1.4.1 Calcium Release from Intracellular Stores

Calcium is released from intracellular stores via various second messenger-activated Ca^{2+} channels either in response to an external agonist or as a result of already raised cytosolic Ca^{2+} levels.

Major intracellular messengers that increase $[Ca^{2+}]_c$ include inositol 1,4,5-triphosphate (IP_3), cyclic adenosine 5´-diphosphoribose (cADPR), nicotinic acid adenine dinucleotide phosphate (NAADP), and Ca^{2+} itself (Berridge, 1993; Petersen and Cancela, 1999; Bootman *et al.*, 2002). At present only two types of intracellular release channels have been identified, both of which mobilise Ca^{2+} from the ER; the IP_3 receptor (IP_3R), activated by IP_3 and the ryanodine receptor (RyR), activated by cADPR and Ca^{2+}. NAADP has been shown to act through a separate, as yet uncharacterised, channel located on the lysosomes (Churchill *et al.*, 2002).

A standard signalling pathway involves the activation of a G-protein associated with a plasma membrane receptor. The subsequent interactions between this G-protein and phospholipase C (PLC) results in the hydrolysis of phosphatidylinositol-4,5-biphosphate (PIP_2) to form inositol-1,4,5-trisphosphate (IP_3) and diacylglycerol (DAG). The second messenger, IP_3, can then initiate a well defined intracellular Ca^{2+} signalling pathway, releasing Ca^{2+} from the ER, while DAG remains at the plasma membrane where it can phosphorylate protein kinase C (PKC) which plays a crucial role in many signal transduction pathways (Hilgemann *et al.*, 2001; Hofer and Brown, 2003).

It has been shown in pancreatic acinar cells that which second messengers are involved in translating an agonist-induced Ca^{2+} spike into a global Ca^{2+} signal by releasing Ca^{2+} from intracellular stores depends on the initial extracellular agonist. By measuring the spread of the Ca^{2+} spikes in the presence of various second messengers, it was determined that spikes induced by acetylcholine (ACh) can be transformed into global signals by cADPR or NAADP with IP_3 having little effect. In converse experiments, for Ca^{2+} spikes initiated by stimulation with cholecystokinin (CCK), IP_3 globalises the Ca^{2+} signal, whereas cADPR and NAADP have little effect. One possible explanation for this is that ACh recruits cADPR and NAADP as Ca^{2+} mobilising messengers, while CCK recruits IP_3. The same study shows that by using combinations of IP_3, cADPR and NAADP it is possible to reconstruct the assortment of local and global Ca^{2+} responses to physiological stimuli (Cancela *et al.*, 2002).

Although often over shadowed by the ER, evidence has suggested that the Golgi apparatus may also function as an Ca^{2+} store, separate from the ER, with a high-affinity SERCA pump capable of accumulating both Ca^{2+} and manganese (Mn^{2+}) and a Ca^{2+} release channel modulated by IP_3 (Pinton *et al.*, 1998b; Dolman *et al.*, 2005).

1.4.1.1 Calcium-Induced Calcium Release

Calcium-induced calcium release (CICR) is the process through which elevations of $[Ca^{2+}]_c$ cause the release of further Ca^{2+} from intracellular stores. This has been shown to amplify Ca^{2+} signals in a variety of cell types (Holliday *et al.*, 1991; Friel and Tsien, 1992; Usachev *et al.*, 1993b; Llano *et al.*, 1994; Berridge, 1998; Albrecht *et al.*, 2001). A number of studies have demonstrated that CICR releases Ca^{2+} from the endoplasmic reticulum (ER) via activation of ryanodine receptors (RyRs) (Hongpaisan *et al.*, 2001).

1.4.1.1.1 The Endoplasmic Reticulum

The endoplasmic reticulum (ER) is a continuous structure expressed abundantly throughout the cytoplasm of neurones, acting as both a Ca^{2+} sink for Ca^{2+} entering the cell across the plasma membrane and a Ca^{2+} source releasing Ca^{2+} into the cytosol in response to intracellular messengers such as IP_3 and cADPR (Friel and Tsien, 1992; Verkhratsky and Shmigol, 1996; Petersen *et al.*, 2001).

Ca^{2+} release from the ER is mediated via two, Ca^{2+}-activated, Ca^{2+} release channels; the IP_3 receptor (IP_3R) and the ryanodine receptor (RyR). These are also activated by IP_3 and cADPR respectively.

Ca^{2+}-dependent activation of ER receptors through CICR serves to amplify depolarisation-induced $[Ca^{2+}]_c$ increases. The RyRs have been shown to be reversibly sensitised by the application of caffeine, reducing the concentration of $[Ca^{2+}]_c$ required

for activation (Friel and Tsien, 1992; Albrecht *et al.*, 2001) while application of low concentrations of the plant alkaloid ryanodine (≤ 1 μM) locks the receptors into a subconductance state, reducing the basal level of the ER Ca^{2+} stores and preventing CICR. At much larger concentrations (> 100 μM), ryanodine has been shown to completely block the channels (Friel and Tsien, 1992; Albrecht *et al.*, 2001).

Release from the ER can also occur through agonist binding to extracellular receptors on the plasma membrane. This can activate a G-protein coupled to the receptor, producing IP_3 and DAG through a previously described pathway. While DAG can activate protein kinase C (PKC), IP_3 rapidly diffuses through the cytoplasm to the ER, binding to IP_3 receptors (IP_3Rs) and changing the conformational shape of the receptor such that a channel is opened allowing Ca^{2+} to pass from the ER to the cytoplasm (Bootman *et al.*, 2001a).

Uptake into the ER is regulated by sarco- and endoplasmic reticulum Ca^{2+} ATPase (SERCA) pumps, which transport two Ca^{2+} ions for every hydrolysed molecule of ATP (Carafoli, 2003). At resting $[Ca^{2+}]_c$, SERCA uptake is balanced by passive Ca^{2+} release maintaining ER Ca^{2+} at basal levels (Albrecht *et al.*, 2001). Uptake through these pumps has been shown to increase linearly with increasing $[Ca^{2+}]_c$, helping clear large cytosolic Ca^{2+} loads (Lytton *et al.*, 1992; Wanaverbecq *et al.*, 2003), although at high $[Ca^{2+}]_c$, Ca^{2+}-sensitive CICR operates in parallel with this ER uptake, effectively weakening the Ca^{2+} accumulation into the ER (Albrecht et al., 2001).

The SERCA Ca^{2+} uptake is inhibited by thapsigargin; initially discharging the ER calcium into the cytoplasm and preventing further uptake (Holliday *et al.*, 1991; Shmigol

et al., 1995a; Verkhratsky and Shmigol, 1996; Albrecht *et al.*, 2001; Hongpaisan *et al.*, 2001).

1.4.1.1.2 Calcium-Induced Calcium Release in Neurones

CICR has been shown to be present in many excitable cell types, where it is thought to amplify depolarisation-induced Ca^{2+} influxes via net Ca^{2+} release from the ER (Friel and Tsien, 1992; Shmigol *et al.*, 1995b; Albrecht *et al.*, 2001).

Studies in sympathetic neurones by Albrecht *et al.* and Hongpaisan *et al.* have shown that the net result of CICR depends on the magnitude of the $[Ca^{2+}]_c$ changes and does not always result in a rise in $[Ca^{2+}]_c$; such that while even small cytosolic Ca^{2+} changes (less than ~ 350 nM) are capable of inducing Ca^{2+} release from the ER this is masked by a more rapid uptake into the organelle.

Thus for small changes in $[Ca^{2+}]_c$, induced by weak depolarisations, the ER acts as a Ca^{2+} sink, accumulating Ca^{2+} from the cytosol at a faster rate than it is released by CICR. This accumulation becomes weaker as the Ca^{2+} changes become larger such that at large changes in $[Ca^{2+}]_c$ the ER acts as a Ca^{2+} source, releasing its stored Ca^{2+} through CICR. These effects have been classified into three distinct modes of CICR by Albrecht *et al.*.

Mode 1 results from weak depolarisations which cause small changes in $[Ca^{2+}]_c$ (< ~350 nM). In this situation the passive Ca^{2+} release from the ER is found to be slower than the Ca^{2+} uptake, resulting in a net flow of Ca^{2+} into the ER which acts as a Ca^{2+} sink. At larger changes in $[Ca^{2+}]_c$ (~ 700 nM) the passive Ca^{2+} release from the ER becomes

faster than the uptake. This causes a net release of Ca^{2+} from the ER into the cytoplasm further increasing the rate at which the depolarisation-induced $[Ca^{2+}]_c$ rises via mode 2 CICR. Mode 3 CICR is caused by even larger changes of $[Ca^{2+}]_c$ (>1 μM) which cause ER Ca^{2+} releases at a rate much greater than that of the Ca^{2+} extrusion systems leading to a regenerative rise in $[Ca^{2+}]_c$ (Albrecht *et al.*, 2001; Hongpaisan *et al.*, 2001). The spatial variations in $[Ca^{2+}]_c$ immediately after depolarisation mean that while the global averaged $[Ca^{2+}]_c$ may only rise to levels promoting mode 1 or 2 CICR, the sub-population of ER located under the plasma membrane are exposed to much higher levels of $[Ca^{2+}]_c$ moving them to mode 3 CICR helping to drive the Ca^{2+} signal into the cell.

While this has not been demonstrated in sensory neurones, it seems likely that similar phenomena would exist.

1.4.1.1.3 Calcium Waves Driven by Calcium-Induced Calcium Release

The ER has been shown to participate in the propagation of Ca^{2+} waves through CICR in a number of cell types (Ashby *et al.*, 2002). These waves can spread throughout the cell, globalising the Ca^{2+} signal.

The speeds of these Ca^{2+} waves vary between cell types. In hepatocytes Ca^{2+} waves have been shown to travel at speeds of between 50 – 62 μm s^{-1} (Nathanson *et al.*, 1994), almost ten times faster than the speeds of 4.2 – 8.6 μm s^{-1} seen in smooth muscle cells (Mahoney *et al.*, 1993). In neurones, Ca^{2+} waves have been observed travelling with typical speeds measured around 50 μm s^{-1} (McDonough *et al.*, 2000).

Even with the fastest of these propagation speeds, it would take almost 200 msecs for the Ca^{2+} signal to travel to the centre of a cell with a diameter of 20 μm.

1.4.2 Plasma Membrane Calcium Channels

As a charged ion, Ca^{2+} is unable to cross the lipid membrane surrounding the cell, and so protein structures are required to transport Ca^{2+} ions from the relatively inexhaustible supply in the extracellular space. These protein structures, Ca^{2+} channels, include complex gating mechanisms to control the flow of Ca^{2+} into the cytosol down its electrochemical gradient. As such, the channels have a low probability of opening while the cell is at rest, but when the cell is stimulated, the probability of the channels activating increases allowing Ca^{2+} to pass into the cytosolic space.

There are a wide variety of Ca^{2+} channels, categorised by their activation mechanism. These include receptor-operated Ca^{2+} channels (ROCCs), activated by the binding of a specific agonist such as glutamate, ATP or acetylcholine to the extracellular domain of the channel; store-operated Ca^{2+} channels (SOCCs), activated in response to the depletion of intracellular Ca^{2+} stores; mechanically-activated Ca^{2+} channels, activated by the stimulation of mechano-receptors in response to cell deformation and voltage-operated Ca^{2+} channels (VOCCs), activated by depolarisation of the plasma membrane (Barritt, 1999; Berridge *et al.*, 2000).

1.4.2.1 Voltage-Operated Calcium Channels

These are at least ten types of voltage-operated Ca^{2+} channels expressed in neurones, essential for converting electrical activity at the cell membrane into biochemical events (Berridge, 1998; Catterall, 2000). Normally found closed at resting membrane potentials, these channels open in response to depolarisations of the plasma membrane allowing Ca^{2+} to move from the extracellular space into the cytoplasm down its concentration gradient. The various channels exhibit nearly perfect selectivity for Ca^{2+} over sodium despite extracellular sodium concentration being more than 50 times that of extracellular Ca^{2+}. It has been shown that in the absence of extracellular Ca^{2+}, the channels become highly permeable to sodium. This is due to a high-affinity Ca^{2+} binding site on the channel that when Ca^{2+}-bound blocks the flow of sodium ions conferring selectivity. The various subtypes of VOCCs are identified by their different electrical and pharmacological properties, while their different locations and opening kinetics allow for a wide variety of signalling pathways necessary to accommodate the numerous cellular responses triggered by changes in $[Ca^{2+}]_c$ (Diochot *et al.*, 1995; Desmadryl *et al.*, 1997; Augustine *et al.*, 2003).

Voltage-activated Ca^{2+} channels are divided into two groups, High voltage-activated (HVA) channels and low voltage-activated (LVA) channels, depending on the voltage threshold for channel activation (Lacinova and Hofmann, 2005). Within these groups the channels are further subdivided. HVA channels include L-type channels, characterised by their long-lasting (L) currents; N-type channels which are selectively blocked by the peptide toxin ω-conotoxin GVIA; P-type channels, prevalent in cerebellar Purkinje (P)

neurones and which are highly sensitive to the peptide toxin ω-Aga-IVA and Q-type channels, closely related to P-types but with a slightly lower affinity to ω-Aga-IVA. LVA channels consist of various subtypes of T-type channels characterised by currents that are transient and have tiny (T) single channel currents (Bean, 2001).

In sensory neurones, depolarisation-induced Ca^{2+} entry primarily occurs via L- and N-type Ca^{2+} channels found in the cell body and dendrites (Nowycky *et al.*, 1985; Fox *et al.*, 1987b, a). These are normally closed at plasma membrane resting voltages of -80 or -70 mV and maximally opened at voltages around +10 mV as experienced through action potentials. Ca^{2+} entering though these channels can activate signalling pathways targeted at the nucleus such as the activation of the transcription factor cyclic adenosine monophosphate response element binding protein (CREB) which drives the expression of a number of genes regulating neuronal plasticity and survival (Shaywitz and Greenberg, 1999; Dolmetsch et al., 2001).

When exposed to prolonged depolarisation, L- and N-type channels display voltage-dependent inactivation causing the current to decline. The speed of this inactivation varies between cell types, typically occurring with half-times of hundreds of milliseconds to seconds. In L-type channels, inactivation can also be triggered via a negative feedback mechanism. Ca^{2+} entering through the channels can bind to the Ca^{2+}-binding protein calmodulin. This can then go on bind to the channel allowing it to interact with the Ca^{2+} channel α1 subunit causing channel inactivation (Zühlke *et al.*, 1999; Dolmetsch *et al.*, 2001; Lacinova and Hofmann, 2005).

1.4.2.1.1 L-type Calcium Channels

L-type Ca^{2+} channels are part of large family of high-voltage activated channels, activated by large depolarisations of the plasma membrane. The L-type channel is identified by its long-lasting (L) current and relatively slow inactivation, as well as its sensitivity to a number of Ca^{2+} channel agonists such as nifedipine or nitrendipine (Diochot *et al.*, 1995; Dolphin, 2001; Heinemann, 2001).

The specificity of L-type channels for nuclear signalling may come from their ability to use calmodulin (CaM), a well-characterised Ca^{2+}-binding protein modulating many important Ca^{2+}-dependent enzymes and signalling pathways (Solà et al., 2001). As described previously, once bound to Ca^{2+}, CaM can bind to the channel causing Ca^{2+}-dependent inactivation. This binding can also activate the Ras/mitogen-activated protein kinase (MAPK) pathway which conveys the local Ca^{2+} signal at the mouth of the channel to the nucleus. This signalling pathway participates in the activation of cAMP response element binding protein (CREB) mentioned previously (Dolmetsch *et al.*, 2001; Redmond and Ghosh, 2005).

1.4.2.1.2 N-Type Calcium Channels

Another type of high-voltage activated Ca^{2+} channel, the N-type Ca^{2+} channel is predominantly located in the nervous system where it is thought to have a specific developmental role in the migration of immature neurones before the establishment of

their synaptic circuits, as well as being involved in the release of neurotransmitters such as glutamate in mammalian central neurones (Luebke *et al.*, 1993; Desmadryl *et al.*, 1998).

The N-type channels are selectively blocked by ω-conotoxin GVIA but are resistant to L-type Ca^{2+} channel-specific blockers.

1.4.3 Uptake of Intracellular Calcium into Calcium Sinks

Following repolarisation, the intracellular Ca^{2+} concentration ($[Ca^{2+}]_i$) rapidly recovers to resting levels. This occurs through a variety of uptake and extrusion systems. Ca^{2+} can be removed from the cell to the extracellular medium by plasma membrane Ca^{2+}-ATPase (PMCA) pumps and Na+ / Ca^{2+} exchangers or taken up into the ER by the sarco-endoplasmic reticulum ATPase (SERCA). The two pumps hydrolyse ATP to ADP to provide the energy required to pump Ca^{2+} out of the cytoplasm against its concentration gradient. The exchanger on the other hand uses the electrochemical gradient of sodium as a driving force to remove Ca^{2+} from the cytoplasm.

The mitochondria also play an important role in the regulation of $[Ca^{2+}]_i$; taking up Ca^{2+} during the development of the Ca^{2+} signal, before releasing it slowly back into the cytosol via the Na^+ / Ca^{2+} exchanger after $[Ca^{2+}]_i$ begins to fall. This uptake and release system serves two purposes, initially accelerating the recovery from large Ca^{2+} transients through its high uptake before slowing the eventual recovery of $[Ca^{2+}]_i$ to resting levels (Colegrove *et al.*, 2000; Wanaverbecq *et al.*, 2003).

Studies on bullfrog sympathetic neurones have suggested a pattern of Ca^{2+} movement in which the extrusion of mitochondrial Ca^{2+} holds $[Ca^{2+}]_i$ at ~200 – 300 nM for a period, during which time Ca^{2+} is accumulated from the cytosol into the endoplasmic reticulum (ER). Subsequent ER Ca^{2+} levels can remain elevated for up to 15 minutes before slowly releasing into the cytoplasm creating a prolonged phase of recovery. It has been proposed that such long recoveries to basal levels in the ER and by consequence in the cytoplasm may provide a memory mechanism for Ca^{2+} activity suitable for processes such as protein synthesis and transport (Friel, 1995; Hongpaisan *et al.*, 2001).

Work done by Wanaverbecq *et al.* on rat superior cervical ganglion concluded that the contributions to intracellular Ca^{2+} regulation from non-mobile buffering systems were strongly dependent on the size of the intracellular Ca^{2+} changes. For small increases in $[Ca^{2+}]_i$ (< 500 nM), resulting from depolarisations of 60 msec from the resting voltage to 0 mV, the plasma membrane Ca^{2+}-ATPase (PMCA) was found to be the main contributor in returning the $[Ca^{2+}]_i$ to resting levels, whereas the other Ca^{2+} extrusion and uptake systems such as the Na^+ / Ca^{2+} exchanger and the endoplasmic reticulum Ca^{2+} uptake system were found to contribute very little to the clearance of the small Ca^{2+} transients. However, for larger Ca^{2+} transients, where $[Ca^{2+}]_i$ is increased to levels > 500nM, while recovery to resting Ca^{2+} levels continued to be strongly dependent on the PMCA, additional contributions from the Na^+ / Ca^{2+} exchanger and SERCA systems were seen as well as uptake into the mitochondria (Wanaverbecq *et al.*, 2003).

1.5 Calcium Buffering

As well as fixed buffers such as those mentioned in the preceding sections, neurones also contain a wide variety of mobile, protein-based buffers that rapidly bind Ca^{2+} entering the cytoplasm. These buffers are heavily responsible for shaping the spatial and temporal properties of the Ca^{2+} signal.

The buffering capacity of each cell, given by the number of Ca^{2+} ions that are bound to buffers for each ion of free Ca^{2+}, varies significantly between cells (Berridge *et al.*, 2000).

1.5.1 Calcium-Binding Proteins

Calcium-binding proteins provide a large variety of Ca^{2+}-buffers which modulate the spatial and temporal properties of the Ca^{2+} signals and Ca^{2+} sensors responsible for translating changes in $[Ca^{2+}]_i$ to a range of cellular functions.

The various Ca^{2+}-binding proteins, including Ca^{2+} buffers such as parvalbumin or calbindin-D_{28K} and Ca^{2+} sensors such as calmodulin, have different affinities and binding kinetics for Ca^{2+}, fine-tuned to exert their specific biological function.

1.5.1.1 Calmodulin

Calmodulin (CaM) is identified as one of the most common of the Ca^{2+}-binding proteins, present in all eukaryotic cells where it is found throughout the cytosol and the nucleus as well as associated with membranes and a variety of proteins including those comprising the structure of L-type Ca^{2+} channels. CaM acts as a Ca^{2+} sensor with two pairs of EF-hands, capable of binding up to four molecules of Ca^{2+}. This results in a pronounced conformational change enabling CaM to activate a large array of cellular functions, including cell growth, cell division and gene transcription (Putney, 1998; Solà et al., 2001; Milikan et al., 2002).

It has been shown that in response to depolarisation, calmodulin translocates to the nucleus of neurones within 15 secs. (Deisseroth *et al.*, 1998; Mermelstein *et al.*, 2001).

Calmodulin also plays a key role in the regulation of Ca^{2+} channels by coupling increases in $[Ca^{2+}]_c$ to changes in the activity of many enzymes and ion channels (Chin and Means, 2000).

1.5.1.2 Calbindin-D_{28k}

Calbindin-D_{28k} (CaB) is a Ca^{2+}-binding protein found throughout the central nervous system (CNS) as well as in non-neuronal tissue. A single protein molecule consists of six EF-hand motifs, four of which are found to bind Ca^{2+}. CaB has been shown to be a major

endogenous buffer in a variety of situations ranging from the single synapse level to whole cells such as hippocampal mossy fibres. CaB acts as a mobile Ca^{2+} buffer, binding Ca^{2+} entering the cytoplasm across the plasma membrane, shaping the spatiotemporal extent of cellular Ca^{2+} signals. It has further been proposed that CaB may act to protect neurones against excessive influxes of Ca^{2+} as well as being involved in aspects of pain transmission in some neurones (Li *et al.*, 2005).

1.5.1.3 CREB

Cyclic adenosine monophosphate (cAMP) response element binding protein (CREB) is a nuclear Ca^{2+}-responsive transcription factor, constitutively bound to DNA, which drives the expression of a number of genes that regulate neuronal survival and plasticity (Shaywitz and Greenberg, 1999; Redmond and Ghosh, 2005).

CREB can be activated by many pathways including phosphorylation by CaM kinases CAMKII and CAMKIV at Ser133, Ser142 and Ser143 or the previously described MAPK pathway. Activation permits it to bind the CREB binding protein (CBP), initiating transcription.

1.6 Basic Calcium Diffusion

The laws governing the movement of Ca^{2+} in cells are primarily those of diffusion. With the exception of locations where active pumps are involved, such as the plasma membrane and ER ATP-ases, the net Ca^{2+} flow is in directions dictated by its concentration gradient; that is from areas of high [Ca^{2+}] to those of lower [Ca^{2+}]. In this way, increases in $[Ca^{2+}]_c$ originating at Ca^{2+} release sites and at the mouths of plasma membrane Ca^{2+} channels are rapidly dispersed throughout the cytosol and nucleus of the cell.

In free solution, the diffusion of Ca^{2+} ions has been measured as 792 $\mu m^2 s^{-1}$ (Winslow *et al.*, 1994). At this diffusion speed, it would take the free Ca^{2+} ions under 1 msec to travel from the plasma membrane to the centre of a cell with a diameter of 20 μm. In cellular structures, the diffusion would be expected to be slower because steric hindrance and viscosity.

1.7 Nuclear Envelope

The nucleus is isolated from the cytoplasm by two lipid bilayer membranes called the nuclear envelope.

Transport between the cytoplasm and the nucleus occurs via nuclear pore complexes (NPCs). These are supramolecular assemblies, with masses of the order of 125 x 10^3 kD, that span the nuclear envelope (Wang and Clapham, 1999).

The NPC consists of a ring of aqueous channels, thought to allow passive diffusion of molecules with masses less than ~20 – 40 kD, surrounding a central granule allowing signal-mediated transport of larger proteins (Greber and Gerace, 1995; Wang and Clapham, 1999). Many proteins contain a nuclear localisation sequence that aids their translocation from the cytoplasm into the nucleus. This sequence allows the protein to bind to nuclear transport receptors (NTRs) that are capable of travelling through the NPC at very high rates (Ribbeck and Gorlich, 2001). Once inside the nucleus, the protein is dissociated from the NTR by interaction with RanGTP. A similar pathway speeds up the export of specific proteins from the nucleus. Proteins with a nuclear export sequence can form complexes with both a NTR and RanGTP. Once in the cytoplasm this complex is dissociated by hydrolysis of the RanGTP (Peters, 2005).

Many experiments have suggested that the nuclear pores are freely permeable to Ca^{2+} and other ions, allowing changes in $[Ca^{2+}]_c$ to rapidly propagate into the nucleus via passive diffusion (Gerasimenko *et al.*, 1996; Lipp *et al.*, 1997).

Some studies, such as those on HeLa cells, show changes in nuclear Ca^{2+} occuring rapidly after those in the cytosol as expected by free diffusion. However, there are also reports indicating that the nuclear envelope acts as a significant barrier to Ca^{2+} diffusion either slowing down the diffusion of Ca^{2+} into the nucleus, in the case of rat sensory neurones (al-Mohanna *et al.*, 1994; Zimprich *et al.*, 1995) or, in the case of HeLa cells, completely isolating the nucleus from cytoplasmic Ca^{2+} changes (Badminton *et al.*, 1995; Badminton *et al.*, 1996b). No studies indicating the extent to which the nuclear envelope

presents a barrier to diffusion have been made on chick sensory neurones which are the subject of my experiments.

The outer nuclear membrane is continuous with the surrounding ER such that the nuclear intermembrane space is continuous with the lumen of the ER. Studies in HeLa and NRK cells have suggested that the nuclear envelope becomes a greater barrier to both passive diffusion and signal-mediated transport when the ER is depleted of Ca^{2+} by ionomycin or thapsigargin (Greber and Gerace, 1995). However, work by Strübing and Clapham studying human embryonic kidney cells find that only passive diffusion and not active is blocked in such cases while later work in COS7 cells from the same laboratory has found no direct evidence linking depletion of luminal Ca^{2+} stores with gating of the nuclear pores (Strübing and Clapham, 1999; Wei *et al.*, 2003).

It has been shown that the nuclear envelope also acts as a Ca^{2+} store and that both IP_3 and ryanodine receptors are found on the inner nuclear envelope raising the view that nuclear Ca^{2+} concentration ($[Ca^{2+}]_n$) can be raised independently of $[Ca^{2+}]_c$ (Gerasimenko *et al.*, 1995). Recent evidence has been presented in a range of neurones suggesting that IP_3 receptors can be activated through the interaction of a family of EF-hand Ca^{2+}-binding proteins, CaBP1, independently of IP_3 production (Yang *et al.*, 2002; Haynes *et al.*, 2004). Although the work has focused on IP_3 receptors found on the ER, if correct this raises the possibility that nuclear IP_3 receptors could be activated in the same way. This, coupled with evidence that the nucleus has the ability to generate IP_3, further promotes the view that the nucleus can control its Ca^{2+} levels independently of the cytosol.

It has been postulated that the origin of the nuclear Ca^{2+} signal, be it diffusion from the cytoplasm or release from the nuclear envelope, may have differing effects on nuclear functions (Hardingham *et al.*, 1997).

1.8 Mitochondria

The ability of mitochondria to accumulate Ca^{2+} was first identified in the 1960s (Rossi *et al.*, 1967; Dhalla, 1969; Harris and Berent, 1969; Lehninger, 1969), although it took over two decades for the effects of this uptake into the mitochondria on Ca^{2+} signalling to be investigated (Thayer and Miller, 1990). This, along with other studies, showed that the mitochondria are capable of accumulating very large amounts of Ca^{2+} from the cytosol leading to enhanced rates of ATP synthesis. More recently, it has been shown that mitochondria in secretory cells directly modulate both local and global agonist-induced Ca^{2+} signals (Johnson *et al.*, 2002).

In sensory neurones, experiments have demonstrated that the rate of Ca^{2+} clearance can be altered by using mitochondrial uncouplers, such as carbonyl cyanide *m*-chlorophenylhydrazone (CCCP) or carbonyl cyanide *p*-trifluoromethoxyphenylhydrazone (FCCP), to depolarise the mitochondrial membrane and inhibit mitochondrial Ca^{2+} uptake. Despite this, the low affinity of mitochondria for Ca^{2+} led many to conclude that under physiological Ca^{2+} changes the ER would be primarily responsible for intracellular Ca^{2+} uptake, leaving the mitochondria to buffer high changes in $[Ca^{2+}]_c$.

However, more recent work has shown specific spatial localisation of the mitochondria around Ca^{2+} entry and Ca^{2+} release sites where they can act as immobile sinks delaying the diffusion of the Ca^{2+} signal to the rest of the cell (Pinton *et al.*, 1998a; Tinel *et al.*, 1999). These points create microdomains of high $[Ca^{2+}]_c$ which are then buffered into the mitochondrial matrices.

In addition to exposure to local, high concentrations of Ca^{2+}, the position of mitochondria in cells provides significant physiological functions in restricting the spread of Ca^{2+}. In pancreatic acinar cells, the majority of mitochondria act as a barrier helping to prevent the spread of IP_3-induced Ca^{2+} release in the apical pole containing the secretory granules spreading into the basolateral region containing the nucleus. These mitochondrial barriers confine agonist-induced Ca^{2+} spikes to the apical pole where they act upon the Ca^{2+}-sensitive chloride channels clustered in the luminal (apical) membrane. The activation of these channels is required for these cells to secrete both fluid and enzymes into the lumen(Tinel *et al.*, 1999).

1.8.1 Mitochondrial Calcium Uptake and Release Mechanisms

Calcium is taken up into the mitochondria following increases in $[Ca^{2+}]_c$ and released back into the cytoplasm over a period of minutes. Ca^{2+} uptake is mediated via an as yet unidentified high-capacity, low-affinity uniporter, which is activated by elevated $[Ca^{2+}]_c$ and driven by the large electrical potential generated by the large negative voltage of the inner mitochondrial membrane. This carries Ca^{2+} ions across the mitochondrial

membrane using the mitochondrial membrane potential difference ($\Delta\Psi_m$) as a driving force without the need for an ion exchange (Mitchell, 1961; Gunter and Pfeiffer, 1990). Mitochondrial respiration maintains $\Delta\Psi_m$ at around 150 – 200 mV negative to the cytosol through the generation of a H^+ electrochemical gradient (Duchen, 2000; Rizzuto et al., 2000). Studies using isolated mitochondria or mitochondria *in situ* within permeabilised cells have indicated that flux through the uniporter is only significant when $[Ca^{2+}]_c$ is in the micromolar range (Scarpa and Graziotti, 1973; Rizzuto *et al.*, 1993). In some cells, the mitochondria are located close to sites of Ca^{2+} release from the ER exposing them to micromolar concentrations of Ca^{2+} (Rizzuto *et al.*, 1993). However, in other cells mitochondria appear able to take up Ca^{2+} even when exposed to relatively small elevations of Ca^{2+}. For example, in rat luteal cells, measurable mitochondrial Ca^{2+} uptake has been shown to occur when $[Ca^{2+}]_c$ is increased from 50 nM to just 180 nM (Szabadkai *et al.*, 2001).

The stored Ca^{2+} in the mitochondria can be released via a Na^+ / Ca^{2+} exchanger (Crompton *et al.*, 1977; Fiskum and Lehninger, 1979; Carafoli, 1987). While the exact ion exchange involved is still not completely understood, suggestions include one Ca^{2+} ion being exchanged for two of sodium (Brand, 1985) or possibly three sodium for two Ca^{2+} (Brierley *et al.*, 1994). This helps maintain a low resting mitochondrial Ca^{2+} concentration $[Ca^{2+}]_m^{rest}$. In turn, the increased concentration Na^+ in the mitochondria is removed by a rapid Na^+ / H^+ exchanger.

Although under physiological conditions the Na^+ / Ca^{2+} exchanger appears to be the predominant efflux pathway (Rizzuto et al., 2000), other pathways exist to remove Ca^{2+}

from the mitochondria, including Na^+-independent Ca^{2+} efflux and the permeability transition pore (PTP). The PTP is a high conductance, non-selective channel providing fast Ca^{2+} release from the mitochondria. It is activated by a number of factors including the build up of Ca^{2+} within the mitochondrial matrix (Bernardi, 1999).

This pattern of uptake and release helps produce the different spatial and temporal dynamics of intracellular Ca^{2+} signalling needed to control the vast array of Ca^{2+}-dependent processes (Friel, 2000).

As well as the uniporter, work done on isolated liver mitochondria has proposed that the mitochondria can uptake Ca^{2+} via another route, the rapid uptake mode (RaM) (Sparagna *et al.*, 1995). This provides a very high rate of Ca^{2+} uptake into the mitochondria under physiological conditions before being quickly inhibited, possibly by rising $[Ca^{2+}]_m$.

1.8.2 Mitochondrial Calcium Buffering

Work done in the 1980s in hepatocytes concluded that mitochondria act to buffer increases in $[Ca^{2+}]_c$ mobilised from other intracellular sources (Shears and Kirk, 1984). This finding was backed up by results from permeabilised clonal pituitary cells, showing that a significant proportion of the Ca^{2+} released from the ER in response to IP_3 was transiently accumulated into mitochondria (Biden *et al.*, 1986).

A model of Ca^{2+} oscillations produced by Meyer and Stryer in 1988 included mitochondria as a crucial element in the buffering of cytosolic Ca^{2+}, keeping cytosolic

levels in the low micromolar range and helping return the system to resting levels (Meyer *et al.*, 1988; Meyer and Stryer, 1988); a result that has since been shown experimentally in a variety of cell types (Jouaville *et al.*, 1995; Zimmermann, 2000).

In neurones, the mitochondria are considered the major mechanism for cytosolic Ca^{2+} clearance following large increases in $[Ca^{2+}]_c$. At lower $[Ca^{2+}]_c$ changes, mitochondria still uptake Ca^{2+} from the cytoplasm, but at levels comparable to removal via plasma membrane pumps (Colegrove et al., 2000).

The prevailing view has been that Ca^{2+} accumulation into the neuronal mitochondria becomes increasingly influential as intracellular Ca^{2+} approaches ~500 nM (Friel and Tsien, 1994). Recently, experiments performed by Pivovarova *et al.* on sympathetic neurones have demonstrated that Ca^{2+} uptake occurs at intracellular Ca^{2+} levels as low as 300 nM. However, while inhibition of mitochondrial Ca^{2+} uptake with the protonophore FCCP has been shown to significantly increase $[Ca^{2+}]_c$ levels resulting from strong depolarisations, leading to $[Ca^{2+}]_c$ of ~500 – 800 nM (Friel and Tsien, 1994), it has little to no effect on $[Ca^{2+}]_c$ responses resulting from weak depolarisations which only increase $[Ca^{2+}]_c$ to ~300 nM. They further showed that simultaneously blocking uptake into the mitochondria and the ER with FCCP and thapsigargin respectively strongly potentiates $[Ca^{2+}]_c$ responses to weak depolarisations. They postulate that when Ca^{2+} uptake is inhibited in one organelle, $[Ca^{2+}]_c$ increases around the second organelle enhancing its uptake of Ca^{2+} and that the pronounced effect of FCCP on strong depolarisations indicates a higher-order dependence on $[Ca^{2+}]_c$ for mitochondria than for the ER (Pivovarova *et al.*, 1999). This higher dependence on $[Ca^{2+}]_c$ is shown in other cell types

by Szabadkai *et al.* who report that in rat luteal cells $[Ca^{2+}]_m$ increases as the square of $[Ca^{2+}]_c$ (Szabadkai *et al.*, 2001).

In sensory neurones, where large amounts of Ca^{2+} enter the cytoplasm across the plasma membrane following depolarisation-induced opening of ion channels mitochondria may be expected to be located primarily around the periphery of the cell. This, however, does not seem to be the case in rat secondary sensory neurones where electron microscopy experiments show a significantly lower density of mitochondria in the 1 μm adjacent to the plasma membrane than the average density of the cell (Shishkin *et al.*, 2002). Although no work has been done on chick sensory neurones, experiments on rat DRG neurones have shown that buffering of intracellular Ca^{2+} into the mitochondria makes a significant contribution to the kinetics of Ca^{2+} transients induced by long depolarisations (Thayer and Miller, 1990).

1.8.3 Targets of Mitochondrial Calcium

Work by Denton *et al.* in the 1970s suggests that the rate of ATP synthesis may be strongly dependent on Ca^{2+} uptake into the mitochondria (Denton *et al.*, 1972; Denton *et al.*, 1978). In sensory neurones, increases in mitochondrial Ca^{2+} allows ATP production to be matched to cellular activity demands. The increased $[Ca^{2+}]_m$ triggers an increase in the dehydrogenases of the tricarboxylic acid (TCA) cycle. This causes an increase in the conversion of NAD^+ to NADH; seen as an increase in the autofluorescence of NADH

(Duchen, 1992). In experiments on mouse sensory neurones, a 100 msec depolarisation of the plasma membrane has been shown to be sufficient to raise the NADH autofluorescence. This increase in autofluorescence is blocked by microinjection of the cell with Ruthenium Red (Duchen, 1992). The increased availability of NADH leads to increasing mitochondrial, and subsequently cytoplasmic, ATP levels. This has been directly observed by Jouaville *et al.* working on HeLa cells and skeletal myotubes using a mitochondrially targeted ATP probe (Jouaville et al., 1999). The mitochondria are the main source of cellular ATP, and as such must be responsive to the fluctuating energy demands of the cell (Jacobson and Duchen, 2004).

It has been suggested that Ca^{2+} uptake by mitochondria at low $[Ca^{2+}]_c$ could increase ATP production to provide for energy demands for processes triggered by $[Ca^{2+}]_c$ elevations, such as gene transcription (Fields et al., 1997).

1.9 Aims of This Thesis

The aim of my work has been to examine the speed of Ca^{2+} diffusion across nerve cell bodies in signalling to central structures such as the nucleus through a combination of experimental and modelling techniques. In doing this, I aim investigate whether processes such as Ca^{2+}-induced Ca^{2+} release play a significant role in the propagation of a depolarisation-induced Ca^{2+} signal across the cell.

The mathematical diffusion model, that I aim to develop, should allow me investigate the effects of the inclusion of a Ca^{2+} indicator dye on the intracellular Ca^{2+} dynamics and whether, in the absence of the indicator dye, a different pattern of Ca^{2+} diffusion occurs.

2 MATERIALS AND METHODS

2.1 Isolation of Dorsal Root Ganglion Neurones

Dorsal root ganglia (DRGs) are groups of sensory neurones involved in conveying information from the periphery to the CNS. Instead of the usual cellular make-up of an axon and a dendrite, these neurones have two axons; one extending towards the spinal column and the other towards the skin or muscle.

The ganglia contain cells of different sizes, loosely categorised into small, medium and large DRG neurones. These different neurones have been shown to have different physiological properties. Small diameter DRG neurones (< 28 mm) have previously been characterised by their sensitivity to capsaicin, which acts to open cation-selective ion channels in the plasma membrane. Large DRG neurones (> 35 μm), however, are found to be insensitive to capsaicin (Bevan and Szolcsanyi, 1990). Other observations have shown that Ca^{2+} transients are larger and decay more slowly in small than in large diameter rat DRG neurones (Gold, 2005).

While none of these results have been demonstrated in chick DRG neurones, I have continued to use the size-based classification of the neurones, and as such all of my work presented in this study was performed on small DRG neurones measuring 10-20 μm in diameter. These cells have previously been used in the Bolsover lab for patch clamp

experiments. Using the same cell type ensured previous results could be applied to my experiments.

DRGs were isolated from 12 day chick embryos killed by cervical dislocation. The spinal column was removed and cut into half, allowing the ganglia to be extracted.

The DRGs were incubated in 2.5 mg/ml collagenase in Dulbecco's Modified Eagle Medium (DMEM), 50 units/ml penicillin and 50 μg/ml streptomycin for 3 hours at 37°C and 5 % CO_2 before being centrifuged at 1000 rpm for 3 minutes. The supernatant was removed and the cells re-suspended in a growth medium consisting of 89 % DMEM, 10 % foetal calf serum, 50 units/ml penicillin, 50 μg/ml streptomycin and 20 ng/ml nerve growth factor.

The DRG neurones were then triturated through a fire polished Pasteur pipette and plated onto a multi-well plate (VWR International) pre-treated sequentially with poly-ornithine (5 mg/ml; 1hr) then laminin (0.5 mg/ml; 1hr).

The DRG neurones were left in the multi-well plate overnight before being replated onto glass cover slips (22 x 40 mm, number 1 glass, BDH, UK) pre-treated with poly-ornithine (5 mg/ml; 1hr). Replating the cells was done for two reasons: (i) it helps ensure the neurones have a simple shape, with no processes, making them easier to model mathematically; (ii) most of the glia and fibroblasts remain behind in the multi-well plate, producing cover slips primarily populated with neurones. The cover slips were then placed within a perfusion chamber (RC26, Warner Instruments, Hamden, CT, USA) secured on a recording platform (P1, Warner Instruments, Hamden, CT, USA) and incubated overnight.

2.2 Fluorescent Imaging

Fluorescence is a property of certain molecules that, when illuminated by a light source, give off light of a different wavelength. The molecules absorb photons from the illuminating light source temporarily raising their vibrational energy state. To return to their ground state from this unstable higher energy state, the molecules must lose vibrational energy. One of the ways this energy is lost is through the release of photons. The lifetime of the excited state is short, so that fluorescence emission ceases within nanoseconds of the end of excitation. Fluorescence is only one of the ways a molecule gives off energy in order to relax from an excited state and hence the emitted photon carries only a fraction of the energy provided by the excitatory one. The energy of a photon is given by $E = hc/\lambda$ (where h is Planck's constant, c is the speed of light in vacuum and λ is the wavelength of the radiation). As the wavelength is inversely proportional to the energy, this tells us the wavelength of the fluorescent light emitted by the molecule is always longer than that of the excitatory radiation. This is known as Stoke's law and gives rise to the Stoke shift in wavelength, figure 2.1.

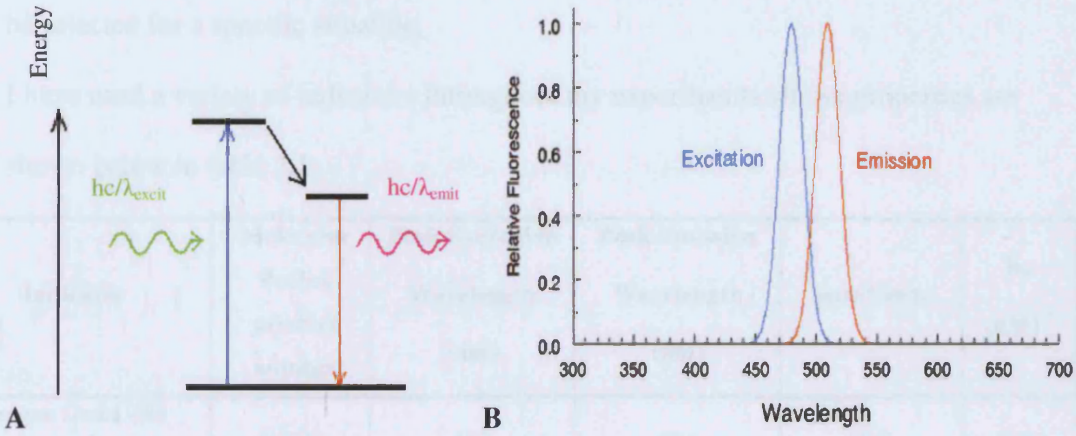

Figure 2.1 Principles of fluorescence emission

A: Energy level diagram showing the absorption of an excitatory photon, with an energy given by $E = hc/\lambda_{excit}$, raising a fluorescent molecule to a higher vibrational energy state. The fluorescent molecule emits its own photon in order to lose the energy required to return to its ground state. The energy of the emitted photon is given by $E = hc/\lambda_{emit}$. The lower energy of the emitted photon compared to the absorbed photon gives rise to the Stoke shift (B) resulting in the wavelength of the emitted fluorescence being longer than the excitation radiation.

2.2.1 Fluorescent Indicators

The fluorescent properties of certain molecules have been harnessed to produce a wide variety of fluorescent indicators. Many of these indicators fluoresce only when bound to a specific target, such as Ca^{2+}. There exist indicators to bind to a wide variety of different ions, molecules, proteins or organelles allowing them to selectively stain intracellular regions such as the mitochondria or endoplasmic reticulum. Calcium, in particular, can be detected by a wide range of fluorescent indicators varying in affinity, dynamic range, excitation / emission spectra and spatial specificity. These indicators come in a variety of forms, including free acid, acetoxymethyl (AM) ester and conjugated

to large molecular weight dextrans. Through careful choice, the appropriate indicator can be selected for a specific situation.

I have used a variety of indicators throughout my experiments whose properties are shown below in table 2.1.

Indicator	Molecular Probes product number	Peak Excitation Wavelength (nm)	Peak Emission Wavelength (nm)	Sensitive to	K_d (nM) [1]	Dye Form
Oregon Green 488 BAPTA-1 Dextran	O6798	497	524	Ca^{2+}	1833	Dextran conjugate
Rhod-2	R1245MP	552	581	Ca^{2+}	570	AM
Rhod-FF	R23983	552	580	Ca^{2+}	1670	AM
Fura Dextran	F3029	364 / 338	501 / 494	Ca^{2+}	240	Dextran conjugate
Hoechst 33342		352	455	Nucleic acid		Native
Calcein		494	514			AM
Tetramethylrhodamine Dextran	D1816	555	580			Dextran conjugate
Fluorescein Dextran	D3310	353	520			Dextran conjugate; caged
Mitotracker Green	M7514	490	516	Mitochondria		FM
Tetramethylrhodamine methyl ester (TMRM)	T668	549	573	Mitochondrial membrane potential		Native

Table 2.1 Fluorescent indicator properties

[1] The values here are the typical values given by the manufacturer. In some cases I have measured the values independently as described below.

2.2.2 Calculation of Calcium Concentration from Fluorescent Intensity

2.2.2.1 Single Wavelength Fluorescent Calcium Indicators

For single wavelength fluorescent indicators, that is ones that exhibit an increase in their fluorescence when Ca^{2+} bound, the fluorescence signals at time t, (I_t), can be converted into Ca^{2+} concentration ($[Ca^{2+}]_t$) knowing the dynamic range $(S)$of the dye, measured as the ratio of the fluorescent intensity at saturating Ca^{2+} against the fluorescent intensity at zero Ca^{2+}, the dissociation constant of the dye (K_d), the fluorescence at resting Ca^{2+} (I_0), and the resting Ca^{2+} concentration ($[Ca^{2+}]_r$), by modifying the basic calibration equation for the dye, shown below as equation 2.1.

$$[Ca^{2+}]_t = K_d * \frac{I_t - I_{\min}}{I_{\max} - I_t}$$

Equation 2.1

Where I_{max} and I_{min} are the fluorescent intensities measured at maximal and minimal free Ca^{2+} concentrations used in calibration.

In order to calculate Ca^{2+} concentrations from fluorescent imaging data, equation 2.1 can be rewritten, replacing I_{min} with FI_0 where I_0 is the fluorescence at resting Ca^{2+} concentrations and F is defined as in equation 2.2.

$$F = I_{min} / I_0 = \frac{K_d + [Ca^{2+}]_r}{[Ca^{2+}]_r S + K_d}$$

Equation 2.2

Replacing I_{max} by SI_{min} results in an equation for the Ca^{2+} concentration producing the fluorescent intensity I_t shown below as equation 2.3.

$$[Ca^{2+}]_t = K_d * \frac{I_t - FI_0}{SFI_0 - I_t}$$

Equation 2.3

2.2.2.2 Ratiometric Fluorescent Calcium Indicators

Ratiometric fluorescence Ca^{2+} indicators exhibit a shift in either their excitation or emission spectra when they bind to Ca^{2+}. In the example of fura dextran, binding to Ca^{2+} moves its excitation peak from 368 nm to 336 nm. By measuring a ratio of the Ca^{2+}-free fluorescence with the Ca^{2+}-bound fluorescence accurate measurements of the Ca^{2+} concentrations can be made. The main advantage of ratiometric dyes is that the measured

ratio is independent of the amount of dye present but directly dependent on the ion concentration. In addition, the ratioing of measurements eliminates variable effects such as photo-bleaching, detector sensitivity, cell thickness and optical paths. However, ratiometric indicators cannot be used for measuring dynamic calcium changes where changes in concentrations occur between measurements at the two wavelengths.

Fluorescence signals at the two wavelengths are used to calculate the fluorescence ratio at time t(R_t). This is then converted into Ca^{2+} concentration ($[Ca^{2+}]_t$) by applying:

$$[Ca^{2+}]_t = K_{1/2} * \frac{R_t - R_{min}}{R_{max} - R_t}$$

Equation 2.3

Where R_{min} and R_{max} are the ratios at zero and saturating Ca^{2+} concentrations respectively. $K_{1/2}$ is the Ca^{2+} concentration for which the ratio is the average of R_{min} and R_{max}.

2.2.2.3 In-vitro Calibration of OG488BD

To perform an in-vitro calibration of the Ca^{2+} indicator Oregon Green 488 BAPTA-1 Dextran (OG488BD), which I have used with equal concentrations of Tetramethylrhodamine dextran (TRITCD), a stock solution containing

10 mM of each indicator was dissolved in H_2O to a concentration of 500 μM. This stock was in-turn diluted ten-fold into solutions containing zero free Ca^{2+} and 1.35 μM free Ca^{2+} from a Calcium Calibration Buffer kit (Molecular Probes, C-3722) and into a solution containing saturating levels of free Ca^{2+} made up of 100 mM KCl, 30 mM HEPES and 1 mM $CaCl_2$ (all solutions at pH 7.2).

Using the Zeiss confocal with the same configuration settings used to image my experimental data, the intensity values for the indicator mixture were measured in all three free Ca^{2+} conditions under excitation at 488 nm. This was repeated many times, the dilution into the appropriate calibration buffer performed for each individual measurement, allowing an average intensity value for each calibration solution to be calculated. Once corrected for the background intensity signal, the intensity values were used to calculate the K_d and the dynamic range of the indicator dye.

From the saturated Ca^{2+} measurements and the measurements taken at zero free Ca^{2+} we can calculate the dynamic range as the ratio of the fluorescent intensity at saturating Ca^{2+} to the fluorescent intensity at zero Ca^{2+} levels (equation 2.4).

We can then use a rearranged form of the basic Ca^{2+} calculation equation for a single wavelength dye (equation 2.5) to calculate the estimated K_d using the saturating and zero free Ca^{2+} measurements along with those taken at 1.35 μM free Ca^{2+}.

$$dynamic \quad range = \frac{I_{max}}{I_0}$$

Equation 2.4

$$K_d = \frac{Ca^{2+} * (I_{max} - I)}{I - I_0}$$

Equation 2.5

For example, one batch had a measured K_d of 1.833 μM and a dynamic range of 4.55. The measured, in-vitro minimum fluorescence, I_0, could be very different to the in-vivo fluorescence altering the values of the K_d and the dynamic range inside the cell. However, I have assumed these difference are small and have used the values measured in-vitro throughout my experiments. This calibration was performed for every new dye stock.

2.2.2.4 In-vitro Calibration of Rhod-2

The Ca^{2+} indicator Rhod-2 was calibrated in the same way as OG488BD (section 2.2.2.3), but using an excitation wavelength of 543 nm, resulting in a measured K_d of 1.67 μM and a dynamic range of 9.1. The fluorescence signal measured in zero free Ca^{2+} was not significantly different from the background signal measured in the absence of Rhod-2. This indicates that Rhod-2 does not fluoresce when Ca^{2+} free. Only one stock of this dye was used.

2.3 Indicator Loading Techniques

2.3.1 AM-Loading

The charged structures of fluorescent indicators prevent them from crossing the lipid membrane surrounding cells. By coupling the indicator to Acetoxymethyl (AM) groups, by an ester bond, the molecular charge is neutralised, allowing the indicator to pass freely across the membrane. Once inside the cell, the AM bonds are cleaved by protein esterases releasing the free indicator molecule. This provides a non-intrusive method of loading fluorescent indicators into cells.

Cells loaded in this manner were incubated in standard growth medium containing the required concentration of AM indicator for 30 minutes at room temperature in an atmosphere containing 5 % CO_2. As well as loading the cytosol and the nucleus, the free acid can be pumped into the endoplasmic reticulum (ER), by a broad spectrum anion transporter, where it would be insensitive to cytosolic changes; it is mainly to reduce this effect that we load at room temperature.

2.3.2 Patch Clamping

Patch clamping is a technique developed by Neher and Sakmann (Neher and Sakmann, 1976) and improved upon by Sigworth and Neher in the early 1980s (Hamill et al., 1981).

This technique uses a narrow tipped glass pipette sealed against the membrane of a cell to directly measure the current passing through a single ion channel.

Depending on the size of the patch, one or more channels may be isolated under the pipette. Current flowing through the channel can be detected by a sensitive current-to-voltage converter that is connected to the inside of the electrode.

2.3.2.1 Whole-Cell Patch Clamping

The whole-cell patch clamp configuration allows direct access to the inside of the cell providing control of the cell's membrane potential allowing the membrane to be depolarised as required causing Ca^{2+} transients via the opening of voltage-gated Ca^{2+} channels.

A glass pipette, with a narrow tip (3 -5 μm), is placed against the membrane of a cell. The application of suction to the inside of the pipette can lead to an electrical seal between the glass and the membrane so tight that ions are effectively prevented from leaking out. By applying abrupt suction to the pipette, the section of cell membrane under the pipette is broken.

In the whole-cell configuration, solutions in the patch pipette equilibrate with the cell cytosol following concentration gradients. This was used as a method of introducing fluorescent dyes and specific drugs into the interior of the DRG neurones.

Cells were washed with external solution (containing, in mM, NaCl 120, $MgCl_2$ 1.2, KCl 5.5, $CaCl_2$ 1.8, CsCl 10, TEA-Cl 1.8, HEPES 10, glucose 25, tetrodotoxin (TTX) 0.001,

BayK 8644 (±) 0.005; osmolarity adjusted to 320 mOsm with sucrose; pH 7.2) and placed on the stage of a Zeiss confocal microscope. When used externally at these concentrations, Tetrodotoxin (TTX), extracted from the Japanese puffer fish *fugu*, binds to sodium channels, blocking the flow of sodium. TEA was used to block potassium channels. This helps ensures that any current we see is limited to the Ca^{2+} channels. BayK 8644, an agonist of L-type Ca^{2+} channels, can enhance the currents passing through these channels by increasing their open probabilities (Diochot *et al.*, 1995; Desmadryl *et al.*, 1997; Satoh *et al.*, 1997; Dolphin, 2001; Heinemann, 2001).

Micropipettes were produced from glass capillary tubes with a microfilament insertion (Clark Electrical, GC100F-10) using a two-stage Narishige pipette puller (Micro Instruments, Oxon, UK) producing electrodes with access resistances between 10 - 20 MΩ. The tip of the micropipette was filled with 100 μM of the required fluorescent dye made up in a standard internal solution (in mM: CsCl 125, HEPES 10, MgATP 4; osmolarity 300 mOsm; pH 7.2). The pipettes were then back-filled with internal solution.

These pipettes were then mounted on an Axon HS-2 headstage (Axon instruments, Foster City, USA). Two Ag/AgCl recording electrodes, one inside the pipette and the other in the bath, provide an electrical circuit required to measure the seal resistance of the patch. The voltage through these electrodes was controlled using an Axoclamp 2A amplifier with a low-pass filter operating at 10 kHz and a digitizer rate of 2 kHz for 50 msec depolarisations and 200 Hz for 1 second depolarisations (Axon Instruments, Foster City, USA) running in continuous voltage clamp mode and Clampex 7 software (Axon

Instruments, Foster City, USA) running on a Dell computer with a Intel 486/50 processor and 8 Mb RAM.

The headstage was mounted on a specially constructed, vibration-free frame attached to the side of the microscope.

A problem introduced by the use of the confocal microscope was that switching between standard microscopy (in which the cell and the micropipette can be viewed through the eyepieces) and confocal mode generated considerable vibration which may displace the micropipette. For this reason, the micropipette was positioned some distance ($\approx$ 100 μm) above the cell using standard microscopy. The system was then switched to confocal mode and the final approach of the pipette to cell performed 'blind' using an x/y/z piezo-electric micromanipulator (Burleigh Instruments, NY, USA). The increase in access resistance of the pipette was used as an indicator that the pipette had reached the cell membrane and light suction was then applied until a giga-Ohm seal was achieved. The holding voltage was reduced to -70 mV and the cell was left for 30 seconds before sharp suction was applied to break the patch of membrane under the pipette and achieve the whole-cell configuration.

2.4 Fluorescent Microscopy

Fluorescent microscopy couples the use of fluorescent indicators with conventional microscopy techniques. This allows us to identify cellular regions and follow molecular pathways occurring within a cell *in situ*. Fluorescent indicators can be introduced into a

cell either via a patch pipette or through AM-loading. The sample is then illuminated, by lasers or a mercury light source, exciting the fluorescent molecules. The resulting fluorescent emission passes to detectors where it is converted to electrical signals and the resulting image displayed and stored on an accompanying computer.

For non-confocal, fluorescent microscopy experiments I used a Zeiss Axiovert 100 TV and a TILL Photonics imaging system, mounted on an air table and earthed to a Faraday cage. The same patch clamp set-up was used as described in section 2.3.1. A simple perfusion system enabled the extracellular medium to be changed during imaging experiments.

2.4.1 Confocal Laser Scanning Microscopy

A confocal microscope differs from a conventional one in its ability to image a single focal plane without light interference from other focal planes. This is achieved through the use of a pinhole positioned at the focal point of the objective lens. This ensures that only emitted light from the in-focus region of the sample reaches the detector. Light from above and below the plane of focus of the object is eliminated, preventing the background haze from the out-of-focus planes complicating the image resulting in improved contrast and higher resolution (figure 2.2a).

The optimum diameter of the pinhole depends on the wavelength of the excitation light. As the emitted light passes through the pinhole it is diffracted producing a pattern known as an Airy disk (figure 2.2b). The diameter of this disk increases proportionally with wavelength and so the pinhole must be adjusted to produce the maximum emission intensity whilst removing other diffracted light.

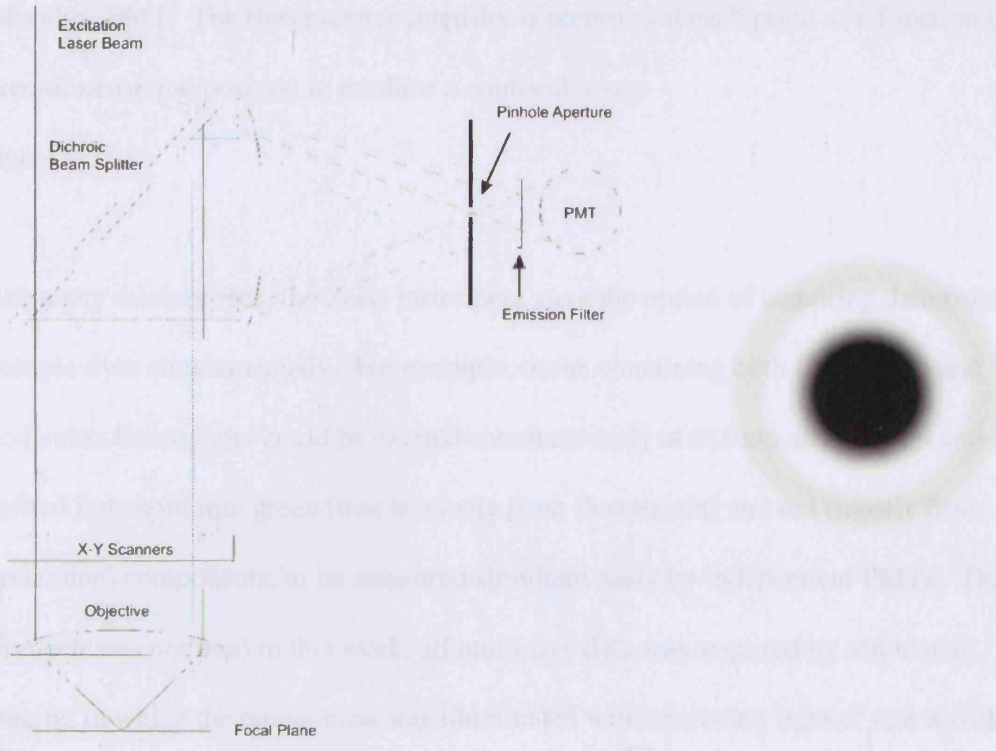

Figure 2.2 Producing confocal images

(a): Schematic of the confocal system, showing the use of a pinhole to remove out of focus emission.

(b): Airy disk produced by diffraction of light through the pinhole.

On a laser scanning confocal microscope, the excitation light is provided by lasers. These can provide intense beams of light at the specific wavelength required to excite the fluorescent molecules. The precise wavelengths are selected using acousto-optical tuning

filters (AOTFs). In order to generate an image, collimators focus the laser beam onto the mirrors used to move the focused laser across the sample. The emitted light from each point passes through the pinhole and is detected by photo-multiplier tubes (PMTs) and analog-to-digital converters turning the light intensity into an electrical signal. 12-bit coding was used throughout. Dichroic mirrors are used to separate the emitted signals from different fluorescent molecules, directing each selected wavelength band to an individual PMT. The fluorescence intensity is recorded at each point as a function of its three-dimensional position to produce a confocal image
(figure 2.3).

Like many microscopes, the Zeiss instrument gave the option of acquiring data from multiple dyes simultaneously. For example, tissue containing both fluorescein and rhodamine fluorophors could be excited simultaneously at 488 nm and 543 nm and the emitted light split into green (that is mostly from fluorescein) and red (mostly from rhodamine) components, to be measured simultaneously by independent PMTs. This approach was not used in this work; all multi-dye data was acquired by sequential imaging in which the preparation was illuminated with excitation light of one wavelength and the resulting emission signal measured, then illuminated with excitation light of a second wavelength and the second emission signal measured, and so on. This approach takes more time than simultaneous imaging, but gives much greater selectivity, helping to reduce the contamination of one channel (such as rhodamine) by light from another (such as fluorescein).

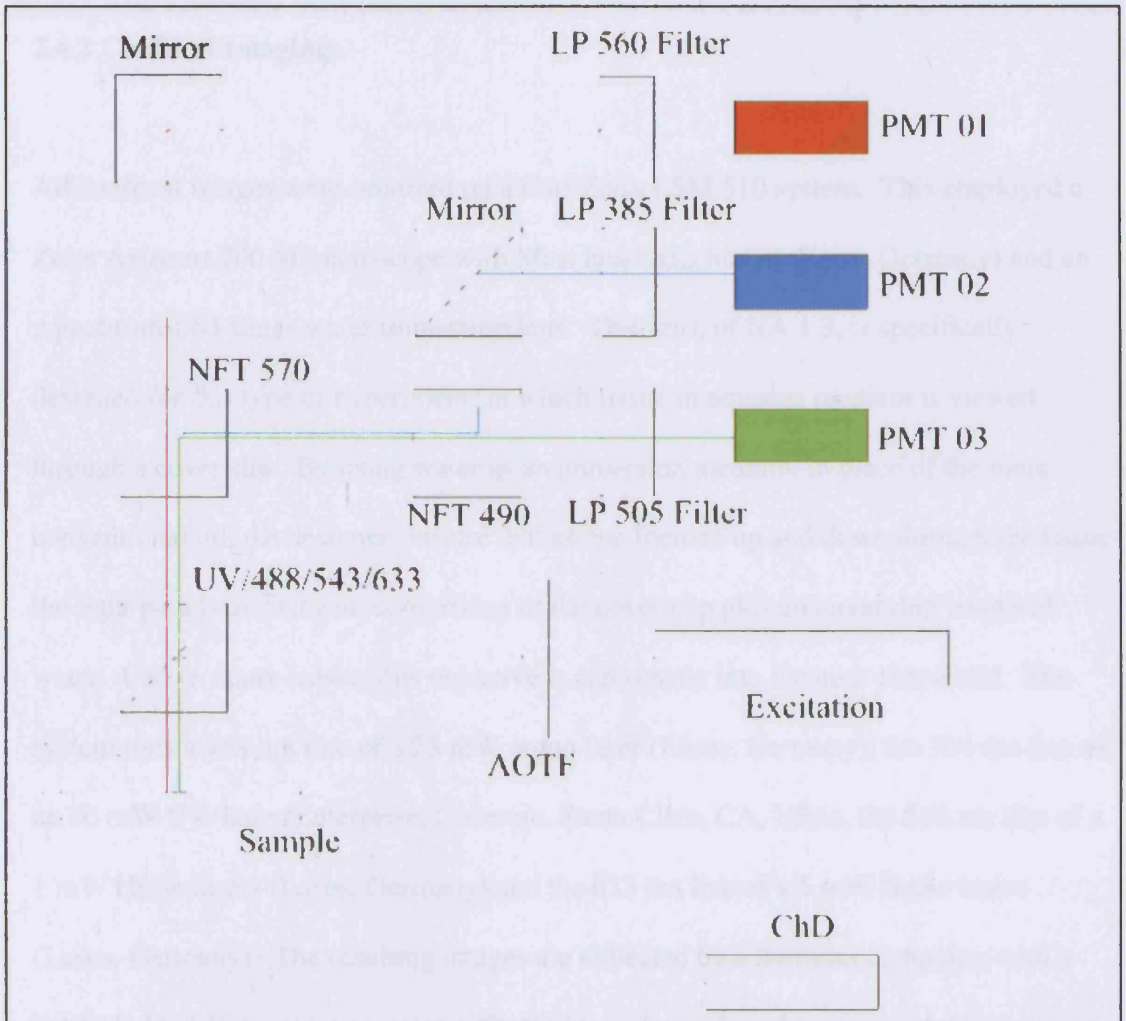

Figure 2.3 Schematic of confocal set-up

Zeiss confocal microscope set-up used for standard patch clamp experiments with pipette containing 100 μM OG488BD and 100 μM tetramethylrhodamine dextran and the cell nucleus stained with 2 μM Hoechst. Excitation is provided by sequential illumination at 488 nm, 543 nm and 364 nm respectively for the three dyes. The emission from the OG488BD is reflected by the NFT570 dichroic, but passes through the NFT490 dichoric to PMT 03. A long-pass 505 filter helps remove any contaminating light from the signal. The emission from Hoechst follows the same path as the OG488BD, but is reflected by the NFT490 dichroic to PMT 02, while the tetramethylrhodamine emission passes through the NFT 570 dichroic to PMT 01.

2.4.2 Confocal Imaging

All confocal images were acquired on a Carl Zeiss LSM 510 system. This employed a Zeiss Axiovert 200 M microscope with Meta head attachment (Zeiss, Germany) and an Apochromat 63-times water immersion lens. This lens, of NA 1.3, is specifically designed for this type of experiment; in which tissue in aqueous medium is viewed through a cover slip. By using water as an immersion medium, in place of the more conventional oil, the designers ensure that as one focuses up and down through the tissue the light path is unchanged, comprising of the cover slip plus an unvarying length of water. Unlike many lenses, this objective is achromatic into the near ultraviolet. The system uses a 488 nm line of a 25 mW argon laser (Lasos, Germany), the 364 nm line of an 80 mW UV-laser (Enterprise, Coherent, Santa Clara, CA, USA), the 543 nm line of a 1 mW HeNe lasers (Lasos, Germany) and the 633 nm line of a 5 mW HeNe lasers (Lasos, Germany). The resulting images are collected by a Siemens computer, with a 2.4 GHz Intel Xeon processor and 1 Gb RAM, and transferred onto recordable compact discs for off-line analysis and long-term storage.

2.4.2.1 Linescan Imaging

The linescan setting was used to image the Ca^{2+} changes resulting from a short, 50 msec depolarisation. This setting was chosen as it provides the fast resolution required to image events happening on millisecond time scales. These 50 msec depolarisations correspond to tens of action potentials. This is closer to physiological conditions than many previous studies on neuronal calcium signalling and of relevance to events such as synaptic transmission where trains of action potentials are observed.

From an x/y image, a line was chosen, intersecting the nucleus, along which the laser would scan at a speed of 1.92 msec per line (scan speed setting 9). The PMTs were adjusted to ensure the signal was not saturating and then the system was set to image this line continuously 6000 times, providing just under 12 seconds of imaging time (figure 2.4a). Starting the imaging triggers the start of a protocol in Clampex 7 to depolarise the cell membrane from the holding voltage of -70 mV to +10 mV for 50 msec. after 550 linescans (1.056 s). This increases the open probability of the voltage-sensitive Ca^{2+} channels in the plasma membrane allowing Ca^{2+} from the extracellular medium to enter the cytosol where it is seen as an increase in OG488BD fluorescence. The resulting image is displayed with distance across the cell in the x-direction and time in the y-direction. From this, one can clearly see the radial diffusion as the Ca^{2+} entering the cell through the plasma membrane Ca^{2+} channels propagates to the centre of the cell. The action of the plasma membrane Ca^{2+} pumps is also evident; returning the Ca^{2+} concentration to resting levels over a period of around 6 seconds (figure 2.4b). The whole-cell currents were measured using Clampex 7 and stored on a

Dell computer with an Intel 486/50 processor and 8 Mb RAM. These were then exported from pClamp6 software and leak-subtracted in Excel.

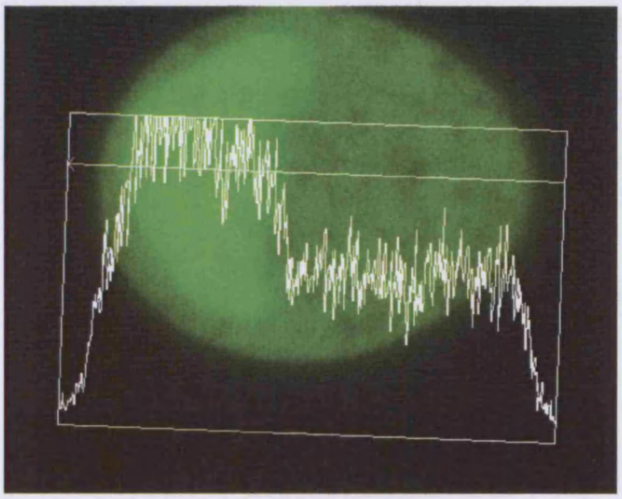

Figure 2.4a Confocal image of a DRG neurone
Scan line drawn through the cell intersecting the nucleus showing the intensity is greatest in nuclear region on the left. While the signal is clearly saturating in the nucleus, this was adjusted before the linescan experiments were performed.

Figure 2.4b
Raw linescan data resulting from imaging along the scan line 6000 times at a speed of one scan every 1.92 msec. The cell is depolarised for 50 msec. from a holding voltage of -70 mV to +10 mV causing the voltage sensitive Ca^{2+} channels on the plasma membrane to open and cytosolic Ca^{2+} to rise. This is seen as an increase in fluorescent intensity.

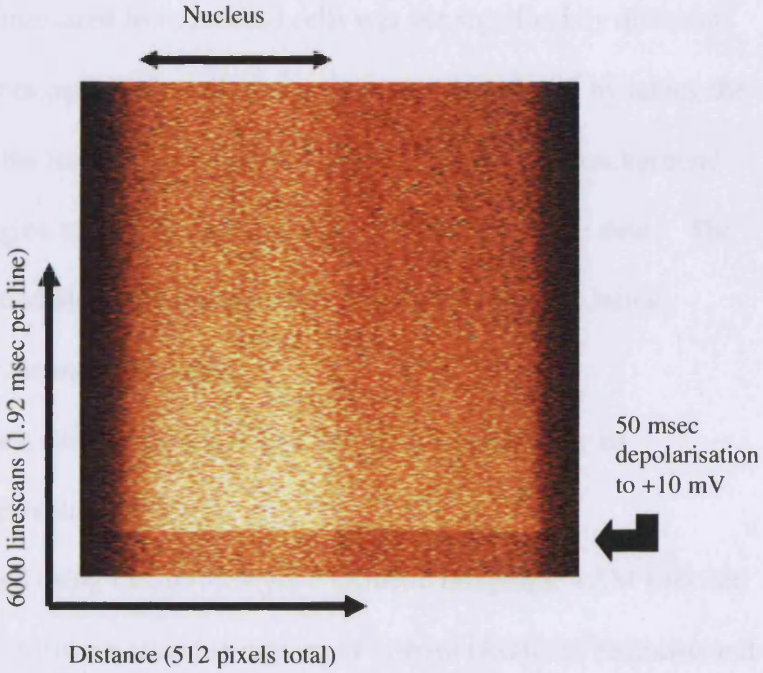

2.4.2.2 Confocal Z-Stacks

The z-stack setting of the confocal microscope allows a series of x/y images of the sample to be taken at predetermined steps through the z-direction. Through the Zeiss software, the step size and start and finish points are selected; the computer automatically incrementing the z-position by one step after each x/y scan.

The completed z-stack enables a three-dimensional image of the sample to be created.

2.5 Image Analysis

Linescan images were imported into Matlab (release 12, The Math Works) for analysis. It was found that the signal measured from unfilled cells was not significantly different from the signal measured from outside the cells and so any error introduced by taking the signal outside the cell to be the true background was ignored. The average background value is measured from a region outside of each cell and subtracted from the data. The first 40 values for each position along the linescan were averaged to give an initial, pre-depolarisation value for the intensity signal.

The data is then displayed as a normalised I/I_0 image; dividing each pixel by its pre-depolarisation value (figure 2.5).

The x/y images were analysed using Lucida Analyse 5 (Kinetic Imaging). LSM files can be imported directly into the software allowing regions of interest (ROIs) to be drawn and

average intensity signals to be calculated and plotted against time. These can be imported into Excel for further analysis.

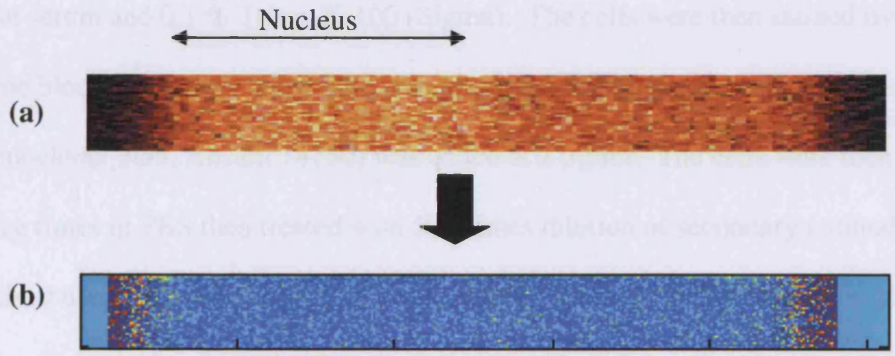

Figure 2.5 Analysing linescan data

From the raw linescan data (a), it appears as if the fluorescence from the nucleus is brighter than that from the cytosol. To rectify this, all linescan data is imported into Matlab, background corrected and normalised against pre-depolarisation fluorescence values (b). This removes any difference between the resting fluorescent intensity in the two regions allowing depolarisation-induced changes to be observed more clearly.

2.6 Immunofluorescence Imaging

Where the mitotracker family of fluorescent indicators have been included to identify the mitochondria, immunofluorescence experiments were used to confirm that mitotracker positive organelles were indeed mitochondria.

DRG neurones preloaded in 200 nM mitotracker green were confocally imaged whilst alive and then fixed for ten minutes in 4 % paraformaldehyde in phosphate buffered saline (PBS, Sigma). Cells were washed three times in PBS plus 0.05 % Tween (Sigma) then blocked for 30 minutes in PBS supplemented with 1 % bovine serum albubin, 10 % goat serum and 0.1 % Triton X-100 (Sigma). The cells were then stained overnight in the same block solution to which anti-mitochondrial ATP synthase subunit beta (mouse monoclonal 3D5, Abcam 14730) was added at 2 μg/ml. The cells were then washed three times in PBS then treated with 500-times dilution of secondary antibody (goat anti-mouse, Alexa 633 conjugate, Molecular Probes) in block solution for two hours. After three washes in PBS, the cells were imaged on the confocal microscope using 633 nm excitation and 650 nm longpass collection.

3 PATCH CLAMPING AND IMAGING RESULTS

3.1 Measurement of Resting Intracellular Calcium Concentration by Fura Dextran

To measure the resting Ca^{2+} concentration in DRG neurons ($[Ca^{2+}]_{rest}$) cells were whole-cell patch clamped with 100 μM Fura 10 kDa dextran in the patch pipette on the stage of a Zeiss Axiovert 100 TV non-confocal microscope (Zeiss, Germany) attached to a TILL Photonics imaging system.

The cell was patched as described in section 2.3.2.1 with a caesium-based patch solution in the patch pipette. Once cell-attached, a light puff of air was used to blow away any fura dextran which had leaked from the pipette into the external solution. The patch was then taken whole-cell and the system left for 3 minutes to allow the dye to fill the cell. The cells were imaged for 1 second at 340 nm and 380 nm allowing ratiometric calculations to measure the Ca^{2+} concentration as described in section 2.2.2.2.

Taking a ratio of the fluorescent emission of fura dextran when excited at 380 nm and 340 nm allows us to calculate the proportion of Ca^{2+} bound to the indicator. When using this in combination with the measured $K_{1/2}$ we can calculate the Ca^{2+} concentration using equation 3.1 (Tsien et al., 1982).

$$[Ca^{2+}] = K_{1/2} \frac{(R - R_{min})}{(R_{max} - R)}$$

Equation 3.1

where R is the background corrected 340/380 fluorescence ratio, R_{min} is the ratio at zero $[Ca^{2+}]$ and R_{max} is the ratio for a saturating $[Ca^{2+}]$. In order to measure the background signal, images of the cell and pipette at each excitation wavelength were acquired whilst in the cell-attached configuration. These were used to calculate a background signal that included cell autofluorescence and stray light from dye in the pipette. This value was removed from the measured fluorescence intensities before they were used in equation 3.1.

The $K_{1/2}$ for fura dextran was calibrated using a similar technique as in section 2.2.2.3. The fluorescent ratios were measured at zero Ca^{2+} level, saturating Ca^{2+} and at 1.35 μM free Ca^{2+}; the $K_{1/2}$ is calculated, by rearranging equation 3.1, to be 4.28 μM.

To confirm the cell was healthy, it was depolarised for 50 msec after the fura dextran measurements were taken and only cells with inward currents of amplitude > 100 pA accepted.

My measurements result in a value for the cytosolic, resting, Ca^{2+} concentration in chick DRG neurones of $[Ca^{2+}]_{rest}$ = 129 ± 38 nM (mean ± SEM; n = 6). This is consistent with previously quoted values of between $[Ca^{2+}]_{rest}$ = 97 ± 7 nM and $[Ca^{2+}]_{rest}$ = 160 ± 8.9 nM (n = 36) in chick sensory neurones (Snow *et al.*, 1994; Bolsover *et al.*, 1996) as well as values measured using AM loaded fura-2 in whole, unpatched rat DRG neurones of 73 ± 2.2 nM (mean ± SEM; n = 94) (Usachev *et al.*, 1993a).

3.2 Basic Result – Radial Calcium Diffusion wave

Depolarisation of the plasma membrane of a chick DRG neurone increases the open probability of L- and N-type Ca^{2+} channels in the membrane causing a flux of Ca^{2+} from the extracellular to the intracellular space (Diochot *et al.*, 1995; Catterall, 2000).

The inward Ca^{2+} current produced by a 50 msec depolarisation of the plasma membrane from the holding voltage of -70 mV to +10 mV was found to raise the $[Ca^{2+}]_c$ by 0.96 ± 0.17 μM (mean ± SEM; n = 32), consistent with previously measured values (Bootman *et al.*, 2001a). Linescan data from these cells show a clear radial Ca^{2+} influx, originating at the plasma membrane and diffusing into the centre of the cell with a time to half maximum intensity of 24 ± 2 msec (n = 20) (figure 3.1).

The increased cytosolic Ca^{2+} levels are reduced by plasma membrane Ca^{2+}-ATPase (PMCA) pumps, Na^+/Ca^{2+} exchangers and uptake into intracellular Ca^{2+} stores, returning the Ca^{2+} to resting levels over a few seconds.

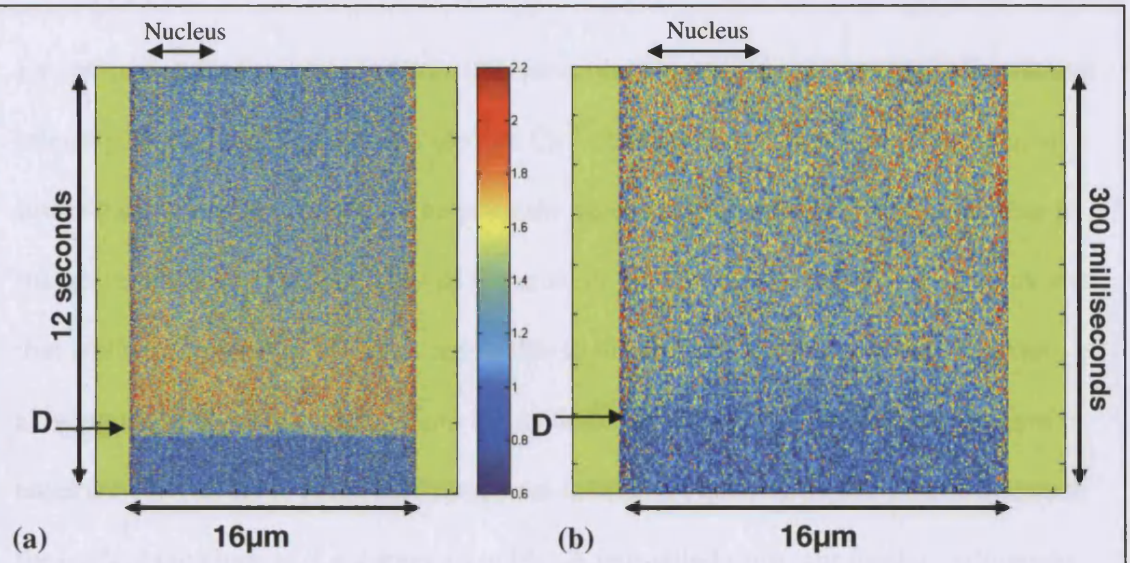

Figure 3.1 Linescan image

Linescan image of a chick DRG neurone showing a Ca^{2+} influx through plasma membrane Ca^{2+} channels opened by a 50 msec depolarisation of the membrane. The raw intensity data is imported into Matlab where it is converted into a normalised array of I/I(0) values shown here. (a) shows a whole linescan experiment performed over 12 seconds. The neurone is depolarised for 50 msec after 1.070 seconds (at point D) causing a radial Ca^{2+} influx originating at the plasma membrane and diffusing into the centre of the cell. Image (b) focuses on the 300 msec around the depolarisation, more clearly showing the radial Ca^{2+} influx originating at the plasma membrane and diffusing into the centre of the cell in around 30 msecs. The colour bars show increasing I/I(0) values.

In order to make a quantitative analysis of the Ca^{2+} dynamics, the fluorescent signal was measured at three specific points in each cell; at the centre of the cell and 3 µm in from the plasma membrane on each side. Due to the standard topography of the replated chick DRG neurones, as discussed later in section 5.3, one of the measurements taken 3 µm from the edge of the cell always falls in the nucleus, while both the others lie in the cytoplasm. This allowed me to observe the effect of the nuclear envelope on the diffusion dynamics.

By comparing the increases in Ca^{2+} concentration, represented as increases in fluorescent intensity, at the two sides, we can see that Ca^{2+} changes occur more slowly at the point inside the nucleus as opposed to the point the same distance into the cytosol resulting in the centre of the influx being skewed towards the nuclear side of the cell. This indicates that while the nuclear envelope is permeable to intracellular Ca^{2+}, it presents a barrier slowing the diffusion of the ions into the nucleus (figure 3.2). By comparing the time it takes the Ca^{2+} levels to reach half-maximum intensity, I have measured this delay due to the nuclear envelope as 9 ± 2 msec ($n = 38$). A two-tailed t-test was used to help assess whether this is a statistically significant delay. Compared against a hypothetical mean of zero, representing free diffusion, the delay in diffusion across the nuclear envelope is found to be extremely statistically significant ($P < 0.0001$).

I performed a similar analysis on the two points in the cytoplasm; the one 3 μm in from the plasma membrane and the other in the centre of the cell. By again comparing the time taken for the increase in fluorescent intensity to reach half-maximum, the delay caused by Ca^{2+} diffusing to the centre of the cell was measured at 24 ± 2 msec ($n = 19$).

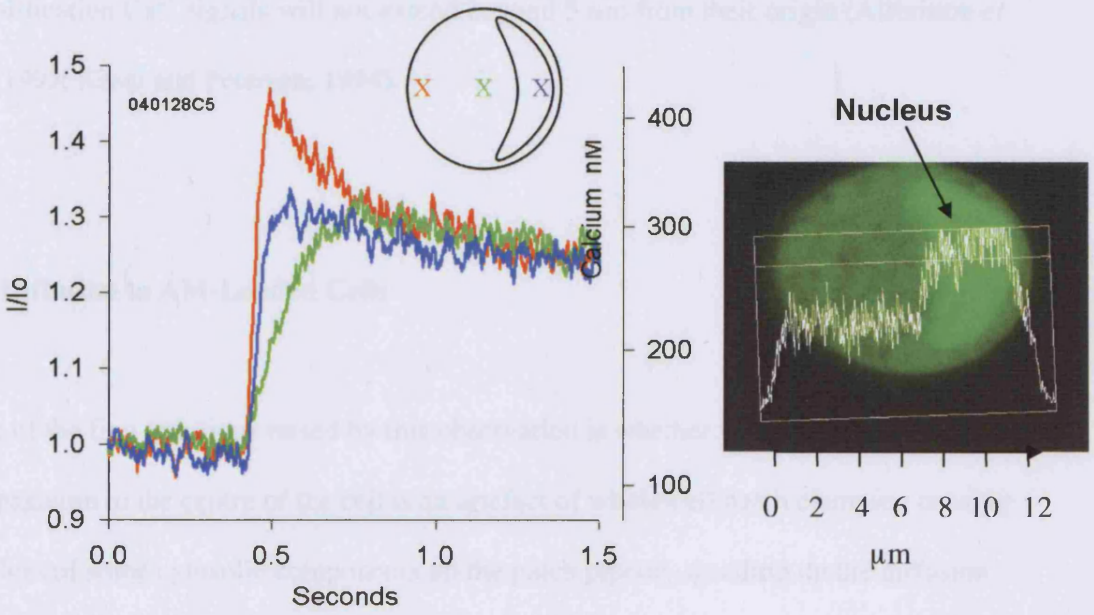

Figure 3.2 Quantitative analysis of linescan data

In order to quantitatively measure the Ca^{2+} dynamics following depolarisations, three standard points were selected at which to measure the changes in fluorescent intensity of OG488BD resulting from changes in Ca^{2+} concentration. The points, shown in the graph insert, were located 3 µm in from the plasma membrane on each side of the cell and one point in the centre of the cell. Due to the topography of an E12 chick DRG neurone, one of the points 3 µm in from the edge always lies in the nucleus while the others fall in the cytoplasm. These allow two standard measurements to be made of Ca^{2+} dynamics; the time taken for the Ca^{2+} signal to diffuse to the centre of the cell and the delay caused to the signal in crossing the nuclear membrane. Comparisons of these values in different conditions allow me to quantitatively describe any changes in the Ca^{2+} dynamics obtained through experiments.

Using the same data, the time taken for the Ca^{2+} signal to equilibrate in concentration across the whole neurone was measured as 557 ± 88 msec (n = 18).

These results shows that diffusion of the Ca^{2+} signal inside chick DRG neurones following a 50 msec depolarisation of the plasma membrane is a fast event, occurring at the centre of the cells on timescales of milliseconds, clearly contradicting many earlier

views that Ca^{2+} diffusion is extremely limited in the cytosol, such that without amplification Ca^{2+} signals will not extend beyond 5 μm from their origin (Allbritton *et al.*, 1992; Kasai and Petersen, 1994).

3.3 Diffusion in AM-Loaded Cells

One of the first questions raised by this observation is whether this fast signal propagation to the centre of the cell is an artefact of whole-cell patch clamping causing the loss of some cytosolic components up the patch pipette, speeding up the diffusion through the cytoplasm.

To eliminate the effect of whole-cell washout, Ca^{2+} signalling in intact, AM-loaded cells could have been tested using depolarisations induced by extracellular potassium puffs. However, in order to compare the intracellular Ca^{2+} dynamics in unperturbed cells with those maintained in the whole-cell patch configuration, I AM-loaded DRG neurones with Oregon Green BAPTA-1 AM (molecular probes, O6807). These cells were then patched in the normal way, as described in section 2.3.2.1, with the dextran conjugated form of the dye in the patch pipette. The cells were depolarised immediately upon going whole-cell and then again after three minutes in the whole-cell configuration, by which time the dextran-conjugated form of the Ca^{2+} indicator had diffused into the cell.

Comparison of the two diffusion patterns shows no significant difference in the Ca^{2+} dynamics (figure 3.3).

To further quantify this, I used the standard analysis of the fluorescent intensity signal at the three points within the cell to compare the time taken for the Ca^{2+} signal to diffuse through the cytosol and across the nuclear membrane for the first and second depolarisations. Calculating the difference between these values in each individual cell shows that although the diffusion is slightly slower in both cases for AM-loaded cells depolarised immediately, compared against the same cells depolarised after 3 minutes in the whole-cell patch clamp configuration, this was not a significant difference (4 ± 4 msec; $P = 0.3661$ and 1 ± 7 msec; $P = 0.844$ respectively for diffusion through the cytoplasm to the centre of the cell and diffusion through the nuclear envelope compared against hypothetical values of zero representing no difference in diffusion times for AM-loaded cells and cells left in the whole-cell configuration for three minutes; $n = 10$).

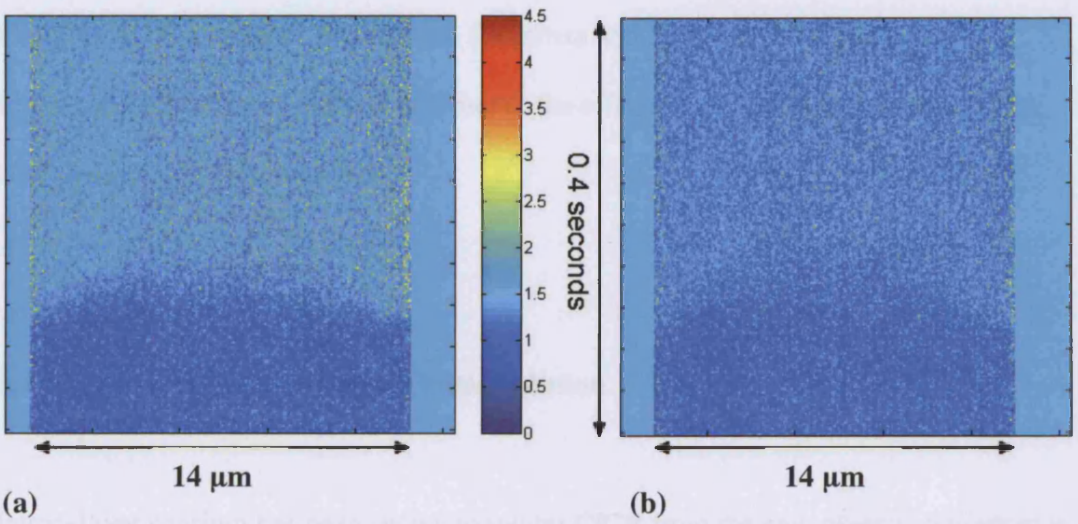

Figure 3.3 Effects of loss of cytosolic constituents on calcium diffusion

Linescan images from the same cell (240604_C6) AM-loaded with OG488 BAPTA-1 AM and whole-cell patch clamped with a pipette containing OG488BD. The cell was depolarised immediately upon going whole-cell (a) and again after three minutes whole-cell (b), allowing a comparison of the Ca^{2+} dynamics. The resulting images show that any loss of cytosolic constituents up the patch pipette does not have a significant effect on the diffusion of Ca^{2+} to the centre of the neurone. This was confirmed through statistical analysis of the temporal and spatial diffusion dynamics.

3.4 Calcium-Induced Calcium Release

Another possible reason for the observed fast diffusion of the Ca^{2+} signal would be calcium-induced calcium release (CICR). CICR describes the process of Ca^{2+} release from intracellular stores, such as the sarco / endoplasmic reticulum, triggered by a rise in intracellular Ca^{2+} concentration. This has been shown to be a major contributor to increases in free Ca^{2+} in most cell types, resulting in the release of large concentrations of free Ca^{2+} into the cytosol in response to Ca^{2+} activation of the ryanodine receptor

(Rizzuto, 2001). This provides an amplification of the Ca^{2+} signal, prolonging the signal lifetime and increasing its propagation (Bootman and Berridge, 1995).

I have used a number of methods to observe the effects of CICR on Ca^{2+} signalling in DRG neurones as laid out below.

3.4.1 Use of a Potassium-Based Pipette Solution

Intracellular caesium has been shown to inhibit CICR from the endoplasmic reticulum in a similar way to ryanodine (Kennedy and Meech, 2002). In order to see if this had any effect on the Ca^{2+} dynamics following a 50 msec depolarisation, I repeated the standard patch clamp experiments using a potassium-based pipette solution (125 mM KCl, 10 mM HEPES, 4 mM MgATP, 100 μM OG488BD; 300 mOsM; pH 7.2). Experiments performed using the potassium intracellular solution were analysed in an identical way to the caesium-based results. From these I measured a delay at the nuclear envelope of 10 ± 2 msec ($n = 27$) and a delay in Ca^{2+} diffusion through the cytosol to the centre of the cell of 27 ± 4 msec ($n = 27$). Neither of these values were found to be statistically different from the values obtained with a caesium-based intracellular solution ($P = 0.7595$ and $P = 0.5468$ respectively).

3.4.2 Long Depolarisations and Trains of Depolarisations

Significant CICR has been shown to be produced in rat DRG neurones following large increases of intracellular Ca^{2+} (Shmigol *et al.*, 1995b). In this work I have used two methods to raise the cytosolic Ca^{2+} concentration to levels expected to trigger CICR. The first of these was the use of long depolarisations; depolarising the plasma membrane from the holding voltage of -70 mV to +10 mV for 1 second, instead of the standard 50 msec. The second involved the use of ten 50 msec depolarisations in quick succession. These methods raised $[Ca^{2+}]_c$ to 2.7 ± 0.7 μM (n = 10) and 3.3 ± 1.4 μM (n = 10) respectively, concentrations that have been shown to activate the ryanodine receptors on the ER in many cell types (Bootman *et al.*, 2001a).

Even at these concentrations, all diffusion appeared radial; originating at the plasma membrane and diffusing into the centre of the cell. Had CICR been present, it would appear as local increases in fluorescence intensity diffusing out from a point inside the cell. These results failed to reveal any CICR (figure 3.4).

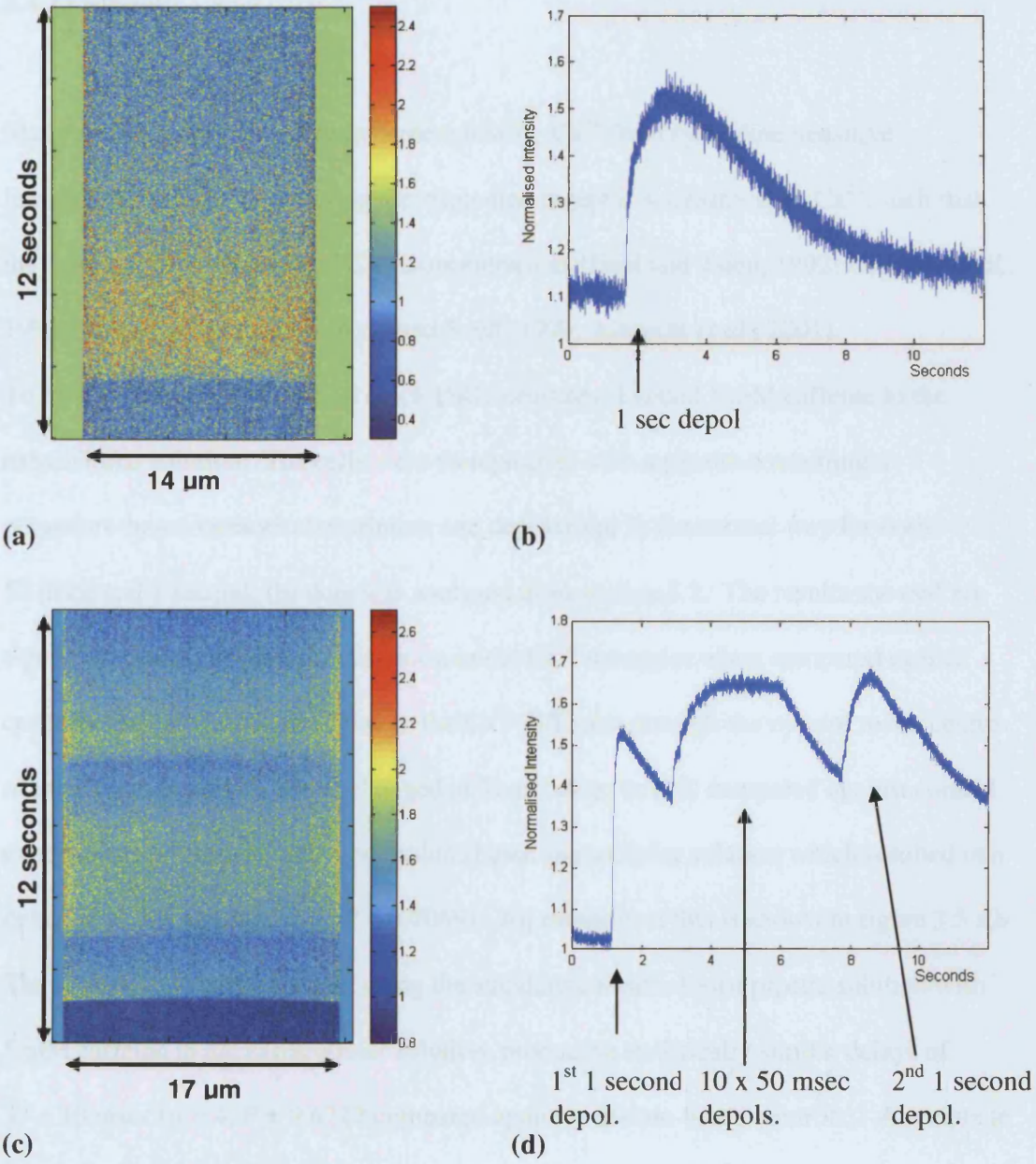

Figure 3.4 Large increases in $[Ca^{2+}]_c$

Large increases in $[Ca^{2+}]_c$ were produced via two methods with the aim of triggering CICR. Depolarising the plasma membrane of DRG neurones for 1 second (a & b) produced increases in $[Ca^{2+}]_c$ of 2.7 ± 0.7 µM (n = 10); while a train of ten 50 msec depolarisations (c & d) increased $[Ca^{2+}]_c$ by 3.3 ± 1.4 µM (n = 10). Both of these are significantly larger than the increases in $[Ca^{2+}]_c$ from 50 msec depolarisations of 0.96 ± 0.17 µM (n = 32). Despite these large increases in intracellular Ca^{2+} concentration, no CICR was observed. Figures show normalised linescan images and plots of normalised fluorescent changes averaged along the scan line for both protocols.

3.4.3 Caffeine

Many studies have pointed to caffeine releasing Ca^{2+} from ryanodine-sensitive intracellular stores by increasing the ryanodine receptor's sensitivity to Ca^{2+}, such that they can be activated by basal Ca^{2+} concentrations (Friel and Tsien, 1992; Usachev *et al.*, 1993b; Shmigol *et al.*, 1996; Ayar and Scott, 1999; Albrecht *et al.*, 2001).

To try and induce CICR in E12 chick DRG neurones, I added 5 mM caffeine to the extracellular solution. The cells were then patched with a pipette containing a potassium-based intracellular solution and depolarised in the normal way for both 50 msec and 1 second; the data was analysed as in section 3.2. The results showed no significant spatial or temporal variation in the Ca^{2+} dynamics when compared against control experiments and the delay in the Ca^{2+} diffusion through the cytosol to the centre of the cells was statistically unchanged at 31 ± 7 msec (n = 5) compared against control experiments performed with a potassium-based intracellular solution which resulted in a delay of 27 ± 4 msec (n = 27; P = 0.7069). An example of this is shown in figure 3.5 a,b. The experiments were repeated using the standard caesium-based pipette solution with 5 mM caffeine in the extracellular solution, producing statistically similar delays of 37 ± 10 msec (n = 4; P = 0.6222 compared against caesium-based controls). Attempts to expose the cells to puffs of caffeine whilst in the whole-cell configuration were unsuccessful disrupting the patch clamp seal resulting in significant increases in intracellular Ca^{2+}.

3.4.4 Thapsigargin

Thapsigargin acts on the ATP-dependent Ca^{2+} pump (Ca^{2+}-ATPase) on the endoplasmic reticulum blocking the uptake of Ca^{2+} into the organelle (Thastrup *et al.*, 1990; Holliday *et al.*, 1991; Shmigol *et al.*, 1995a; Hongpaisan *et al.*, 2001). This provides an inhibitor for CICR by preventing the intracellular stores from loading with Ca^{2+}.

Thapsigargin was applied to the extracellular solution of DRG neurones in concentrations of 1 μM and 100 nM for 30 minutes. However, following depolarisations of both 50 msec and 1 second, the linescan images showed radial diffusion patterns very similar to those seen in control cells as well as those performed in the presence of 5 mM caffeine. Figure 3.5 c,d shows the normalised rise in fluorescent intensity along the linescan following a 1 second depolarisation in two cells; one with 100 nM thapsigargin in the extracellular medium and the other with 5 mM caffeine. The plots show no significant spatial or temporal variation in the Ca^{2+} signal.

Analysis of the time taken for the Ca^{2+} signal to diffuse to the centre of the cells also showed no significant difference between depolarisations performed in the presence of thapsigargin and the control cells with a potassium based pipette solution (31 ± 8 msec ($n = 8$; $P = 0.6422$) for 1 μM thapsigargin, 43 ± 6 msec ($n = 7$; $P = 0.0678$) for 100 nM thapsigargin compared against a control value of 27 ± 4 msec ($n = 27$)).

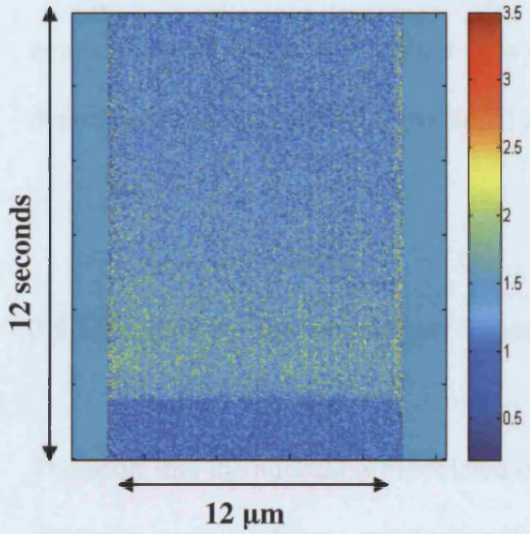

(a)

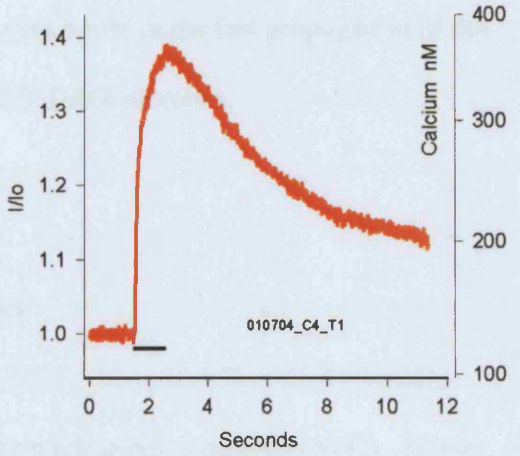

(b)

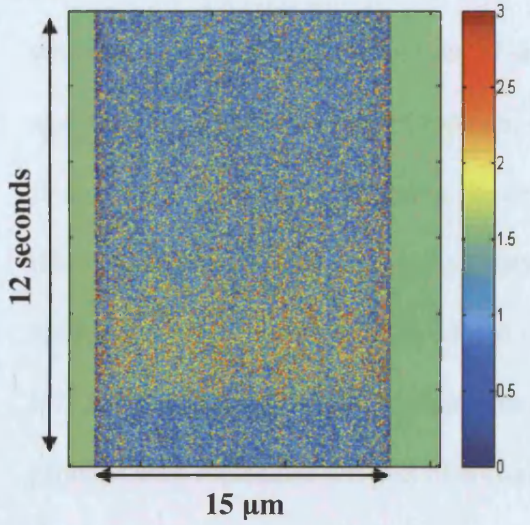

(c)

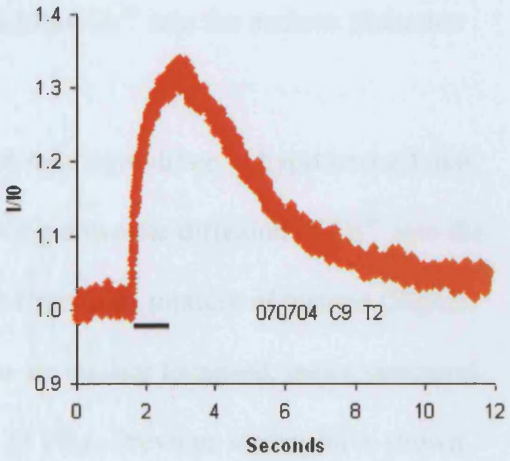

(d)

Figure 3.5 Use of caffeine and thapsigargin

In order to investigate the role of CICR in chick DRG neurones, cells were depolarised in the presence of 5 mM caffeine, which has been shown to promote CICR, and separately in the presence of 1 µM and 100 nM thapsigargin, shown to inhibit CICR. Linescan images performed in the presence of caffeine (a) and 1 µM thapsigargin (c), both using a potassium based pipette solution, show no variation from the standard radial diffusion pattern or in the time taken for the Ca^{2+} signal to diffuse to the centre of the cell. Comparisons of the intracellular Ca^{2+} dynamics at the centre of the cell also show no significant differences in either conditions (b and d). All plots shown here represent 1 second depolarisations.

All these results lead me to conclude that although CICR has been reported in other DRG neurones (Ayar and Scott, 1999), it does not play a role in the fast propagation of the depolarisation induced Ca^{2+} signal in E12 chick DRG neurones.

3.5 Effects of Histone on Nuclear Transport

Transport into the nucleus is modulated by the nuclear pore complex (NPC). These structures contain a large central granule allowing the passage of large molecules and proteins through the nuclear membrane. This is surrounded by numerous small pores which it is postulated allow the flow of small ions like Ca^{2+} into the nucleus (Schatten and Thoman, 1978; Wang and Clapham, 1999).

In order to transport large proteins, the central granule must dilate. I hypothesised that this would compress the surrounding pores, slowing down the diffusion of Ca^{2+} into the nucleus. To test this hypothesis, 33 μM of a heterogeneous mixture of histone (Sigma, H7755) was included in the patch pipette. These are nuclear localised, major structural proteins with molecular weights of around 32 – 33 kDa. Previous studies have shown that concentrations of 4 μM histone are sufficient to competitively block active transport of other proteins through the NPC (Schwamborn *et al.*, 1998). DRG neurones were patched in the normal way with a caesium-based patch solution also containing OG488BD. The cells were then left for three minutes for the Ca^{2+} indicator and histone to diffuse into the cell. The cells were depolarised for 50 msec from the holding voltage of -70 mV to +10 mV inducing a Ca^{2+} influx which was recorded through linescan

imaging in the normal way. The results from this were analysed as described previously; the measurements taken from 3 μm into the cell from each side compared to measure a delay in diffusion across the nuclear envelope. The delay due to the nuclear envelope was measured as 4 ± 3 msec (n = 27). Compared against the control value of 9 ± 2 msec (n = 38) this was found not to be statistically significant (P = 0.1122).

Studies have also indicated that depletion of nuclear Ca^{2+} stores with thapsigargin brings about a conformational change in the nuclear pore complex restricting molecular movement across the nuclear envelope (Stehno Bittel *et al.*, 1995; Perez Terzic *et al.*, 1996; Wang and Clapham, 1999). However, my analysis of the time taken for Ca^{2+} to diffuse into the nucleus in the presence of thapsigargin with a potassium-based internal solution shows no statistical difference to results taken with a potassium-based internal in the absence of thapsigargin; 22 ± 8 msec (n = 7) for 100 nM thapsigargin and 7 ± 4 msec (n = 9) for 1 μM thapsigargin compared against 10 ± 2 msec (n = 27) in the absence of thapsigargin (P = 0.0676 and P = 0.5172 respectively).

4 COMPUTATIONAL MODELLING

The experiments described in the previous chapter have shown that the fast diffusion of the Ca^{2+} signal to the centre of an embryonic chick DRG neurone is not an artefact of the whole-cell patch clamping technique, nor is it propagated by CICR. A further possibility exists; that it may be an artefact caused by the inclusion of a Ca^{2+} indicator dye. This acts as an additional mobile Ca^{2+} buffer and if replacing slower endogenous buffers may speed up the diffusion of the Ca^{2+} signal across the cell.

In order to investigate this I have used computational modelling to create a mathematical model of the intracellular Ca^{2+} dynamics.

Computational cell biology constitutes the generation of predictive models based on a collection of experimentally measured facts and hypotheses. Simulations run on these models allow us to test complex hypotheses and make predictions about how the biological system would behave under a variety of conditions; predictions that can, in turn, be verified experimentally.

The large number of degrees of freedom, such as position and velocity, presented by a system such as intracellular Ca^{2+} signalling makes it untenable to consider each molecule individually and instead a statistical deterministic approach can be used. At a microscopic level, classical systems such as diffusion can be represented as a stochastic system; one where the various events are governed by a degree of probability. At a macroscopic level, modelling attempts can be simplified by considering species populations instead of individual molecules, allowing a desired configuration to be

modelled as a probability distribution. These distributions can then be translated into concentrations for analysis.

Modelling diffusion within cells is a complicated issue, highly dependent on spatial scales, geometry and mobility of the various molecules and ions involved.

A number of previous studies have modelled diffusion in a variety of systems, including Markram *et al.* modelling Ca^{2+} diffusion in dendrites (Markram et al., 1998) and on smaller scales Naraghi and Neher who modelled Ca^{2+} microdomains around Ca^{2+} channels (Naraghi and Neher, 1997). Studies such as these have shown the importance of diffusion on molecular interactions.

Calcium interacting with intracellular buffers is a classic example of a reaction-diffusion system; that is a system where binding reactions are fast enough to affect the diffusion rate of individual species (Wagner and Keizer, 1994; Zador and Koch, 1994). These buffering interactions can have a significant effect on the diffusion of the Ca^{2+} ions within a cell, slowing it by up to ten times (Kasai and Petersen, 1994).

Various methods have been used to model the Ca^{2+} signalling system.

This chapter includes a description of the various modelling techniques, outlining the merits and limitations of each method, concluding with my approach to modelling intracellular Ca^{2+} diffusion.

4.1 Analytical Methods

Analytical modelling methods involve solving the reaction-diffusion equations governing the probability distribution of the various populations so that the concentration of species S can be directly calculated at each spatial position x,y,z and time t. One of the most widely used analytical methods is the finite difference method which has been used by a number of groups to model the problem of buffered Ca^{2+} diffusion (Sala and Hernández-Cruz, 1990; Nowycky and Pinter, 1993; Klingauf and Neher, 1997). These techniques typically involve numerous approximations resulting in large errors in any but the simplest systems.

4.1.1 Finite Volume Method

The finite volume method is used for solving partial differential equations. This method calculates the values of the variables within volume elements. These can then be averaged across the volume to get a population distribution. One advantage of the finite volume method over finite difference methods is that it does not require a structured mesh.

4.1.2 Monte Carlo Method

A Monte Carlo simulation, named after the Monte Carlo casinos where throwing a die generates a random number, is a general description of a model that uses pseudo-random-numbers generation to solve a particular process. The technique involves statistically sampling a population distribution in order to generate approximate solutions to a quantitative problem. Each iteration of the simulation generates one possible outcome; many outcomes can then be averaged to reveal the probability distribution of a particular event at a desired time. This stochastic approach is particularly useful when considering small numbers of molecules, where random behavioural fluctuations become important. In the case of Ca^{2+} dynamics, seemingly random events such as Ca^{2+} sparks can be modelled stochastically through random channel activation. Where a model contains stochastic and non-stochastic systems, Monte Carlo methods can provide a general solution. Although a fairly simple technique, this is a very computationally expensive method to use.

4.2 Spatial Modelling

Spatial models are used in situations such as cellular modelling to provide spatial co-localisation of interacting species within various compartments. In order to solve these types of models, fast, multi-dimensional numerical methods such as finite differencing or Monte Carlo methods are used.

All my models are run as spatial models, providing distinct compartments such as the cytoplasm and nucleus.

4.2.1 Boundary Conditions

Boundary conditions are required to limit the diffusion of the molecules or ions and to define their concentration profiles. When modelling intracellular Ca^{2+} diffusion, the majority of the boundary conditions are defined by the three-dimensional geometry of the cell and the computational domain within which it is defined.

4.3 Mathematics of Reaction-Diffusion Equations

Diffusion is the process by which random Brownian motion of molecules or ions cause an average movement towards regions of lower concentration. This is based on the assumption that all molecules or ions perform a random walk, such that they have an equal chance of moving in any direction. In the case of a concentration gradient, where there are more molecules in one volume element than in a neighbouring volume element, all molecules and ions still perform a random walk, however more molecules will tend to move from the volume element of higher concentration into its neighbour simply due to its initial larger population. This will cause the two volume elements to equilibrate in

concentration, at which point the average diffusion between them will be zero; an equal number of molecules or ions moving between the two elements.

This flow of ions or molecules is described in more detail by Fick's Law. This states that a concentration gradient gives rise to a flux of mass in the (diluted) solution (J), proportional to but in the opposite direction of the concentration gradient. The constant of proportionality is given by the diffusion constant, D ($\mu m^2 s^{-1}$). Mathematically, this can be written in one dimension as:

$$J(x,t) = -D\frac{\partial C(x,t)}{\partial x}$$

Equation 4.1

The flux is negative as the mass will flow down the concentration gradient upholding the second law of thermodynamics of entropy which tells us an isolated system always evolves to a state of higher entropy; that is towards a state of thermodynamic equilibrium characterised by a uniform density and an equilibrated concentration.

The problem of buffered Ca^{2+} diffusion in cells can be described by a series of reaction-diffusion differential equations. These govern the spatial and temporal evolution of the cellular components.

For a system containing Ca^{2+} and a number of buffers, which may include exogenous buffers (in my case the Ca^{2+} indicator Oregon Green 488 BAPTA-1 dextran) or endogenous buffers such as calbindin-D_{28k} or calmodulin, the first-order binding kinetics, describing how free Ca^{2+}

and the various buffers (B_i) interact to produce their Ca^{2+} bound forms, are given by equation 4.2.

$$[Ca^{2+}]+[B]\underset{k^r}{\overset{k^f}{\Leftrightarrow}}[Ca^{2+}B]$$

Equation 4.2

Where k^f and k^r are the forward and reverse reaction rates for the particular binding reaction.

This allows the generation of a set of ordinary differential equations (ODEs) that specify the rate of change of each species as a function of the concentrations of molecules in the system as shown in equation 4.3.

$$\frac{d[Ca^{2+}]}{dt}=\frac{d[B]}{dt}=\left(k^r[Ca^{2+}B]-k^f[Ca^{2+}][B]\right)$$

$$\frac{d[Ca^{2+}B]}{dt}=-\frac{d[B]}{dt}$$

Equation 4.3

The concentration of a system at any given position and time as determined by Brownian motion can be described mathematically by the diffusion equation, shown here in one-dimension in Cartesian coordinates.

$$\frac{\partial C(x,t)}{\partial t} = D\frac{\partial^2 C(x,t)}{\partial x^2}$$

Equation 4.4

where C(x,t) is the concentration of a particular molecule or ion with regards to position (x) and time (t) and D is the diffusion constant of the molecule or ion ($\mu m^2 s^{-1}$). A full derivation of the diffusion equation from the principle of Brownian motion can be found in Appendix A.

When considering radial problems such as the diffusion through a cell it becomes easier to consider the diffusion equation using spherical polar coordinates. Equation 4.5 shows the diffusion equation rewritten for three dimensions in spherical polar coordinates.

$$\frac{1}{r}\frac{\partial}{\partial r}\left(r^2\frac{\partial[Ca^{2+}]}{\partial r}\right)+\frac{1}{r^2\sin\theta}\frac{\partial}{\partial\theta}\left(\sin\theta\frac{\partial[Ca^{2+}]}{\partial\theta}\right)+\frac{1}{r^2\sin\theta}\frac{\partial^2[Ca^{2+}]}{\partial\phi^2}=\frac{1}{D}\frac{\partial[Ca^{2+}]}{\partial t}$$

Equation 4.5

where r and t are the spatial and temporal components respectively.

This partial differential equation (PDE) tells us how the particular component will diffuse spatially with respect to time.

This diffusion equation can be written for each component of the reaction scheme and, when combined with the previous equations governing the reactions, the resulting reaction-diffusion system allows us to describe how the various concentrations within a cell change with time and position.

Solving these reaction-diffusion equations forms the core of computational cell biology, allowing us to generate models of molecular behaviour inside cells.

4.4 The Virtual Cell

Developed at the University of Connecticut Health Center, The Virtual Cell (http://www.nrcam.uchc.edu/) provides a computational modelling environment specifically designed for the construction of biological models. Running as an applet in a web browser, The Virtual Cell allows collaboration between biologists and modellers through the ability to design models, both spatial and non-spatial, either through a mathematics description language (VCMDL) or via the BioModel workspace that provides a general toolbox of model components to specify membrane topology, molecular species, kinetic reaction expressions and membrane fluxes. The two approaches are compatible, such that a model set up using the BioModel workspace is automatically translated into a VCMDL version and as such can be modified using the Math workspace (Loew and Schaff, 2001; Slepchenko et al., 2003).

The complete model comprises of two main subsections; the BioModel and the geometry. The BioModel is where the topography of the model is created; the various compartments defined and the surrounding membranes identified. The molecular species are allocated within the individual compartments and their related reaction kinetics and membrane fluxes specified. This BioModel is then combined with a geometry to create an application. The geometries can be in one, two or three dimensions and created explicitly by an equation or imported from an experimental image. This separation of the physiological model from the geometry allows one model to be easily applied to a variety of geometries. Within the Application, the boundary conditions of the system, the initial conditions and parameter values (such as the diffusion constants and reaction rates) can

be specified. A single BioModel can be used to create several applications, each with its own geometry, boundary conditions and initial conditions.

Upon running the Application, a mathematical description of the model is generated. This MathModel can then be altered directly to adjust individual areas of the simulation. The simulations themselves are run on The Virtual Cell cluster of Compaq DS20 computers located in Connecticut, where the models and results are also stored in a database thus freeing up valuable hard drive space on the modeller's computer.

The results from the simulation can be viewed directly from the program, either displayed as a single 2D slice at a specific time or plotted against time along an arbitrary curve or set of points, or exported as comma-separated values or gif images. This allows the model results to be analysed in Matlab (Mathworks, Inc.) in exactly the same way as my experimental data, allowing a direct comparison to be made between the model results and the original data.

4.4.1 The Physics of The Virtual Cell

The underlying laws governing The Virtual Cell simulations are those of conservation. The spatial and temporal evolutions of the molecular species are controlled by mass conservation, whereby the rate of change in the concentration of a molecular species in a specific volume element is a direct result of the diffusion into and out of the element and reactions inside the element involving the molecular species. Similarly, electric charge conservation governs any changes in membrane potentials; obtained by summing the

molecular fluxes across the membrane involving charged ions with the capacitative currents.

These laws are expressed as a system of differential equations as described by Slepchenko *et al.* (Slepchenko et al., 2003).

As the biological model is developed, a large system of nonlinear, differential equations is created within an often irregular geometry. These cannot be solved analytically by any existing algorithms and so The Virtual Cell approximates the original equations with an algebraic system from which the values of variables can be calculated at selected time points over a predefined mesh. By reducing the time step and mesh size, the approximated algebraic solution should converge to that of the original differential system.

The inclusion of buffers, including the endogenous buffers and the fluorescent Ca^{2+} indicator, in the model provides an additional complication as the timescale for their binding reactions would be expected to be much faster than other reactions such as fluxes through the membranes. To solve these fast reactions would require integration over very short time steps dramatically increasing the computational time required to run the model. The Virtual Cell allows fast reactions to be dealt with separately from the rest of the system, using a pseudo-steady approximation for selected fast reactions. This splits the processes into two; first solving the fast processes using a short time step, and then solving the slow reactions using the instantaneous equilibrium to solve the relevant nonlinear algebraic equations (Slepchenko et al., 2000).

4.4.2 Algorithms for The Virtual Cell

Spatial models are solved within The Virtual Cell using a finite volume approach on a structured mesh. The concentration changes of the various species in each volume element of the mesh, with respect to time, are determined by the diffusion into and out of the element and reactions involving the species inside the element. Letting u_i, $i = 1,...,n$, be the concentrations of the various species, this reaction-diffusion system is described by equation 4.6.

$$\frac{\partial u_i}{\partial t} = \nabla \cdot (D_i \nabla u_i) + R_i \qquad i = 1,...,n$$

Equation 4.6

The first term on the right-hand side (∇) is merely the spatial PDE from the standard diffusion equation, represented in three dimensions, where D_i is the diffusion constant of the i^{th} species; the concentration of species i changing as the second differential with respect to position. The effect of all the reactions on species i is represented by the second term on the right-hand side, R_i. The effects of each reaction on the change in concentration with respect to time are found from the product of the number of molecules produced or consumed by the reaction with the rate at which this occurs. For the case of m different reactions, with rates v_j, $j = 1,...,m$, acting on the i^{th} species:

$$R_i = \sum_{j=1}^{m} \alpha_{ij} v_j \qquad i = 1,\ldots,n$$

Equation 4.7

where α_{ij} is the (i, j) element of the integer-valued stoichiometry matrix which represents how many molecules of the i^{th} species are produced or consumed due to the j^{th} reaction (Reder, 1988).

To contain each species within the given domain (Ω), the boundary condition is imposed such that there is zero flux at the borders of the domain.

$$\Delta u_i \cdot \mathbf{n} = 0 \text{ on } \partial\Omega \qquad i = 1,\ldots,n$$

Equation 4.8

Where $\mathbf{n}$ is the outward, normal vector on $\partial\Omega$.

Jump conditions are used to relate the species concentrations on different sides of the membranes. These describe the flux densities across membranes separating two compartments. As the equations governing concentrations result in second-order spatial derivatives, two jump conditions are needed for each species with non-zero diffusion coefficient, relating to concentration changes on either side of the membrane. Denoting the inside and outside of the cell as + and – respectively, the jump conditions at the membrane for species i are given by equation 4.9.

$$-\Delta u_i|_+ \cdot \mathbf{n} = g_+(u_i|_+, u_i|_-)$$
$$-\Delta u_i|_- \cdot \mathbf{n} = g_-(u_i|_+, u_i|_-) \qquad i = 1,\ldots,n$$

Equation 4.9

Where **n** is the outward, normal vector to the membrane and g_+, g_- are user defined functions of $u_i|_+$, $u_i|_-$ describing how species i moves into and out of the membrane with respect to its concentration on either side of the membrane (Schaff et al., 2001). In the case where the membrane cannot store a species, mass conservation tells us that the flux into and out of the membrane must be equal.

$$g_+ = g_- \equiv g$$

Equation 4.10

As the normal vector is defined to point out of the cell, the negative designation of the jump conditions defines a flux density flowing into the cell.

4.4.3 Geometry Definition within The Virtual Cell

The computational domain, Ω, is always rectangular in The Virtual Cell. In the three-dimensional case, this is divided up into an orthogonal grid of cubic voxels. Each voxel is allocated to a particular compartment within the user defined geometry based on the compartment that the majority of the voxel lies in. This can be seen in figure 4.1 where the plasma membrane is approximated by a step-like membrane of voxels.

This step-like approximation causes problems when calculating membrane fluxes, as the surface area of approximated membrane does not converge to that of the real membrane as the mesh is refined. To rectify this, The Virtual Cell includes a flux correction to ensure that the total flux across a membrane remains unchanged at any mesh size and that this value is the same as the flux across the original membrane.

The original flux density is defined in equation 4.8 as normal to the real membrane. Hence by normalising the equation to the approximated membrane, the corrected flux density of the i^{th} species across the k^{th} membrane element is given by:

$$\tilde{g} = g\left(u_i|_+, u_i|_-\right)\cos\theta_k \qquad i = 1,\ldots,n$$

Equation 4.11

Where θ_k is the angle that the normal to the real membrane makes with the normal to the membrane element (figure 4.1).

By defining the area of the k^{th} membrane element as A_k the corrected flux across the membrane is given by:

$$\tilde{J} = g\left(u_i|_+, u_i|_-\right)A_k \cos\theta_k \qquad i = 1,\ldots,n$$

Equation 4.12

To simplify the calculations, and avoid the need to calculate an exact normal for each membrane element, The Virtual Cell applies a correction to the area of the membrane element, such that:

$$\tilde{A} = A_k \cos\theta_k$$

Equation 4.13

This can be stored when sampling the geometry and reused to calculate the membrane fluxes.

It has been shown that using this correction method ensures the convergence of $\tilde{u}_i$ to u_i (Schaff et al., 2001).

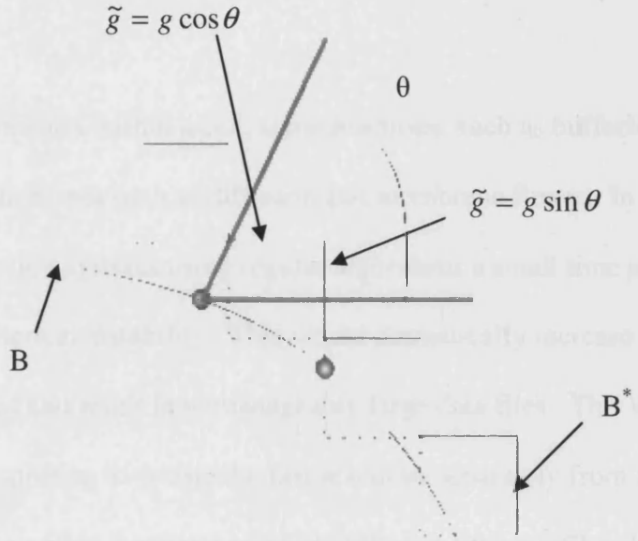

Figure 4.1 Basic scheme for flux correction

Membrane boundary B is approximated by the step-like boundary B^*. Even at very small mesh sizes, the surface area of B^* will not converge on that of B, necessitating a correction function for any fluxes across the membrane. The flux density is made normal to B^* by multiplying the original flux density by $\cos\theta_k$ where θ_k is the angle that the normal to B makes with the membrane element *k*. The corrected membrane flux is calculated by multiplying this new flux density by the area of membrane element *k*, A_k. Adapted from Schaff *et al.* 2001

4.4.4 Fast Processes in Reaction-Diffusion Systems

When modelling Ca^{2+} dynamics within a cell, some reactions, such as buffering, occur on much faster time scales than ones such as diffusion and membrane fluxes. In order to solve these reaction-diffusion systems using regular algorithms a small time step would be needed to prevent numerical instability. This would dramatically increase the computation time required and result in unmanageably large data files. The Virtual Cell uses a technique of time splitting to update the fast reactions separately from the slow ones whilst still remaining within a general reaction-diffusion scheme (Slepchenko et al., 2000).

A typical time step, Δt, is advanced in two stages; the first updating the fast reactions, with rates $v_1,...,v_k$ $(k \leq m)$, by solving:

$$\frac{\partial u_i}{\partial t} = \sum_{j=1}^{k} \alpha_{ij} v_j \qquad i = 1,...,n$$

Equation 4.14

for reactions j=1,…,k

The resulting concentrations for each species, $\tilde{u}_i(x)$, are then used as initial conditions for the slower reactions (j=m-k,…,m), which are updated by solving equation 4.15.

$$\frac{\partial u_i}{\partial t} = D_i \Delta^2 u_i + \sum_{j=k+1}^{m} \alpha_{ij} v_j \qquad i = 1,\ldots,n$$

Equation 4.15

The result from this is an approximation to $u_i(x, T + \Delta t)$. These two stages, described by equation 4.14 and 4.15, are then repeated to calculate the concentrations at subsequent times.

5. ACQUIRING DATA FOR MODELLING

In the previous chapter I have outlined the principles behind computational modelling. I have used these techniques to generate a three-dimensional, computational model of the intracellular Ca^{2+} dynamics following a 50 msec depolarisation. This chapter describes the experiments I have performed to measure more accurate values for many of the parameters included in my model.

5.1 Dye Concentration by Tetramethylrhodamine Dextran Loading

To avoid rundown of Ca^{2+} currents and loss of cellular constituents, Ca^{2+} diffusion measurements were made soon (typically 3 minutes) after achieving the whole-cell patch clamp mode. At this time, OG488BD was still diffusing into the cell from the pipette. To estimate the concentration of OG488BD in the cell at the time of the Ca^{2+} diffusion measurements, 100 μM tetramethylrhodamine dextran (TRITCD; 10,000 MW) was included in the patch pipette. I have assumed that as both this Ca^{2+}-independent indicator (excitation wavelength 554 nm) and OG488BD are conjugated to dextrans of identical molecular weight, they would load into the cytosol and nucleus at the same rate. The patched cell was imaged every 30 seconds, before and after the depolarisation experiment. By selecting a region of interest covering the whole cell, a graph of the fluorescent increase in TRITCD signal can be plotted against time. Subtracting the true background value from each of the fluorescent values creates a loading curve relevant for

both indicators (figure 5.1). I have assumed that the asymptotic value of the curve corresponds to a dye concentration of 100 μM as found in the patch pipette. This allows me to interpolate the concentration of indicator inside the cell at the time of the depolarisation. When the fluorescent intensity in regions corresponding to the cytoplasm and nucleus were plotted, the intensities were seen to increase in parallel, with no measurable lag in the nuclear signal (figure 5.2). In contrast to OG488BD (figure 2.4a) and calcein (figure 5.4), the nucleus usually appeared darker by TRITC fluorescence (figure 5.2).

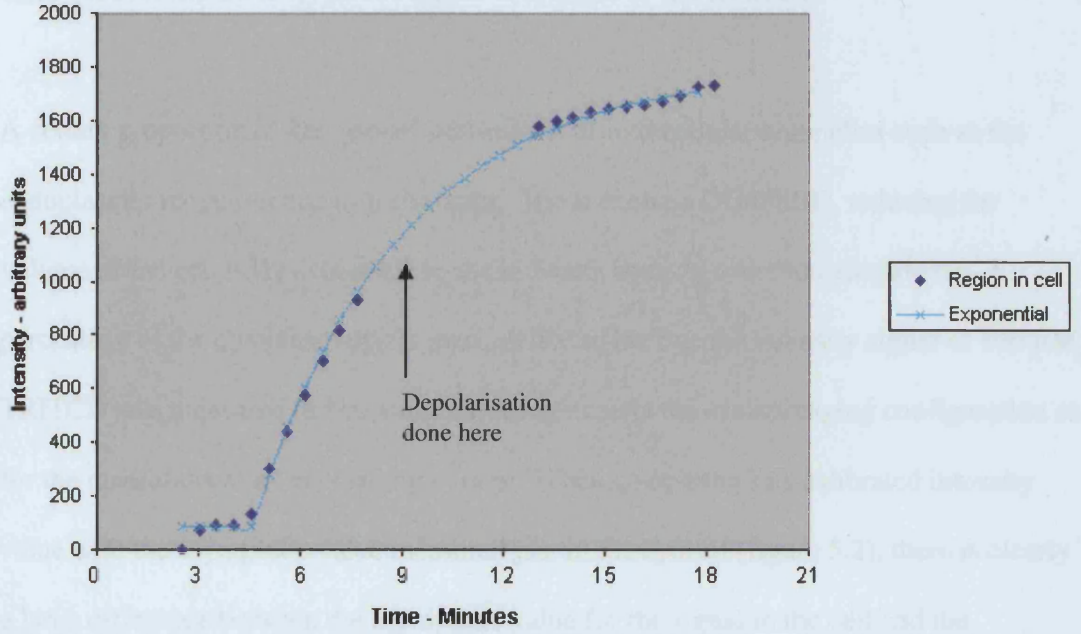

Figure 5.1 Measurement of indicator concentration

Plot of increasing fluorescence signal of tetramethylrodamine dextran (TRITCD) from exemplar cell 120504, imaged every 30 seconds after going whole-cell. An exponential curve of time constant 250 s^{-1} and with an asymptote of 1700 arbitrary intensity units has been fitted to the data. If we assume that the asymptote represents the signal I would get from the cell when cytosolic TRITCD was 100 μM, then the intensity of 1026 arbitrary units measured from the graph at the time of depolarisation indicates that the cytosolic TRITCD concentration was then 57.3 μM. Assuming Oregon Green 488 BAPTA-1 dextran loads the cell at the same rate as the TRITCD, the concentration of OG488BD at the time of depolarisation will be the same as TRITCD (in this example 57.3 μM). The initial rise in TRITC fluorescence was due to a prior attempt to go into the whole-cell configuration. This resealed, but not before allowing a small amount of dye to enter the cell.

5.1.1 Measurement of Cytosolic Space Available to the Indicator

A certain proportion of the cytosol will consist of intracellular organelles such as the endoplasmic reticulum and mitochondria. These exclude OG488BD, reducing the volume of the cell body accessible to the indicator dye. In order to calculate the percentage of the cytoplasm that is inaccessible to the dye the intensity signal of 100 μM TRITCD was measured in free solution, using exactly the same imaging configuration as for the measurement of the loading curves. When comparing this calibrated intensity value with the asymptotic value measured just in the cytosol (figure 5.2), there is clearly a large difference between the asymptotic value for the signal in the cell and the calibrated intensity value for 100 μM of the indicator. I have assumed that this is due to the presence of intracellular organelles that exclude the indicator dye thus reducing the average intensity signal. From this it is possible to estimate the percentage of the cytosol that is available for loading with the Ca^{2+} indicator. Over five cells the average percentage of the cytosol that is available to the indicator is 47.5 ± 5.1 %
(mean ± SEM; n = 5).

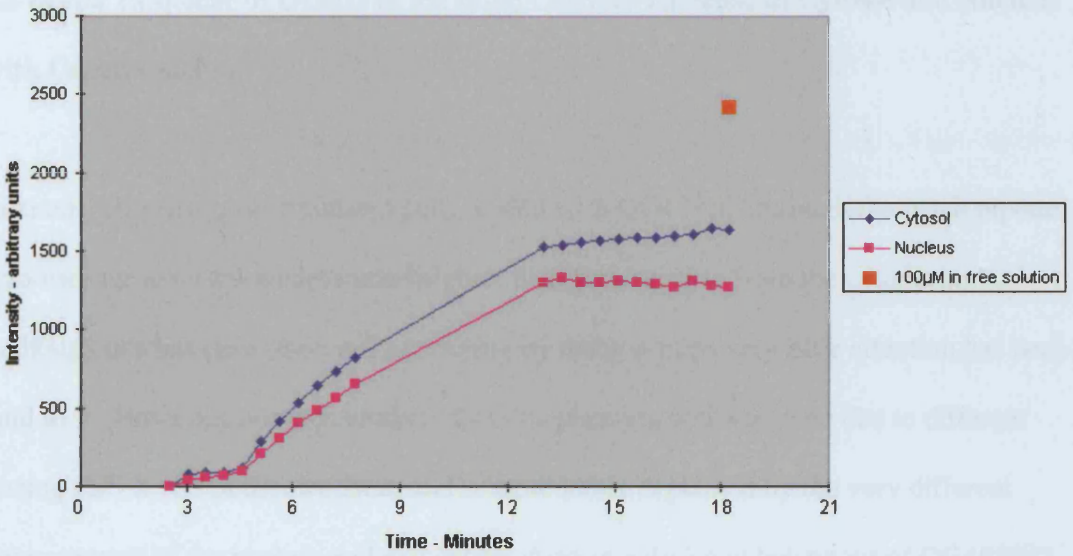

Figure 5.2 Loading curves of TRITCD for cytosol and nucleus

Plot of increasing fluorescence signal of tetramethylrodamine dextran (TRITCD), imaged every 30 seconds after going whole-cell, in 2 regions of interest covering the cytosol and the nucleus respectively. Both regions clearly exhibit the same pattern of loading. Comparison of the asymptotic intensity level in the cytosol with the intensity of 100 µM TRITCD in free solution allows me to calculate the proportion of the cytosol that is available to the indicator dye. In this example, from cell 120504, 62 % of the cytosol is available to the indicator dye and I have assumed the remaining 38 % is made up of intracellular organelles such as the ER. The standard caesium-based internal solution, as described in section 2.3.2.1 was used in all experiments.

5.2 *In situ* Response of OGBD to the same Calcium Increase in Cytosol and Nucleus with Caged Calcium

In almost all resting, unstimulated cells loaded with OG488BD through the patch pipette, fluorescence from the nucleus was brighter than fluorescence from the cytoplasm. Although this has been observed previously by many groups very little attention has been paid to it. However, it seems unlikely that this phenomenon would be due to different resting Ca^{2+} levels in the two areas and is more likely explained by the very different environments of the nucleus and cytosol resulting in a different behaviour of OG488BD in the two regions. That the properties of the dyes can be affected by the different environments of the two regions is reinforced by the behaviour of calcein (figure 5.4), where the nuclear region is clearly brighter than the cytoplasm, and TRITCD, where the nucleus appears dimmer than the cytoplasm (figure 5.2). At the concentrations used in these cells, calcein does not act as a Ca^{2+} indicator implying that the difference is environmental rather due to a difference in Ca^{2+} concentration.

This might result in the relationship between Ca^{2+} concentration changes and fluorescence changes ($dI/d[Ca^{2+}]$) being different in the two regions. To compare $dI/d[Ca^{2+}]$ in the two regions I used whole-cell patch clamp techniques to introduce 0.5 mM of a caged form of calcium, Ca^{2+} bound to the chelator NP-$EGTA^{2-}$ (Molecular Probes, N6802), into the cell via a patch pipette, also containing 100 μM OG488BD. Whilst bound to the chelator, the Ca^{2+} is inert, unable to interact with proteins and molecules inside the cell. However, illumination by an ultraviolet source dramatically increases the chelator's dissociation constant for Ca^{2+}, releasing the free ion. This

provides a controlled way to introduce a large quantity of free Ca^{2+} across the interior of a cell at a given time. Assuming the cell is uniformly filled with Ca^{2+}:NP-$EGTA^{2-}$, the same concentration of free Ca^{2+} will be released at all locations within the imaged plane of the cell, both in the cytosol and the nucleus. Even after partial photolysis, the remaining NP-$EGTA^{2-}$, together with the OG488BD, dominates local Ca^{2+} buffering, ensuring that the change in [Ca^{2+}] is the same in all locations. If the indicator dye behaves identically in the cytoplasm and the nucleus, this should result in a uniform increase in OG488BD fluorescence across the cell.

Once whole-cell, the system was left for three minutes to allow sufficient amounts of the caged Ca^{2+} and OG488BD to enter the cell. From the experiments with TRITCD in section 5.1, I have seen that three minutes provides enough time for the concentrations of 10 kD dextran associated indicators in the nucleus and the cytosol to equilibrate. I have assumed that the concentration of the considerably smaller (653.81 Da) NP-$EGTA^{2-}$ has also equilibrated in the two regions after three minutes. The cell was uniformly illuminated with ultraviolet radiation, simultaneously releasing an equal concentration of free Ca^{2+} into the nucleus and cytoplasm. This allows the fluorescent response of the Ca^{2+} indicator in both regions to be compared. In performing these experiments I have assumed the uncaging is similar in the different environments presented by the nucleus and the cytosol. The UV power used to uncage the Ca^{2+} was set such that the resulting fluorescent changes were similar in amplitude to those seen following 50 msec depolarisation and well below the indicator dye saturation.

In all the measured cells, it appeared that the peak fluorescence was greater in the nucleus than in the cytosol (figure 5.3). However, by measuring the peak rise in normalised

intensity in the cytosol and the nucleus it was found that the change in nuclear fluorescence was larger than that in the cytosol by only 3.09 ± 0.8 % (n = 9; mean ± SEM).

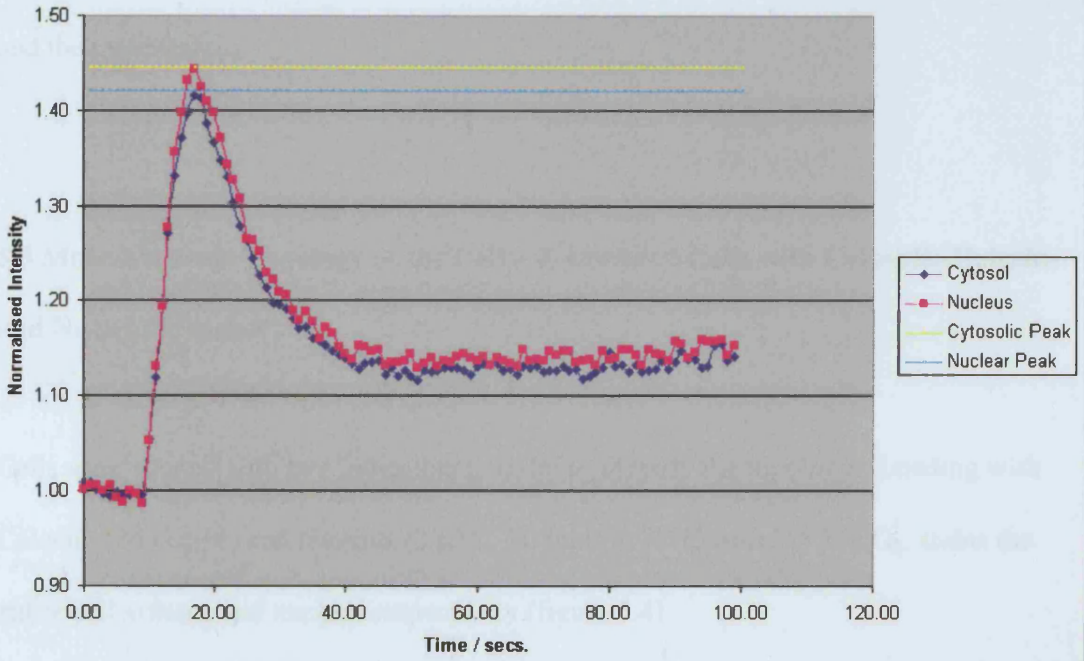

Figure 5.3 Oregon Green 488 BAPTA-1 Dextran response to photo-release of caged Ca^{2+}
Normalised fluorescence intensity increases of Oregon Green 488 Bapta-1 dextran in the nucleus and cytosol of a DRG neurone in response to the release of caged Ca^{2+} uniformly over the entire cell showing a 2.5 % larger increase in fluorescent intensity in the nucleus than in the cytosol to equal increases in free Ca^{2+}.

The same measurements were performed replacing the caesium-based solution in the patch pipette with a potassium-based one. The same phenomenon was seen (n = 8). No significant difference was found between the measurements made with the caesium- and potassium-based patch solutions (P = 0.7376).

Using both internal solutions, I measured significantly higher fluorescence rises in the nucleus compared against the cytoplasm ($P = 0.0029$, $P = 0.0026$ for Cs^+- and K^+-based patch solutions respectively). However, the 3 % difference between nucleus and cytosol is a small one and hence not included in the model and I have assumed that, when normalised, the indicator dye reports Ca^{2+} changes in an identical way in both the nucleus and the cytoplasm.

5.3 More Accurate Topology of the Cell – Z-stacks of Cells with Cytosolic Calcein and Nuclear Hoechst

Cells were stained with two indicators in order to identify the topology. Loading with Calcein AM (2 μM) and Hoechst (2 μM), 30 mins at 37°C with 2.5 % CO_2, stains the entire cell volume and nucleus respectively (figure 5.4).

This enables confocal z-stacks (a series of x/y plane scans taken at increasing z-position through the sample, combined to make a three-dimensional image; see section 2.4.2.2) to be taken, clearly showing the precise location of the nucleus within the cytosol. All the DRG neurones showed a similar topology, with the nucleus at one end of the cell, separated from the plasma membrane by a small gap as shown in figure 5.4. In order to produce a value for this distance between the nuclear envelope and the plasma membrane, the average value was measured from 13 imaged cells, resulting in a value of 0.29 ± 0.03 μm (mean ± SEM; $n = 13$).

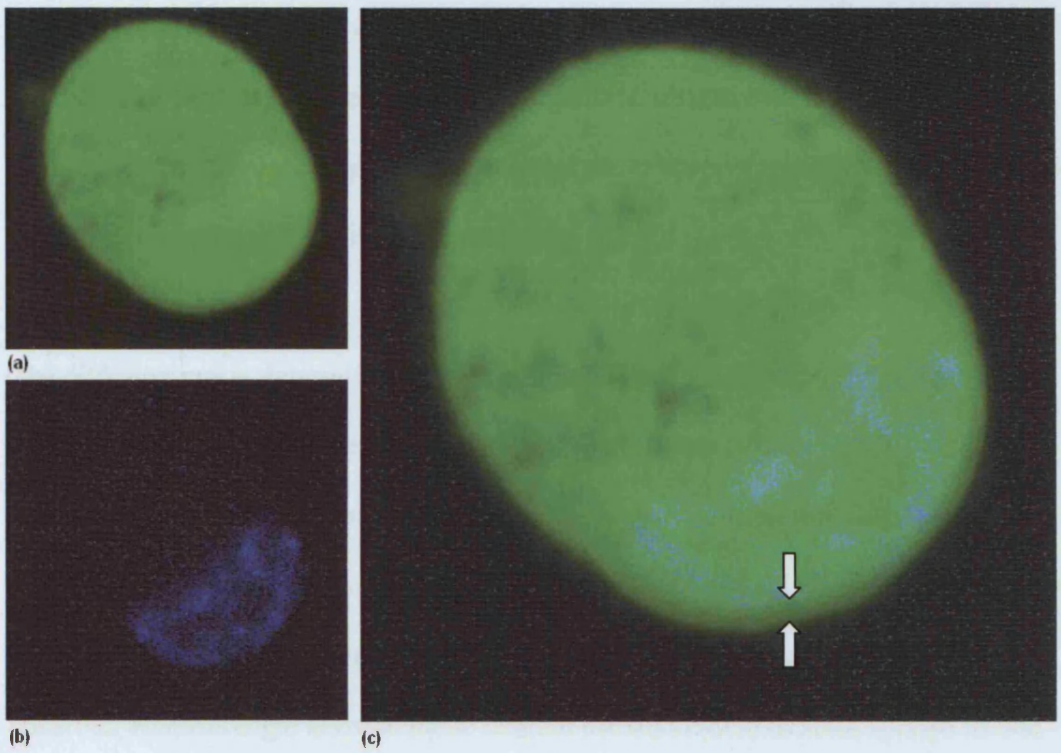

Figure 5.4 Identifying the topology of DRG neurone

DRG neurone AM-loaded with 2 μM calcein (a) and the nucleus stained with 2 μM Hoechst (b). The overlaid image (c) enables an average value of the gap between nuclear and plasma membranes (indicated by the white arrows) to be measured as 0.29 ± 0.03 μm.

5.4 Dextran Diffusion Rate by Caged Fluorescein

In order to measure the diffusion rate of a 10 kD dextran, such as our Ca^{2+} indicator Oregon Green 488 BAPTA-1 dextran, a caged form of fluorescein dextran (MW 10 kD; Molecular Probes) was introduced into a DRG neurone via a patch pipette on the stage of the Zeiss confocal microscope. This dextran conjugate is non-fluorescent until uncaged by illumination in the ultraviolet. The CLSM software of the Zeiss confocal allows a specific region of interest to be defined and exposed to the ultraviolet radiation producing

a highly localised release of caged molecules. I used this to generate ultraviolet photolysis over half of the cell. Taking x/y confocal images every 100 msec; before, during and after the uncaging process; allowed me to observe the diffusion of the released fluorescein dextran as it equilibrated across the cell.

The diffusion rate is determined by measuring the rise in fluorescent intensity at two points within the cell outside of the photolysis area (figure 5.5a).

In order to extract a diffusion constant for a 10 kD dextran from this data, a series of models were created in the modelling environment The Virtual Cell (fully described in section 4.4). Each experimental cell was approximated algebraically as a simple spheroid; Boolean logic allowed me to contain the fluorescein dextran species in one section of the cell body at time zero, from where it can freely diffuse as in the experimental case. The results from the model were analysed in the same manner as the experimental data; observation at the same z-position within the cell, the increase in the fluorescein dextran species was measured from two regions positioned as in the experimental data. The initial concentration and diffusion constant of the modelled dextran can then be adjusted to fit the fluorescent increase measured in the experimental data (figure 5.5b).

Over 4 experiments an average value for the diffusion constant of a 10 kD dextran was measured to be $D = 36 \pm 4.7\ \mu m^2\ s^{-1}$ (mean ± SEM; N = 4), a value roughly 10-fold lower than that of Ca^{2+}.

.

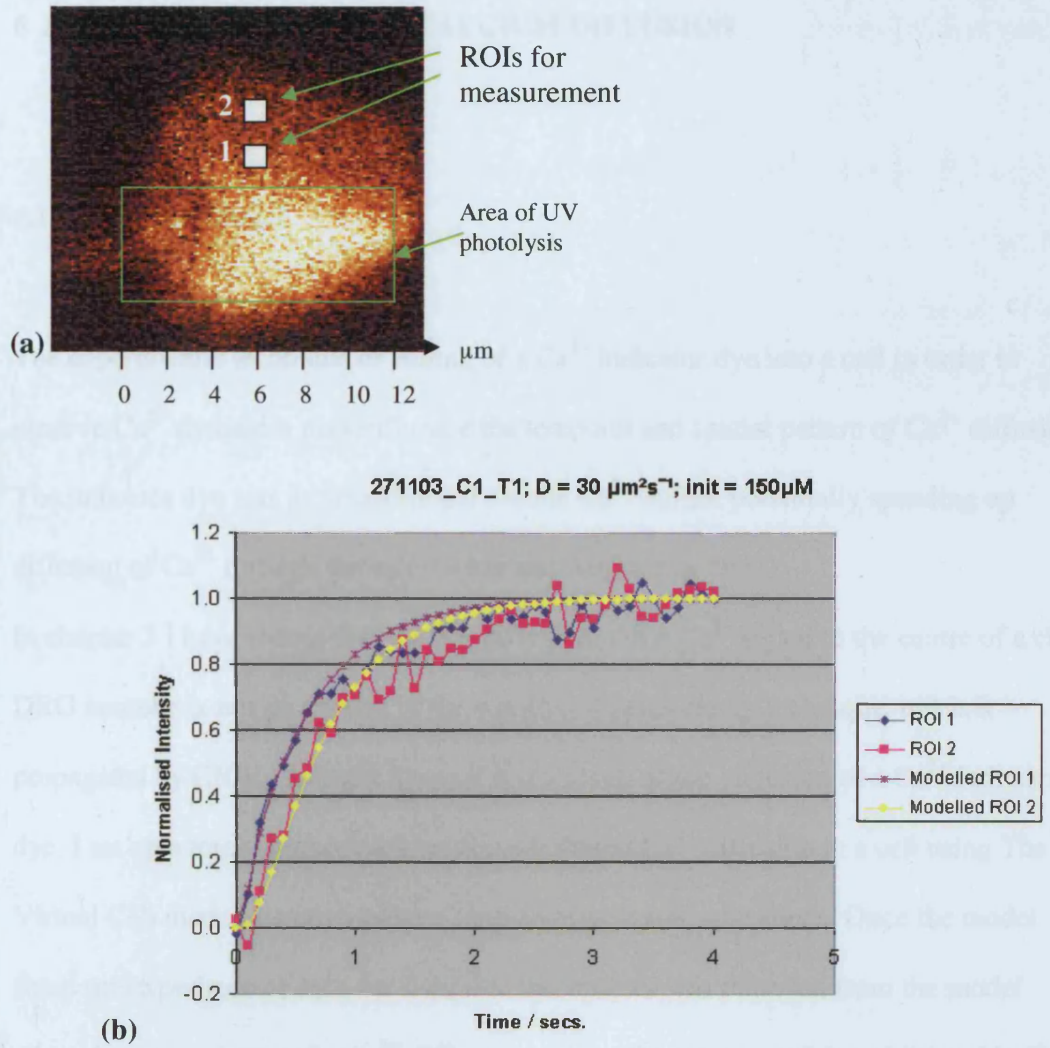

Figure 5.5 Measurement of dextran diffusion constant

(a): Confocal image of a DRG neurone filled with caged fluorescein via a patch pipette. The image shows the cell immediately after the fluorescein is uncaged by UV photolysis over the lower half of the cell (green square). A series of images were taken every 100msecs in order to observe the diffusion of the fluorescein as it equilibrates across the cell. Two regions of interest are selected outside of the photolysis region (shown in image (a)) and the fluorescent increases at each plotted ((b); normalised to the asymptotic value) clearly showing the delay due to diffusion between the two areas. A computer model was used to extract a diffusion constant from the data as described in the text. (b) shows the modelled increase in fluorescence due to the diffusion of uncaged fluorescein. The results from the model are taken from 2 points the same distance from the fluorescein release area as the measurements from the experimental data. The diffusion constant and initial concentration of fluorescein dextran have been adjusted in the model to fit the experimental data (plotted here with an initial concentration of 150µM and diffusion constant of $30\mu m^2s^{-1}$).

6 MODELLING BUFFERED CALCIUM DIFFUSION

6.1 Aim of the Model

The experimental technique of adding of a Ca^{2+} indicator dye into a cell in order to observe Ca^{2+} dynamics may influence the temporal and spatial pattern of Ca^{2+} diffusion. The indicator dye acts as an additional mobile Ca^{2+} buffer, potentially speeding up diffusion of Ca^{2+} through the cell (Neher and Augustine, 1992).

In chapter 3 I have shown that the fast diffusion of the Ca^{2+} signal to the centre of a chick DRG neurone is not an artefact of the whole-cell patch clamp technique, nor is it propagated by CICR. In order to see if it is a result of the inclusion of a Ca^{2+} indicator dye, I set up a three-dimensional model of buffered Ca^{2+} diffusion in a cell using The Virtual Cell modelling environment (http://www.nrcam.uchc.edu/). Once the model fitted the experimental data, the indicator dye species was removed from the model allowing me to observe the Ca^{2+} diffusion without the presence of the additional buffer.

6.2 Model Development

In order to generate accurate descriptions of cellular processes I have created models based on the experimental data obtained from five exemplar cells whole-cell patch clamped with pipettes containing a caesium-based patch solution, OG488BD and

TRITCD. The cells were depolarised for 50 msec and imaged using the linescan setting of the Zeiss confocal microscope as described in section 2.4.2.1.

These cells were selected as those with a good Ca^{2+} influx in response to a 50 msec depolarisation resulting in a clear spatial Ca^{2+} signal with little contaminating noise, a clearly defined geometry and successful loading with TRITCD, requiring the whole-cell patch to be maintained for around 20 minutes, providing a value for the concentration of Ca^{2+} indicator in the cell at the time of depolarisation. The cells and corresponding models are identified here by the date on which experiments were performed; thus the five cells and models are labelled 120504, 240604, 221204, 140105 and 190105 in a day-month-year format.

6.3 Properties of Modelled Species

The physical properties, such as initial concentration, diffusion and reaction rates, for each species have been compiled through a mixture of experimental methods and from values taken from previous literature.

The experimentally derived values have been described in section 5. Here I will briefly describe the source of values taken from the literature and present a summary of all the values. While in most cases it has not been possible to find values from the same cell type and / or species, an effort has been made to find the closest match or to translate published values from other cell types into realistic values for chick DRG neurones.

6.3.1 Properties of Intracellular Free Calcium

The resting concentration of Ca^{2+} in chick DRG neurones was measured experimentally as 129 nM using fura dextran as described in section 3.1. The diffusion constant for free Ca^{2+} inside cells has been taken from Allbritton *et al.*, who present a value of 233 $\mu m^2 s^{-1}$ in Xenopus laevis oocytes (Allbritton *et al.*, 1992). This is significantly slower than a measured value for the diffusion of Ca^{2+} in water of 792 $\mu m^2 s^{-1}$ provided by Lide due to the increased density of cytosol and associated path tortuosity compared to water slowing down the diffusion of the ions (Lide, 1993-1994).

As the basis of a reaction-diffusion model, free Ca^{2+} binds competitively with other species in the model. For reasons of simplicity, these are restricted to an endogenous buffer species, representing the Ca^{2+}-binding proteins inside the cell, ATP as introduced through the patch pipette and the Ca^{2+} indicator dye Oregon Green 488 BAPTA-1 dextran.

6.3.2 Properties of the Mobile Endogenous Buffer

Two main endogenous buffers, calbindin-D_{28k} and parvalbumin, have been reported to be expressed in sensory neurones (Honda, 1995). I have modelled the endogenous Ca^{2+} buffers found in DRG neurones by one species. This is based on the common Ca^{2+} buffer calbindin-D_{28k} (CaB). The concentrations of CaB and other Ca^{2+} buffers inside neurones

vary from cell to cell. As a result, the concentration of endogenous buffer is a variable that can be adjusted to fine-tune the model. This showed a large variation in the concentration of endogenous buffer in the cells, with values ranging from under 10 μM to almost 200 μM.

CaB is capable of binding up to four molecules of Ca^{2+} with at least two different binding kinetics; via high-affinity binding sites with k_{on} for Ca^{2+} of approximately 1 x 10^7 M^{-1} s^{-1} and another with lower affinity and an approximately eight-fold faster k_{on} (Nägerl *et al.*, 2000; Berggård *et al.*, 2002). However, for simplicity, I have based my reaction of the binding of Ca^{2+} to the endogenous buffer on a more basic model proposed by Nägerl *et al.* in which all Ca^{2+}-binding sites are identical with k_{on} for Ca^{2+} of 23.7 μM^{-1} s^{-1} and a k_d of 158 nM. Nägerl *et al* have shown that after the first 2 msec of simulation time, their simplified model produces a good approximation to the more complicated multiple-binding-site model, resulting in a good fit to their experimental data (Nägerl *et al.*, 2000).

The diffusion constant for CaB has previously been measured in cerebellar Purkinje neurones as 20 μm^2 s^{-1} (Schmidt *et al.*, 2005).

I have also tried parvalbumin, as the model for endogenous Ca^{2+} buffering. However, as reported in section 6.10, the results indicate that parvalbumin is unlikely to be the dominant endogenous Ca^{2+} buffer in any of the five exemplar cells.

As in many previous models of buffered Ca^{2+} diffusion (Sala and Hernández-Cruz, 1990; Nowycky and Pinter, 1993; Gil *et al.*, 2000), the decision to model the endogenous Ca^{2+} buffers as a single species is based primarily on the desire to keep the number of parameters to a minimum. As the total buffer concentrations are unknown and with the

uncertainties in the buffer kinetics, having a single species helps reduce the number of estimations that would arise from having a selection of buffers with individual diffusion constants and Ca^{2+}-binding rates. As described in the introduction (section 1.5.1.2), CaB is found throughout the CNS, responsible for buffering Ca^{2+} entering the cytoplasm through plasma membrane Ca^{2+} channels and so makes a good candidate for a mobile, endogenous buffer in my models.

6.3.3 Properties of the Calcium Indicator Dye

The k_d of the Ca^{2+} indicator dye, OG488BD, has been calibrated for each batch as described in section 2.2.2.3. Two dye batches were used throughout my experiments with k_d's of 1.833 and 1.567 μM. I have assumed the k_{on} for the Ca^{2+} indicator is the same as the k_{on} for BAPTA, taken from Rintoul *et al.* as 600 $\mu M^{-1} s^{-1}$ (Rintoul *et al.*, 2001), resulting in k_{off}'s of 1100 and 940.2 s^{-1} respectively.

The diffusion constant of OG488BD has been derived experimentally as 36 $\mu m^2 s^{-1}$ by release of a caged fluorescein dextran conjugate with an identical molecular weight as the Ca^{2+} indicator. This is explained in detail in section 5.4.

6.3.4 Properties of Intracellular ATP

ATP acts as only a minor Ca^{2+} buffer but is included in my model for completeness. The cytosolic concentration is taken to be 4 mM, as included in the patch pipette, with a diffusion constant of 140 $\mu m^2\ s^{-1}$ taken from previous work by Baylor and Hollingworth (Baylor and Hollingworth, 1998). This paper also provides values for the reaction rates of Ca^{2+} and magnesium binding to ATP as k_{on} of 150 $\mu M^{-1}\ s^{-1}$ and 1.5 $\mu M^{-1}\ s^{-1}$ and k_{off} of 30,000 s^{-1} and 150 s^{-1} for Ca^{2+} and magnesium respectively.

6.4 Plasma Membrane Channels and Pumps

By default, membranes defined within The Virtual Cell are impermeable to all species. In order to move populations across the membranes, pathways representing channels and pumps must be created. How these pathways transport species is explicitly defined representing passive diffusion controlled by concentration gradients, gated channels responding to external stimulus or active pumps coupled to another species regulating or powering its action.

In my model, Ca^{2+} influx across the plasma membrane in response to the opening of voltage-gated Ca^{2+} channels is modelled by a population of Ca^{2+} channels allowing passage for Ca^{2+} from the extracellular domain into the cytosol. In turn, a population of

Ca^{2+} pumps is used to return the Ca^{2+} levels to resting levels. An inward leak current is included to ensure $[Ca^{2+}]_i$ remains stable in resting situations (figure 6.1).

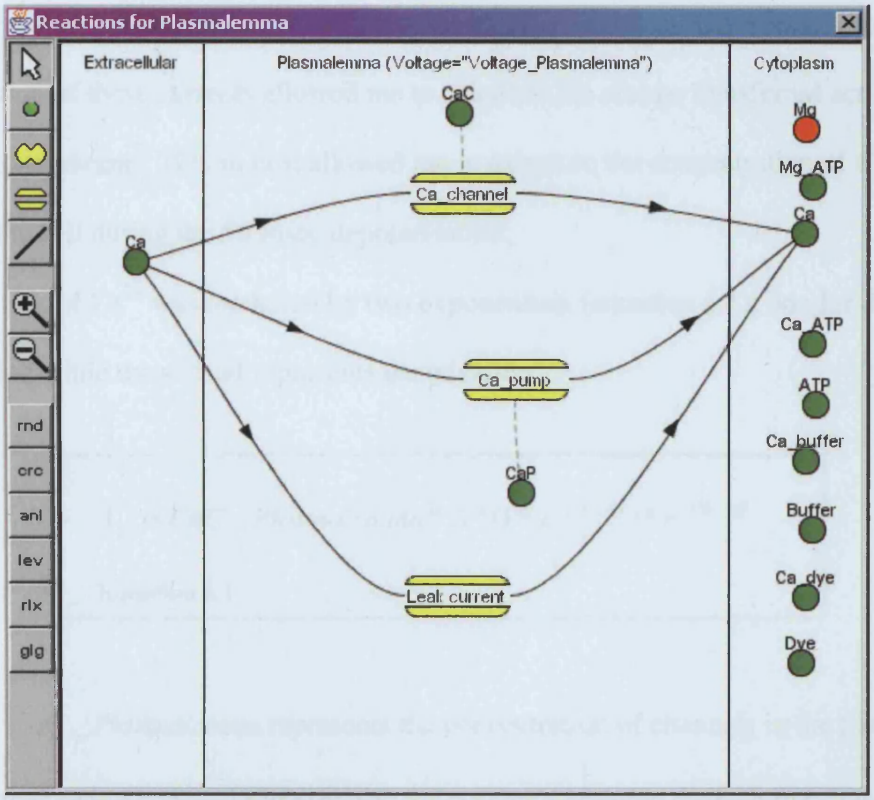

Figure 6.1 Modelling voltage-gated Ca^{2+} channels and plasma membrane pumps

Voltage-gated Ca^{2+} channels and Ca^{2+}-ATPases were included in the model to transport Ca^{2+} ions across the plasma membrane. The population of Ca^{2+} channels are explicitly defined so as to transport a set concentration of Ca^{2+} ions from the extracellular space into the cytosol as specified by the experimentally measured current traces. This is adjusted for each individual cell modelled to fit its specific current. The Ca^{2+} is removed from the cytosol across the plasma membrane by a population of Ca^{2+} pumps. A Michaelis-Menton-based definition increases their action as cytosolic Ca^{2+} levels are increased. These pumps are balanced at resting levels by a leak current. In all cases the default flux flows across the membrane from extracellular to intracellular. In order to remove Ca^{2+} from the cell via a pump the equation describing the flux has to be defined as negative.

6.4.1 Calcium Influx

The inward currents produced by depolarising the plasma membrane were measured through the patch pipette using the computer program pClamp. Once leak corrected, integration of these currents allowed me to calculate the charge transferred across the plasma membrane. This in turn allowed me to calculate the concentration of Ca^{2+} that enters the cell during the 50 msec depolarisation.

This influx of Ca^{2+} was modelled by two exponentials (equation 6.1); one for channel activation while the second represents deactivation.

$$I_{ca} = CaC\_Plasmalemma * A * (1 - e^{-t*k\_on}) * e^{-t*k\_off}$$

Equation 6.1

Where $CaC\_Plasmalemma$ represents the concentration of channels in the plasma membrane, A is a constant representing the current amplitude through the channel and k_on and k_off are rate constants defining the rate of exponential rise and fall.

Using Boolean logic, this influx can be specified to a particular time period. In order to match the experimental data, the modelled influx occurs between $t > 1.052$ seconds and $t <= 1.102$ seconds.

A tail current occurs after the membrane voltage is returned to -70 mV due to the slow inactivation of the Ca^{2+} channels. This is modelled as a decaying exponential added onto the existing influx, producing a full equation defining the Ca^{2+} influx, including Boolean constraints of:

$$I_{ca} = CaC\_Plasmalemma * A * (1 - e^{-(t-1.052)*k\_on}) * e^{-(t-1.052)*k\_off} * (t > 1.052) * (t <= 1.102)$$
$$+ (A\_tail * CaC\_Plasmalemma * e^{-(t-1.103)*k\_off\_tail}) * (t >= 1.103) * (t < 1.2)$$

Equation 6.2

By adjusting A, and the various on and off rate constants, this can be made to fit the experimentally derived plot. An example of this is shown in figure 6.2 while the parameters used are found in Appendix B.

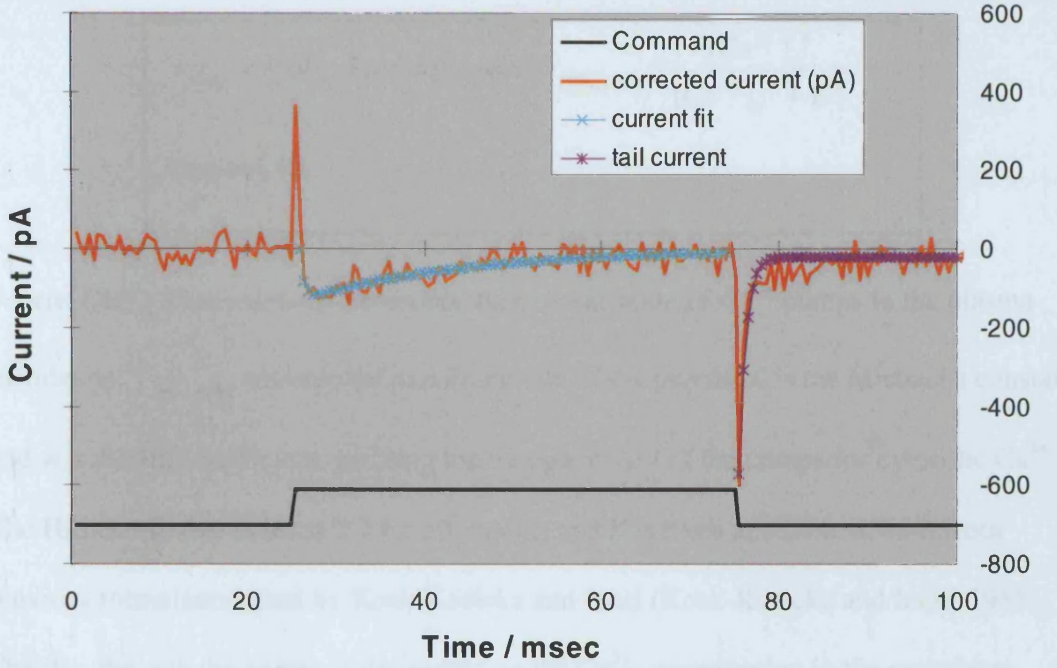

Figure 6.2 Experimental and modelled influxes

The inward Ca^{2+} currents following depolarisation of the plasma membrane were measured through pClamp. These can then be leak corrected and fitted using a combination of exponential equations. The initial Ca^{2+} influx is fitted by a double exponential representing channel activation and subsequent deactivation following repolarisation to -70 mV. A tail current caused by the slow inactivation of the Ca^{2+} channels is fitted using a single decaying exponential. This fit was performed for the current traces from each exemplar cell. The plot displayed shows the influx for 120504 which was fitted with the parameters A = -13, CaC_plasmalemma = 10, k_{on} = 2000, k_{off} = 55, A_{tail} = -55, k_{off_tail} = 1300.

6.4.2 Calcium Extrusion

The Ca^{2+}-ATPases used to pump Ca^{2+} out of the cell back across the plasma membrane have previously been shown to fit well to a Michaelis-Menton equation (Zador *et al.*, 1990). Used to describe the rate of enzyme-catalysed reactions, an adapted form of this equation (equation 6.3) can be used to describe the flow of Ca^{2+} out of the cell via the membrane pumps.

$$I_{pump} = CaP\_Plasmalemma * V_{max\_pump} * \frac{[Ca^{2+}]_c^{\,n}}{[Ca^{2+}]_c^{\,n} + K^n}$$

Equation 6.3

Where $CaP\_Plasmalemma$ represents the concentration of Ca^{2+} pumps in the plasma membrane, V_{max_pump} controls the maximum rate of the pumps, K is the Michaelis constant and n is the Hill coefficient, defining the co-operativity of the pumps for cytosolic Ca^{2+}. The Hill coefficient is set as 2.7 for all models and K is fixed at 0.06 μM, both from previous formulation used by Kosk-Kosicka and Inesi (Kosk-Kosicka and Inesi, 1985). The flux through the pumps is dependent on the Ca^{2+} concentration in the cytoplasm, allowing it to significantly increase the rate of Ca^{2+} removal following increases in $[Ca^{2+}]_c$. This characteristic also means the pumps have a non-zero flux at resting $[Ca^{2+}]_c$. It is for this reason that an inward leak current needs to be included to ensure the intracellular Ca^{2+} levels remain constant while the cell is at rest.

This is defined using a similar, Michaelis-Menton-based equation as used for the Ca^{2+} pumps for simplicity in balancing the two fluxes.

$$I_{leak} = CaP\_Plasmalemma * V_{max\_pump} * \frac{[Ca^{2+}]_{rest}{}^{n}}{[Ca^{2+}]_{rest}{}^{n} + K^{n}}$$

Equation 6.4

Where $[Ca^{2+}]_{rest}$ is the resting concentration of Ca^{2+} in the cytosol, previously measured as 129 nM. K and n have the same definitions and values as for the Ca^{2+} pumps.

The rate of outpumping in the modelled cells is controlled by the parameter V_{max_pump}. This is adjusted to fit the experimental data for each exemplar cell. The values used are found in Appendix B.

6.5 The Nuclear Envelope

As discussed in section 1.7, the nuclear envelope, whilst permeable to Ca^{2+}, provides a barrier to diffusion, slowing the movement of Ca^{2+} changes into the nucleus. This has been modelled by providing pathways through the nuclear envelope for each species. These provide a flow into the nucleus as dictated by their respective concentration gradient over the nuclear envelope allowing a delay in diffusion to be included (figure 6.3). Although I could have set a permeability constant, specific to each species, the nuclear pores represent holes that are large on the molecular scale and are therefore likely to be non-selective. Given this, the permeability of the nuclear envelope (P) to a particular species is set as a simple fraction of the thickness of the nuclear envelope (x), the density of nuclear pore complexes (NPCs) (a) and the diffusion constants of the individual species (D).

$$P = \frac{aD}{x}$$

Equation 6.5

With a and x constant, the permeability is proportional to the diffusion constant. The permeability constant for diffusion of the Ca^{2+}-bound indicator dye into the nucleus was adjusted in order to create a delay in crossing nuclear envelope of roughly 10 msec as measured in the experimental data. This was achieved with a permeability of the nuclear envelope to the indicator dye of 18 $\mu m\ s^{-1}$. The thickness of the nuclear envelope has previously been measured as 15 nm (al-Mohanna *et al.*, 1994). Using this and the

diffusion constant of the indicator dye, which I have previously measured as 36 $\mu m^2 s^{-1}$, it is possible to calculate from equation 6.5 that the nuclear pore complexes make up 0.75 % of the nuclear envelope. If the diameter of a NPC is taken as 61 nm (al-Mohanna *et al.*, 1994), measured in rat sensory neurones, this corresponds to a NPC density of 26 μm^{-2}. Although there are no published values for NPC density in sensory neurones, this is the same order of magnitude as values measured in HeLa cells of 24 μm^{-2} (Walther *et al.*, 2003) and *Xenopus laevis* oocyte of 48 μm^{-2} (Andrade *et al.*, 2001). With the permeability for the indicator dye set, and the ratio of a/x calculated as 0.5 μm^{-1}, the permeabilities for the other species could in turn be calculated using equation 6.5.

The implication of this is that the entire diameter of the nuclear pore is available for diffusion of ions. This contrasts with the results published by al-Mohanna *et al.* in neuroblastoma cells where ion diffusion was found to be limited to smaller pores surrounding the central granule (al-Mohanna *et al.*, 1994).

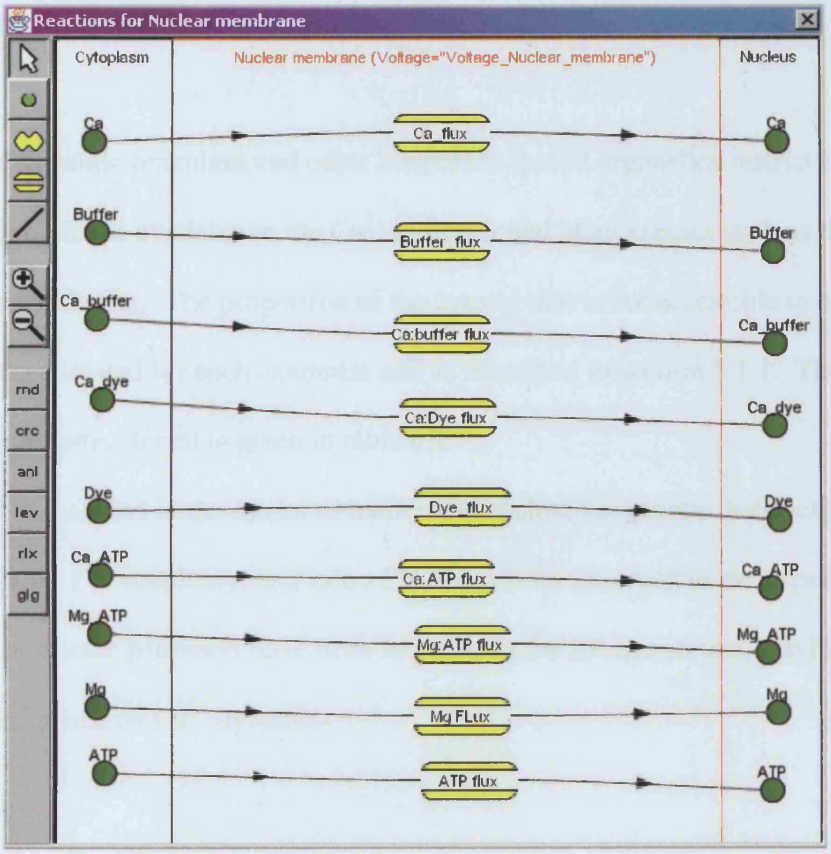

Figure 6.3 Pathways into the nucleus

Diffusion into the nucleus is modelled for each species using a series of pathways. This allows a flow across the nuclear envelope governed by their respective concentration gradients. The permeability of the nucleus to the various species is proportional to their diffusion constants and modulated by the ratio of the density of nuclear pores with the thickness of the nuclear envelope. This permeability has been adjusted such that the nuclear envelope causes a delay in diffusion of roughly 10 msec for the Ca^{2+}-bound indicator species with a diffusion constant of 36 $\mu m^2 s^{-1}$, as measured from the experimental data.

6.6 Endoplasmic Reticulum

The endoplasmic reticulum and other membrane-bound organelles restrict the amount of the cytosol that is available to the Ca^{2+} indicator and other species such as the endogenous buffer. The proportion of the cytosol that is not accessible to cytosolic dye has been estimated for each exemplar cell as described in section 5.1.1. The precise proportion for each cell is given in table 6.1.

The ER is included in the model as membrane enclosed organelle distributed throughout the cytosol. For simplicity, and as no CICR has been observed in the experiments, no uptake or release pathways have been included in the ER membrane, leaving it with no active influence on Ca^{2+} dynamics.

6.7 Geometry

In order to produce spatial models, the relevant reaction-diffusion interactions have to be contained within a defined geometry. This provides the boundary conditions for the models. The geometries within which my models are run are produced from the imaged structure of each exemplar cell.

A z-stack image is produced by imaging a series of confocal slices whilst moving through pre-set increments in the z-direction. This allows the three-dimensional geometry of each individual cell to be measured. Due to the standard topography of a replated DRG neurone, resulting in no axonal growth, these geometries can be very accurately

reproduced in algebraic form within The Virtual Cell. These modelled geometries are created in three distinct parts; the nucleus and the surrounding cytosol, defined by their respective membranes, both contained within the extracellular domain. An example geometry from cell 140105 is shown in figure 6.4. This figure also shows the physiological areas mapped onto the relevant geometric domains.

The respective equations for each exemplar cell can be found in appendix B.

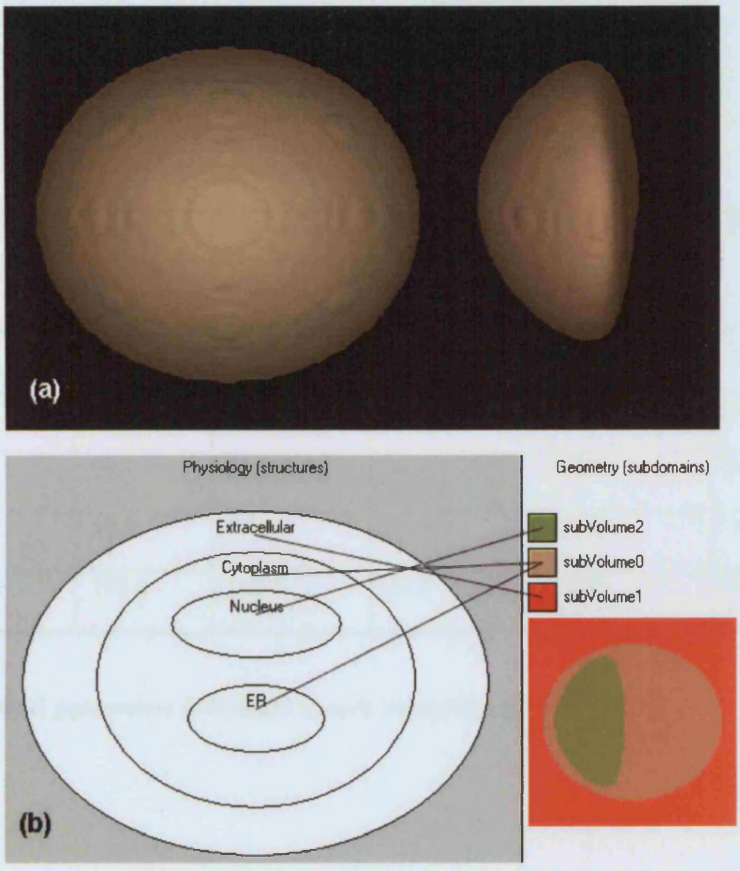

Figure 6.4 Geometry definition in The Virtual Cell

Panel a shows an example of a model geometry (cell 140105). This is created algebraically in three components; the cytosolic (left hand side) and nuclear (right hand side) domains and the surrounding extracellular space. Panel b shows the process of mapping the various physiological structures to the relevant geometric domains. The structure relating to the ER is shown distributed throughout the cytoplasm by means of mapping both structures to the same geometric domain.

6.8 Model Parameters for Each Exemplar Cell

The parameters used to model simple Ca^{2+} diffusion with a calbindin-based buffering system are shown below in tables 6.1 and 6.2. Table 6.1 lays out the parameters values that are specific to individual cells, while table 6.2 shows the universal parameters whose values remain unchanged between individual cells in the standard model.

	Initial Concentrations (μM)				
Cell Modelled	Free CaB	Ca^{2+}-bound CaB	Free OG488BD	Ca^{2+}-bound OG488BD	ER concentration (% of cytosol)
120504	9.9	8.1	53.6	3.8	37
240604	41.2	33.6	54.2	3.8	34
221204	62.7	51.1	34.9	2.9	46
140105	10.3	8.4	37.5	3.1	44
190105	198.8	162.1	34.2	2.8	67

Table 6.1 Model parameters individual to each exemplar cell

Species	Initial Concentration (μM)	Diffusion Constant ($\mu M^2 s^{-1}$)
Free calcium	0.129	233
Free calbindin	See table 6.1	20
Ca^{2+}-bound calbindin	See table 6.1	20
Free OG488BD	See table 6.1	36
Ca^{2+}-bound OG488BD	See table 6.1	36
Free ATP	364	140
Free Mg	1000	233
Ca^{2+}-bound ATP	0.235	140
Mg^{2+}-bound ATP	3636	140

Table 6.2 Universal model parameters

6.9 Model Output

The output from the models looks at the changes in concentration of the Ca^{2+}-bound indicator species while the images from the experimental data look at fluorescence changes of the indicator dye. This fluorescence is made up of the fluorescence signals from both the free indicator and the Ca^{2+}-bound form. These two fluorescent signals are related by the dynamic range of the indicator. The concentrations of these two species are converted into the fluorescence intensity by adding the concentration of free indicator dye to the concentration of Ca^{2+}-bound dye multiplied by its dynamic range (DR) as shown in equation 6.6.

$$I_{total} = [dye] + DR * [Ca : dye]$$

Equation 6.6

The resulting fluorescent output from one of these models is shown in figure 6.5. This shows normalised linescan results from both the experimental and modelled data of cell 190105 over the full 11 seconds of experimentation and zoomed on the 576 msec around the time of depolarisation. I have chosen this cell as an example as it has the highest ratio of inward current to OG488BD signal making it the most sensitive to manipulation. Both the experimental and modelled results are displayed using the same colour mapping.

To provide a quantitative analysis of the model against the experimental data, I have analysed the modelled results using the same technique as used in section 3.2 to analyse the patch clamp results; looking at the intensity changes at three points inside the cell, at the centre and 3 μm in from the plasma membrane on each side. This allows the modelled data to be directly compared to the experimental data.

Figure 6.6 shows the normalised model output from these three points for this exemplar cell compared against the equivalent points from the relevant experimental data.

From both figure 6.5 and figure 6.6, it can be seen that in general the model provides a good fit to the experimental data, closely representing the influx of Ca^{2+} across the plasma membrane, its subsequent buffering by intracellular endogenous buffers and diffusion to the centre of the cell and the nucleus. The only mechanism in the model for returning $[Ca^{2+}]_i$ to resting levels is extrusion across the plasma membrane via plasma membrane Ca^{2+}-ATPases. Comparing the recovery time courses for the experimental and modelled data shows that this provides a good fit, consistent with the findings that in chick DRG neurones extrusion across the plasma membrane provides the main

mechanism for returning $[Ca^{2+}]_i$ to resting levels following a 50 msec depolarisation (Wanaverbecq *et al.*, 2001).

However, two main differences stand out between the experimentally derived data and the modelled data. The first is the appearance of Ca^{2+} 'hotspots' located under the plasma membrane in the model output which do not occur in the experimental data. Secondly, the model predicts a significantly slower diffusion to the centre of the cell than seen in the experimental data. This delay becomes more pronounced in models with higher concentrations of endogenous buffer.

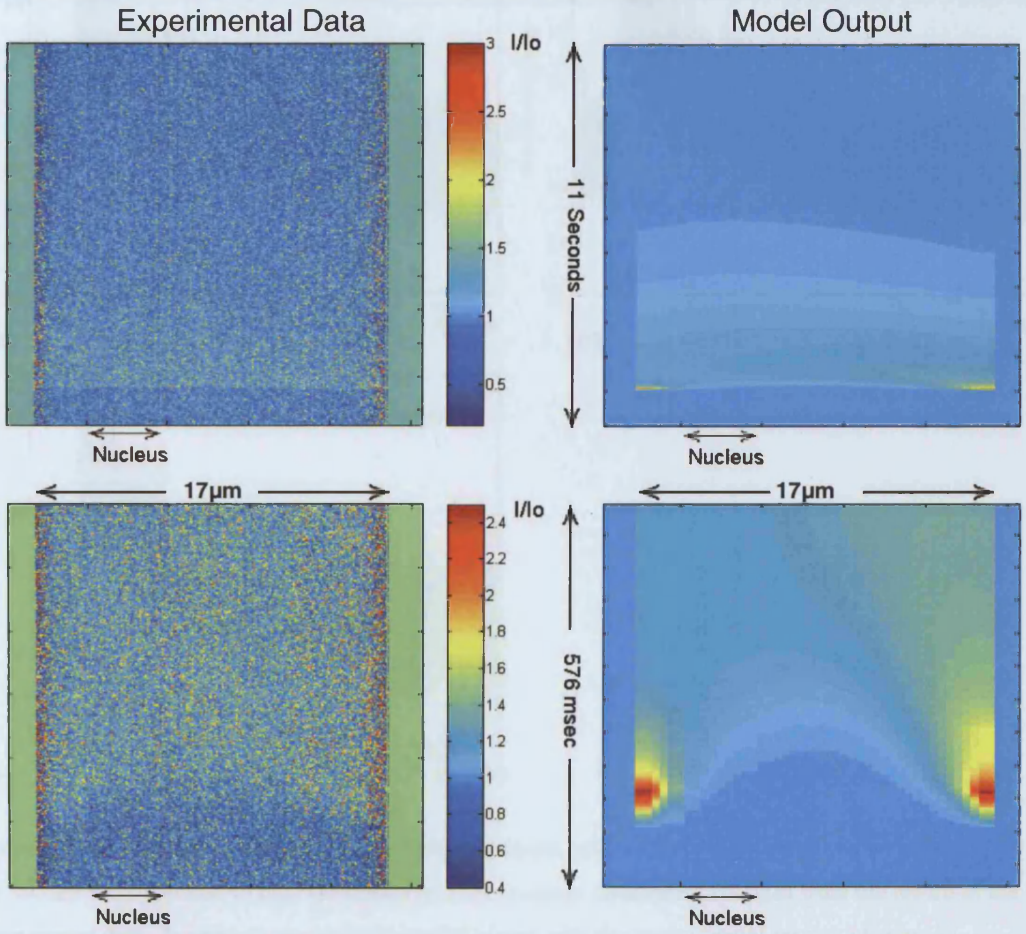

Figure 6.5 Model output

The normalised model outputs for cell 190105 are displayed against the corresponding normalised linescan data over the full 11 seconds of experiment and the 576 msec around the 50 msec depolarisation. Both experimental and modelled results are displayed on identical colour-maps. The model output zoomed around the time of depolarisation clearly show the appearance of Ca^{2+} hotspots under the plasma membrane that are not present in the experimental data.

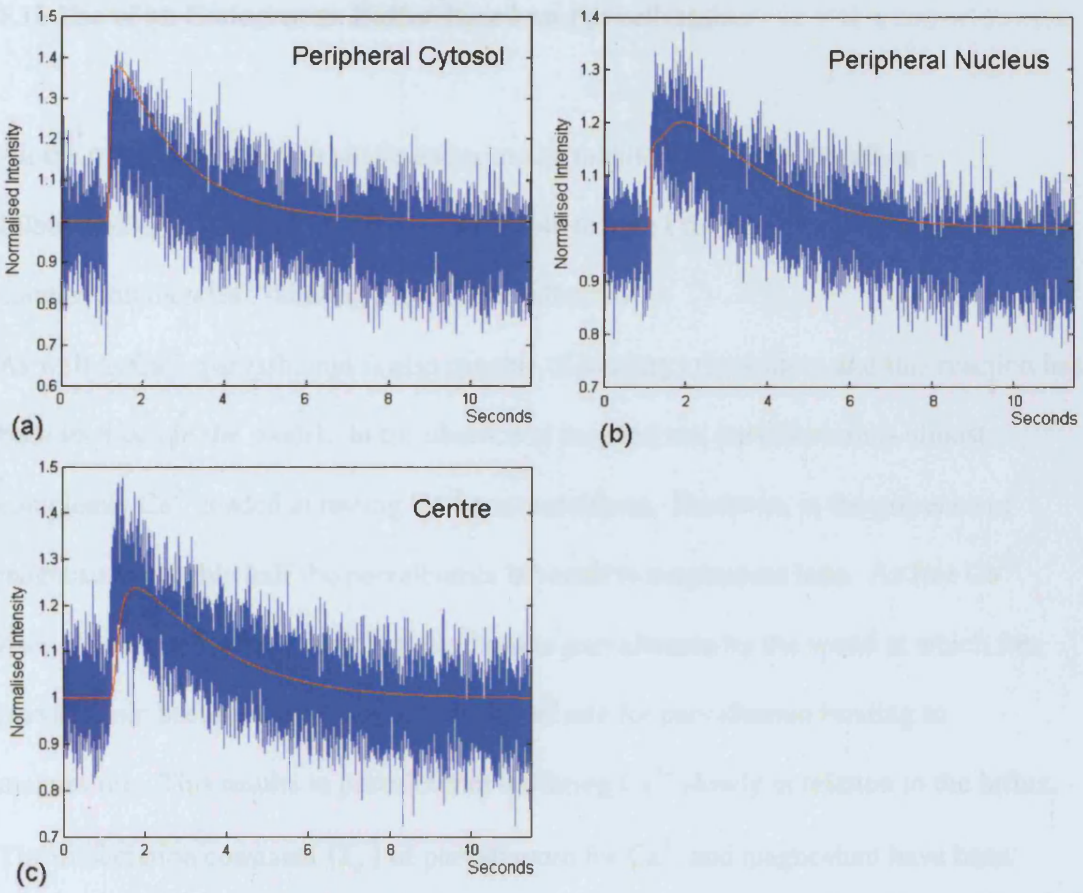

Figure 6.6 Fluorescent intensity changes throughout the cell

The models were adjusted to provide a good fit to the average fluorescent changes from the centre of the experimental data. In order to compare the model output with the experimental results, changes in fluorescent intensity were measured at the centre of the cell and 3 μm in from each side of both data. Results shown here from cell 190105 show a good fit of the model output, the red trace, to the experimental data, the blue trace, in both amplitude and decay of the Ca^{2+} signal following a 50 msec depolarisation. Fits were performed by eye, matching the experimental data at the peak of the average signal, the time taken for the Ca^{2+} signal to diffuse to the centre of the cell and the decay in the Ca^{2+} signal due to efflux from the cell via plasma membrane pumps. However, from panel c, showing the normalised fluorescent changes at the centre of the cell, it is clear that the model predicts a significantly slower diffusion of the Ca^{2+} signal to the centre of the cell than is seen in the experimental data. Photobleaching, causing the final signal to drop below baseline values, was considered to be a significantly weaker effect on the decaying signal than the cellular Ca^{2+} regulation mechanisms and hence was not included in the modelling process.

6.10 Use of an Endogenous Buffer Based on Parvalbumin

All the models have used a single endogenous, mobile Ca^{2+}-buffer based on calbindin-D_{28k}. To see if this was a reasonable model, I replaced the calbindin-D_{28k} with another common Ca^{2+}-binding protein, parvalbumin.

As well as Ca^{2+}, parvalbumin is also capable of binding magnesium, and this reaction has been included in the model. In the absence of magnesium, parvalbumin is almost completely Ca^{2+} loaded at resting Ca^{2+} concentrations. However, in the presence of magnesium roughly half the parvalbumin is bound to magnesium ions. As free Ca^{2+} rises, it is limited in how rapidly it can bind to parvalbumin by the speed at which free parvalbumin becomes available; that is the off rate for parvalbumin binding to magnesium. This results in parvalbumin buffering Ca^{2+} slowly in relation to the influx. The dissociation constants (k_d) of parvalbumin for Ca^{2+} and magnesium have been published as 3.77 nM and 24.5 μM respectively (Eberhard and Erne, 1994). Using these values with the published dissociation rates for Ca^{2+} and magnesium from parvalbumin of 1.03 and 3.42 s^{-1} respectively (Hou *et al.*, 1992), it is possible to calculate the association rates of $k_{on} = 273.21\,\mu M^{-1}\,s^{-1}$ for Ca^{2+} and $k_{on} = 0.14\,\mu M^{-1}\,s^{-1}$ for magnesium. For simplicity, I initially tried a model in which parvalbumin is present at the same total concentration that I used for calbindin-D_{28k} distributed with a calculated ratio of 1 to 40.81633 to 34.21751 for free parvalbumin, parvalbumin bound to Ca^{2+} and parvalbumin bound to magnesium respectively. A diffusion constant of 43 $\mu m^2\,s^{-1}$ has been taken from work by Schmidt *et al.* (Schmidt *et al.*, 2003).

Figure 6.7 shows a result from an example model using parvalbumin as the endogenous, mobile buffer. This produces a clear biphasic recovery from the Ca^{2+} influx which does not fit the experimental data. The biphasic result was seen in all five exemplar models. As a result of this, I have concluded that the major endogenous Ca^{2+} buffer in my exemplar cells cannot be parvalbumin. The use of calbindin-D_{28k} as the endogenous buffer in my model remains a reasonable assumption, providing a good fit to the experimental data.

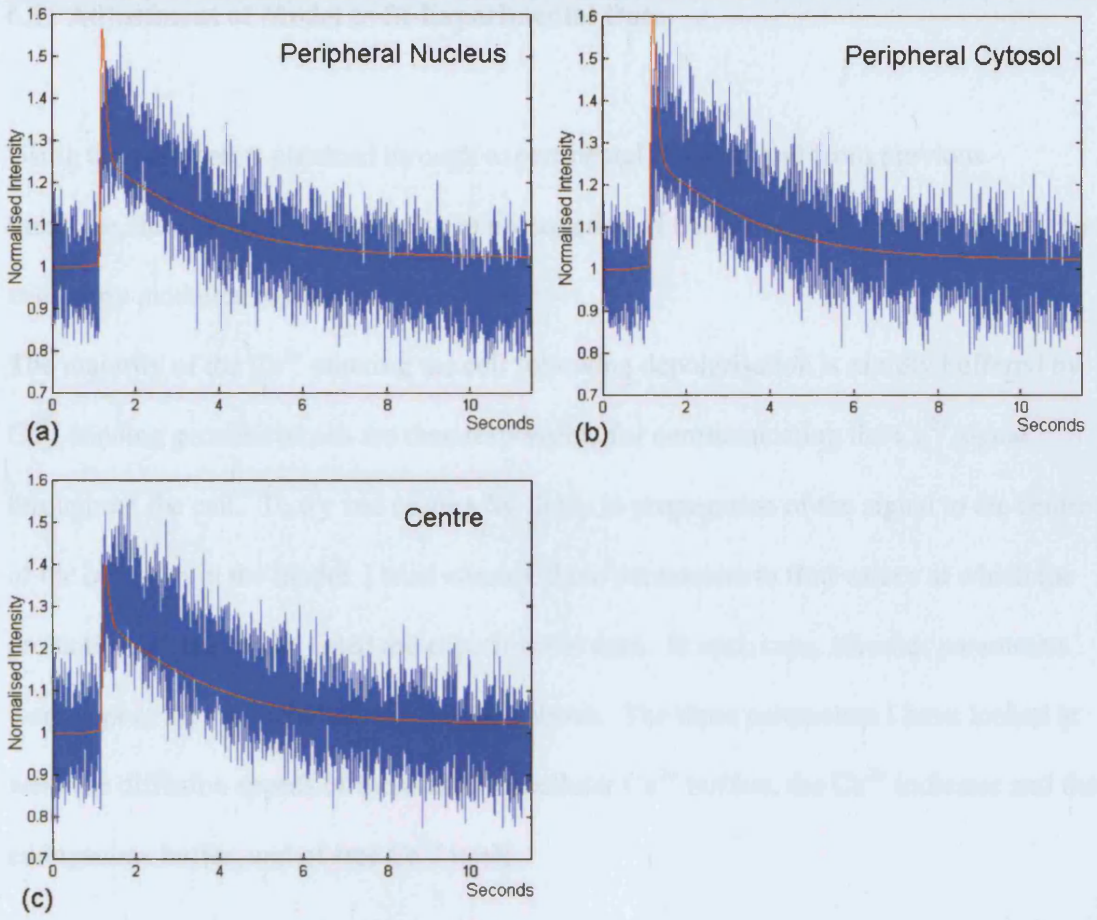

Figure 6.7 Parvalbumin as the endogenous Ca^{2+} buffer

In order to see if the use of calbindin-D_{28k} as the basis for the endogenous buffer in my models was a reasonable assumption, the total calbindin-D_{28k} was replaced with an equal concentration of the Ca^{2+} buffer parvalbumin. Results shown here from cell 240604 clearly show the resulting bi-phasic decay produced by this change at the three standard points within the cell; the centre and 3 μm in from the plasma membrane on each side of the cell. This does not fit the experimental results indicting that the endogenous buffer in my exemplar cells cannot be parvalbumin. These plots show the normalised model output, in red, superimposed upon the normalised experimental data, in blue.

6.11 Adjustment of Model to fit Experimental Data

Using the parameters obtained through experimental methods and from previous literature, there is a significant delay in propagation of the Ca^{2+} signal to the centre of the cell in my modelled results.

The majority of the Ca^{2+} entering the cell following depolarisation is rapidly buffered by Ca^{2+}-binding proteins which are then responsible for communicating the Ca^{2+} signal throughout the cell. To try and correct for delay in propagation of the signal to the centre of the cell seen in the model, I tried altering three parameters to find values at which the predictions of the model fitted the experimental data. In each case, all other parameters were kept at the standard values described above. The three parameters I have looked at were the diffusion speeds of the main intracellular Ca^{2+} buffers, the Ca^{2+} indicator and the endogenous buffer, and of free Ca^{2+} itself.

6.11.1 Increasing the Diffusion Constant of the Calcium Indicator Dye

In order to achieve a reasonable fit in diffusion to the centre of the cell by adjusting the diffusion speed of the indicator dye, its diffusion constant had to be increased by a minimum of a factor of ten from 36 $\mu m^2 s^{-1}$ to 360 $\mu m^2 s^{-1}$ (figure 6.8). The original value comes from my measurements using fluorescein dextran experiments, as described in section 5.4. While it is reasonable that there will be some error associated with this

value, it seems very unlikely that this would be enough to account for this large increase in diffusion speed.

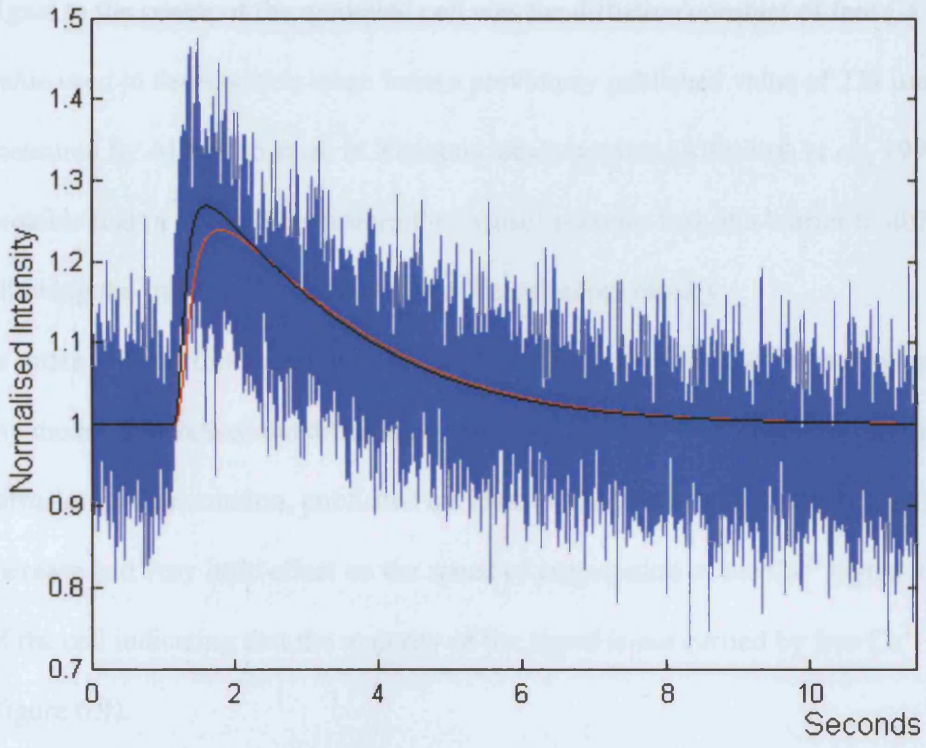

Figure 6.8 Increasing the diffusion constant of the Ca^{2+} indicator dye

In an attempt to increase the speed of diffusion of the Ca^{2+} signal to the centre of the modelled cell I increased the diffusion constant of the Ca^{2+} indicator dye OG488BD. Results shown here from cell 190105 display the normalised fluorescent intensity changes at the centre of the cell from the experimental data, the blue trace, and the model output, the red and black traces. The diffusion constant of the indicator dye had to be increased by a minimum of ten-fold from 36 $\mu m^2 s^{-1}$ (red trace) to 360 $\mu m^2 s^{-1}$ (black trace) in order achieve a reasonable fit for diffusion to the centre of the cell.

6.11.2 Using the Diffusion Constant of Calcium in Free Solution

Another possibility that I looked at in my attempts to speed up the diffusion of the Ca^{2+} signal to the centre of the modelled cell was the diffusion constant of free Ca^{2+}. The value used in the model is taken from a previously published value of 233 $\mu m^2 s^{-1}$ measured by Allbritton *et al.* in Xenopus laevis oocytes (Allbritton *et al.*, 1992). It is possible that in my DRG neurones the cytosol presents less of a barrier to diffusion, allowing the free Ca^{2+} to diffuse across the cell more rapidly.

In order to see if this accounted for the slow diffusion of the Ca^{2+} signal to the centre of my model, I increased the diffusion constant of free Ca^{2+} to its upper limit; that of Ca^{2+} diffusion in free solution, published by Lide as 792 $\mu m^2 s^{-1}$ (Lide, 1993-1994). This increase had very little effect on the speed of propagation of the Ca^{2+} signal to the centre of the cell indicating that the majority of the signal is not carried by free Ca^{2+} ions (figure 6.9).

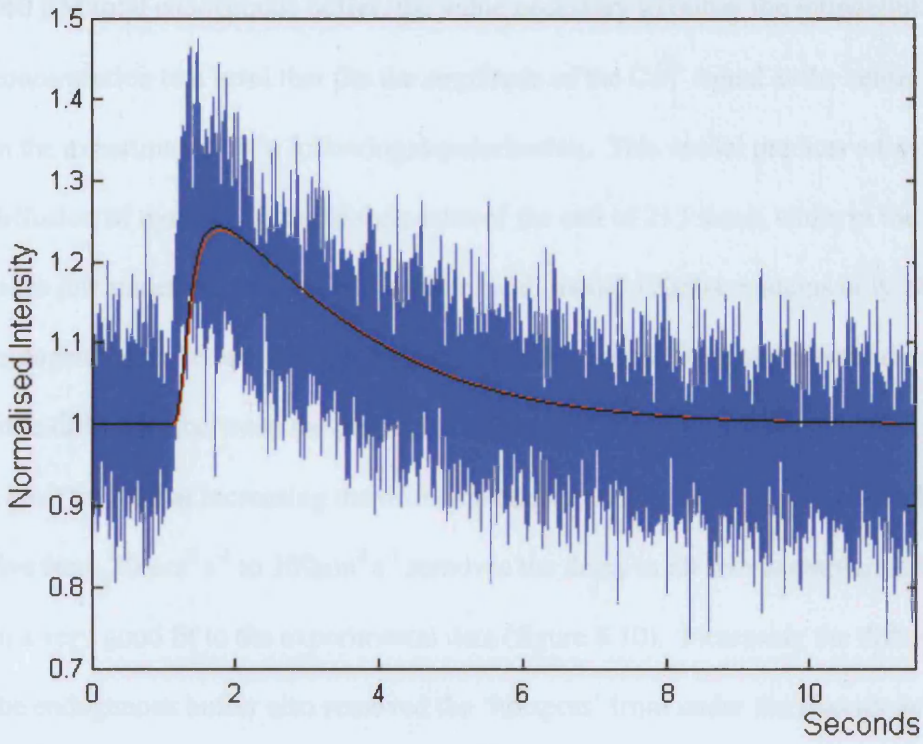

Figure 6.9 Increasing the diffusion constant of free Ca^{2+}

In an attempt to increase the speed of diffusion of the Ca^{2+} signal to the centre of the modelled cell I increased the diffusion constant of free Ca^{2+}. Results shown here from cell 190105 display the normalised fluorescent intensity changes at the centre of the cell from the experimental data, the blue trace, and the model output, the red and black traces. Even increasing the diffusion constant of free Ca^{2+} from the published value in cytoplasm of 233 $\mu m^2 s^{-1}$ (red trace) to the value measured in free solution of 792 $\mu m^2 s^{-1}$ (black trace) did not significantly increase the speed of diffusion to the centre of the cell.

6.11.3 Increasing the Diffusion Constant of the Endogenous Buffer

The mismatch in the timecourse of the diffusion of the Ca^{2+} signal to the centre predicted by the model and the actual results from the cell is more pronounced in models with higher concentrations of endogenous buffer. The model for cell 190105 had over

360 μM total endogenous buffer, the value necessary to buffer the intracellular Ca^{2+} concentration to a level that fits the amplitude of the Ca^{2+} signal at the centre of the cell in the experimental data following depolarisation. This model predicts a time for diffusion of the Ca^{2+} signal to the centre of the cell of 213 msec, while in the real data it takes just under 70 msec . On the other hand, model 120504 contains only 18 μM total endogenous buffer and provides a very close fit to its relative experimental data with very little difference between the propagation times.

I have found that increasing the diffusion constant of the endogenous buffer by a factor of five from 20 $\mu m^2 s^{-1}$ to 100$\mu m^2 s^{-1}$ removes the delay in all five exemplar cells resulting in a very good fit to the experimental data (figure 6.10). Increasing the diffusion speed of the endogenous buffer also removed the 'hotspots' from under the plasma membrane to an acceptable level given the noise from the experimental data. Figure 6.11 shows the resulting linescan images with endogenous buffer diffusion constants of both 20 $\mu m^2 s^{-1}$ and 100 $\mu m^2 s^{-1}$ alongside the relevant experimental data, clearly showing the removal of the 'hotspots'. This value of 100 $\mu m^2 s^{-1}$ is very close to a value of the diffusion constant of calbindin-D_{28k} I have calculated in water of 107 $\mu m^2 s^{-1}$ using the Stokes-Einstein equation (equation 6.7).

$$D = \frac{k_B T}{6\pi\eta R}$$

Equation 6.7

This defines the diffusion constant of a molecule in terms of its radius (R), the viscosity of the solution (η), the temperature (T) and Boltzmann's constant (k_B). Assuming a

molecule of calbindin-D_{28k} has a density similar to water, of 1.33 g cm^{-1}, its molecular weight of 28 kDa would result in a molecular radius of 2.03 nm. At 20.2 °C, water has a viscosity of 0.01 g cm^{-1} s. Using these values, it is possible to calculate a diffusion constant for calbindin-D_{28k} in water of 107 μm^2 s^{-1}.

While it would seem unlikely that the intracellular diffusion constant of calbindin-D_{28k} would be that of the free medium, this result suggests that fast moving, and presumably less massive, endogenous Ca^{2+} buffers are present in chick DRG neurones rapidly relaying the Ca^{2+} from the plasma membrane into the centre of the cell and to the nucleus.

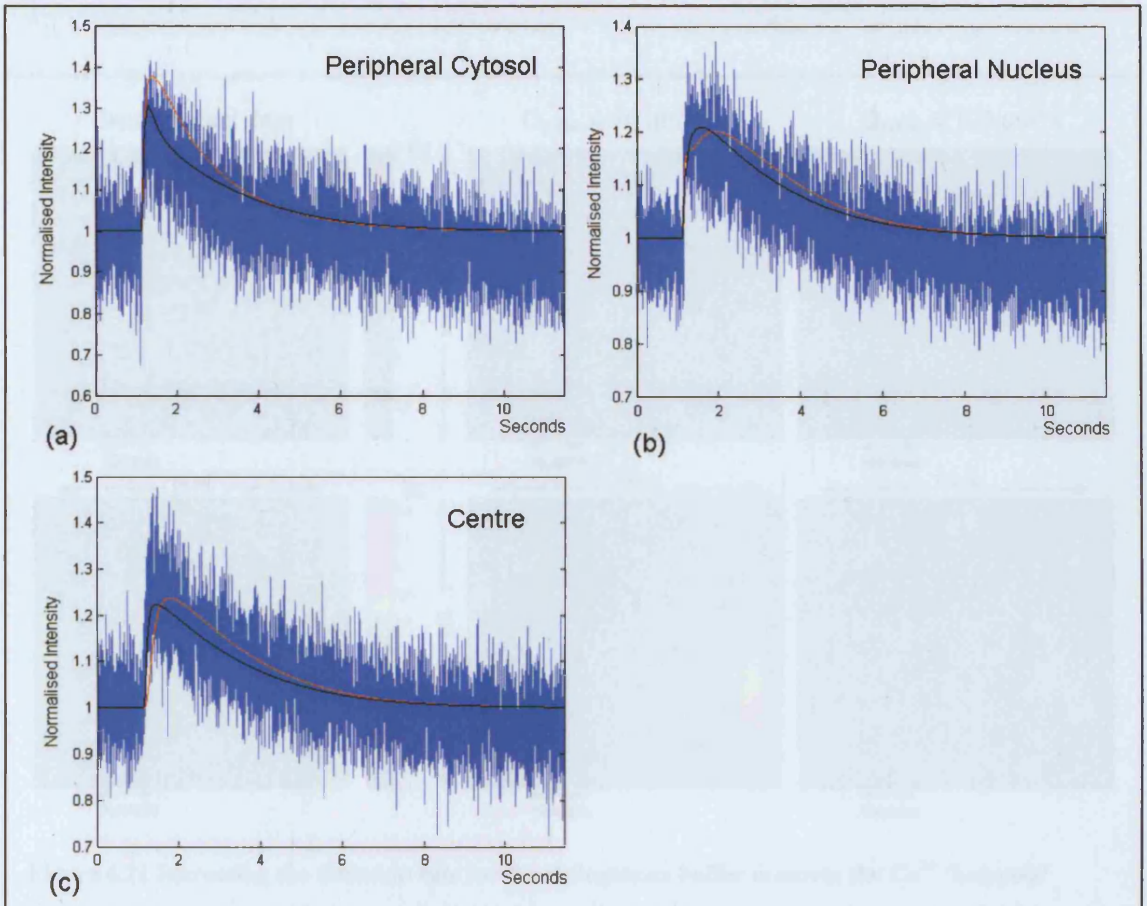

Figure 6.10 Increasing the diffusion constant of the endogenous buffer speeds up diffusion to the centre of the cell

In an attempt to increase the speed of diffusion of the Ca^{2+} signal to the centre of the modelled cell I increased the diffusion constant of the endogenous buffer. Results shown here from cell 190105 display the normalised fluorescent intensity changes at the centre of the cell and 3 μm in from the plasma membrane on each side from the experimental data, the blue trace, and the model output, the red and black traces. As shown in panel c, I found that increasing the diffusion constant of endogenous buffer from the published value for calbindin-D_{28k} in cytoplasm of 20 $\mu m^2 s^{-1}$ (red trace) five-fold to 100 $\mu m^2 s^{-1}$ (black trace) was sufficient to achieve a good fit in the diffusion of the Ca^{2+} signal to the centre of the cell in all my exemplar cells.

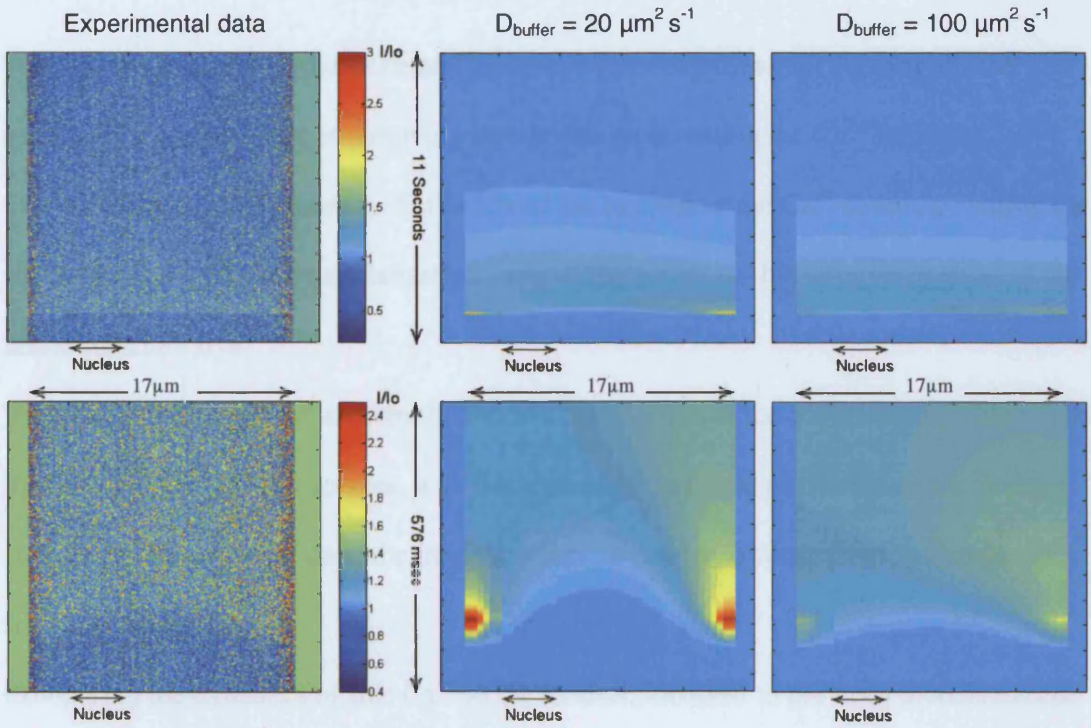

Figure 6.11 Increasing the diffusion rate for the endogenous buffer removes the Ca^{2+} 'hotspots'
In order to achieve a good fit for the diffusion of the Ca^{2+} signal to the centre of the cell, the diffusion constant for the endogenous buffer was increased five-fold to 100 µm^2 s^{-1}. This was also found to remove the Ca^{2+} hotspots from the model output to a level that was acceptable under the noise of the experimental data. The normalised model output from cell 190105 with the standard and increased buffer diffusion constants is shown here along side the relevant normalised experimental data, for the full 11 seconds of experiment and the 576 msec around the 50 msec depolarisation. Corresponding images are shown on identical colour-maps.

6.12 Effects of a Calcium Indicator on Intracellular Calcium Dynamics

With the revised model now accurately portraying the experimental data for all five exemplar cells, the effect of removing the species representing the Ca^{2+} indicator OG488BD could be examined. This allowed me to observe the Ca^{2+} dynamics within the cell following a 50 msec depolarisation without the additional buffering properties of the added indicator dye.

Whereas all previous results from the models have looked at the concentration changes of the Ca^{2+}-bound indicator species, which is then converted into the fluorescence changes seen in the experimental data, the model outputs now refer to concentration changes of free Ca^{2+} within the cell.

Comparing the dynamics of free Ca^{2+} in the models, identical to previous models except for the removal of the Ca^{2+} indicator species, the pattern of diffusion remains largely unchanged (figure 6.12). In particular, by looking at the changes in concentration of free Ca^{2+} at the standard three points within the cell following a 50 msec depolarisation, the time course of the changes in Ca^{2+} concentrations were very similar except that the amplitude was greater in the absence of the dye. However, looking at high temporal resolution I found that the Ca^{2+} signals were very slightly delayed in the presence of the indicator dye. Specifically, looking 3 μm in from the edges of the modelled cell the output from the model including the indicator dye reaches half-maximum 2 msec after that measured in the absence of the indicator dye. The Ca^{2+} signals were found to diffuse to the centre of the cell with an identical propagation rate, the Ca^{2+} signal measured from

the model including the indicator dye at the centre of the cell reaching half-maximum 1 msec after those measured in the absence of the dye (figure 6.13).

This is a highly significant result as it shows that although the experimental technique of adding a Ca^{2+} indicator dye into a cell does affect the intracellular Ca^{2+} dynamics, these affects are very small and within the errors of the model which samples every 1 msec. Furthermore, returning to the original question of whether the inclusion of the indicator dye is acting to speed up the diffusion of the Ca^{2+} signal to the centre of the cell, I have shown that this is not the case and more specifically that it is the endogenous buffers that play the dominant role in the propagation of the Ca^{2+} signal throughout the cell and that changes in their diffusion constants can significantly alter the dynamics of the signal.

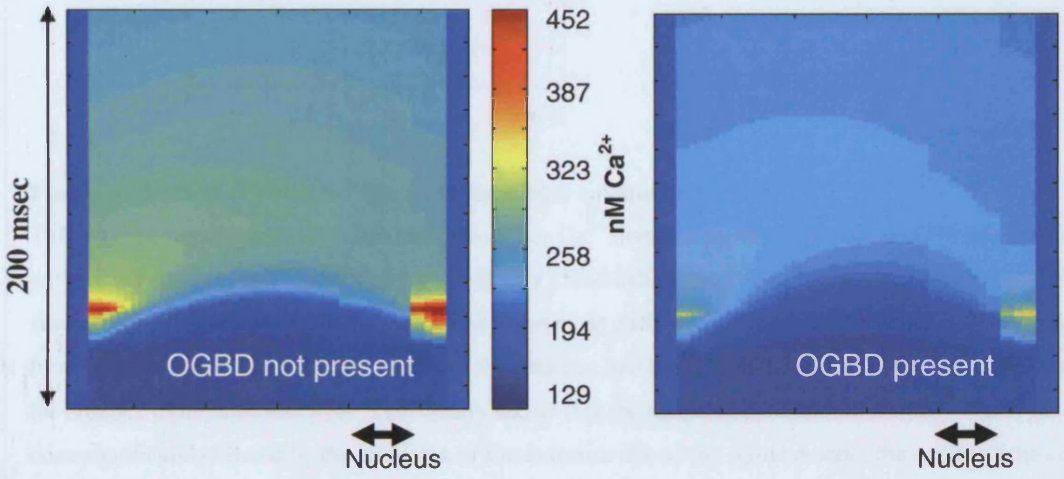

Figure 6.12 Effect of indicator dye on intracellular calcium dynamics

With models created for five exemplar cells, the indicator dye species was removed to see the effect this has on the intracellular Ca^{2+} dynamics. This figure shows the model output of the concentration changes of free Ca^{2+} following a 50 msec depolarisation with and without the species representing the Ca^{2+} indicator OG488BD from cell 240604. This cell has the highest ratio of concentration of indicator dye to endogenous buffer out of the five exemplar cells and so were the indicator dye to have a significant effect on the Ca^{2+} dynamics within the cell it would be expected to be most evident in this cell.

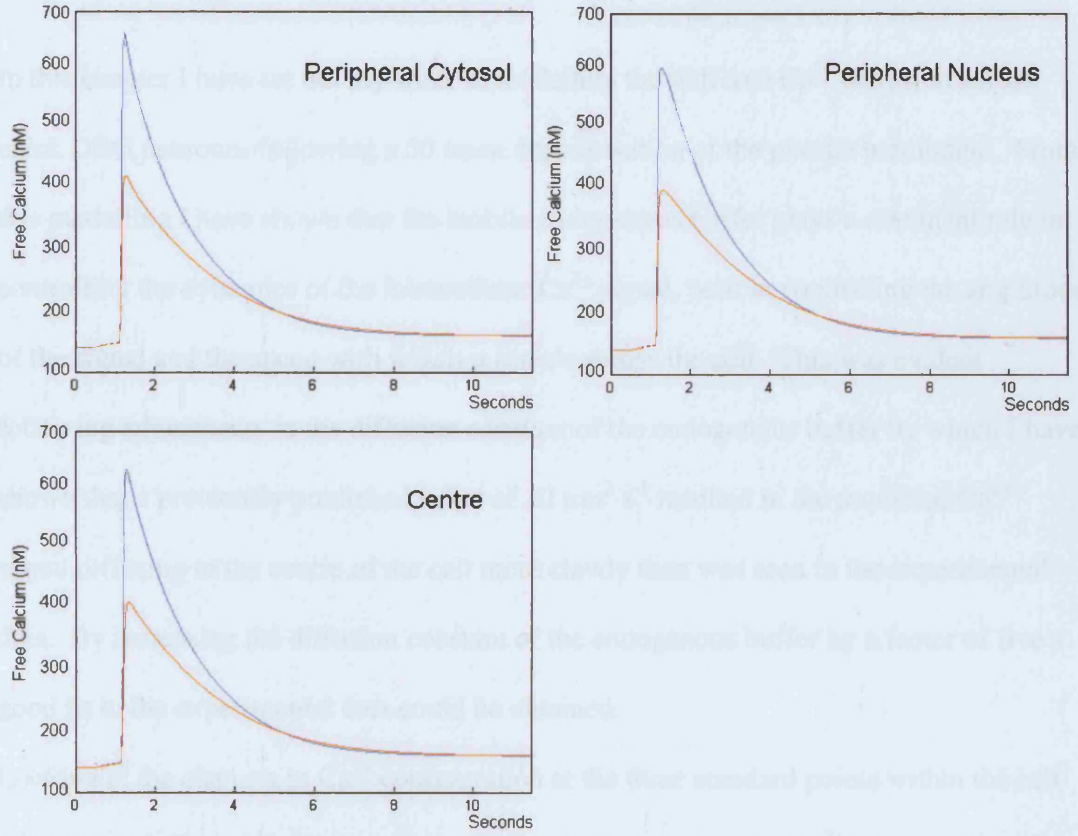

Figure 6.13 Effect of indicator dye on intracellular calcium dynamics

This figure shows the concentration changes of free Ca^{2+} from the model output of cell 240604, with and without the species representing the Ca^{2+} indicator OG488BD (blue and red plots respectively), at the 3 standard points within the cell; the centre and 3 μm in on each side. At each of the points the Ca^{2+} signal from the model including the Ca^{2+} indicator dye reaches half-maximum 2 msec after the signal measured in the absence of the indicator dye. This clearly shows that the temporal dynamics of the Ca^{2+} signal have not been significantly altered by the inclusion of the indicator dye as the signal reaches the centre of the cell at nearly identical times with and without the indicator dye present. The plots of Ca^{2+} changes at the edges of the cell also show that there are no adverse spatial or temporal effects of including the indicator dye.

6.13 Discussion on Modelling Buffered Calcium Diffusion

In this chapter I have set out my work in modelling the buffered Ca^{2+} diffusion across chick DRG neurones following a 50 msec depolarisation of the plasma membrane. From this modelling I have shown that the mobile endogenous buffer plays a dominant role in controlling the dynamics of the intracellular Ca^{2+} signal, both in controlling the amplitude of the signal and the speed with which it travels across the cell. This was evident following adjustments in the diffusion constant of the endogenous buffer by which I have shown that a previously published value of 20 $\mu m^2 s^{-1}$ resulted in the modelled Ca^{2+} signal diffusing to the centre of the cell more slowly than was seen in the experimental data. By increasing the diffusion constant of the endogenous buffer by a factor of five a good fit to the experimental data could be obtained.

Looking at the changes in Ca^{2+} concentration at the three standard points within the cell following a influx of Ca^{2+}, representing a depolarisation-induced Ca^{2+} influx, with and without the presence of the Ca^{2+} indicator OG488BD, shows that the Ca^{2+} concentrations 3 μm in from the edges of the cell reach half-maxiumum within 2 msec of each other and the signals diffuse to the centre of the cell with an identical propagation rate. This result shows that the inclusion of a Ca^{2+} indicator dye does not adversely affect the Ca^{2+} signal it is intended to measure as well as emphasising the point that the majority of the Ca^{2+} signal is communicated throughout the cell by endogenous mobile buffers.

7 MITOCHONDRIA EXPERIMENTS

While the previous chapter has shown that a good fit to the experimental data could be obtained by increasing the diffusion constant of the endogenous buffer five-fold, I was interested in seeing if there were any other significant contributors affecting the temporal and spatial spread of Ca^{2+} within the cell whose inclusion in the model might correct the problems of the slow diffusion of the Ca^{2+} signal to the centre of the cell and the predicted hotspots under the plasma membrane.

As reported in the introduction, many studies have reported spatially-localised mitochondria, positioned so as to expose the low affinity uniporter, responsible for taking up Ca^{2+} into the mitochondrial matrix, to domains of high Ca^{2+} (Rizzuto *et al.*, 1993; Hongpaisan *et al.*, 2001; Rizzuto *et al.*, 2004; Varadi *et al.*, 2004). However, the role of mitochondria in buffering Ca^{2+} from the cytosol has been debated for some time and varies significantly between cell types.

In pancreatic acinar cells, mitochondria have been shown to act as a significant barrier to Ca^{2+} diffusion, preventing large Ca^{2+} loads generated at the primary Ca^{2+} release sites in the granule-rich apical pole from diffusing to the basal part of the cell containing the nucleus (Tinel *et al.*, 1999). In neurones, many studies looking at cell bodies have shown that the mitochondria are capable of accumulating very large amounts of Ca^{2+} from the cytosol, and while, at pre-synaptic terminals, mitochondria have been previously thought to only take up Ca^{2+} following very large Ca^{2+} loads, primarily acting as energy sources for the ATP-dependent Ca^{2+} pump across the plasma membrane (Zenisek and Matthews, 2000), more recent work has demonstrated that in these areas the mitochondria may still

act as the major organelle regulating Ca^{2+} (Billups and Forsyhe, 2002). The majority of these previous experiments have looked at mitochondrial Ca^{2+} accumulation following cytosolic Ca^{2+} changes far larger than those seen following the short depolarisations used in my experiments.

In sensory neurones, where the primary source of intracellular Ca^{2+} increases is through voltage-gated Ca^{2+} channels, it seems reasonable to hypothesise that mitochondria would be found in the space under the plasma membrane where they would be exposed to the high Ca^{2+} levels seen in my model. If mitochondria are present in such locations, capable of accumulating a large proportion of this Ca^{2+} influx, it may account for the appearance of Ca^{2+} 'hotspots' in my model, where there are no mitochondria, and the absence of such 'hotspots' in the experimental data. The results of experiments designed to address this question are described in this chapter.

7.1 Rhod-2 Experiments

In order to examine the role of mitochondria in chick sensory neurones following small depolarisations, such as the 50 msec ones used in my previous experiments, DRG neurones were pre-loaded with 5 μM Rhod-2 AM (Molecular Probes; dispersed with 62.5 μg/ml Pluronic F-127) and mitotracker green (20 or 200 nM; Molecular Probes) by incubation for thirty minutes at room temperature in growth medium. The AM esters of the Rhod family of Ca^{2+} indicator dyes are positively charged, allowing the dye to accumulate in the negatively charged mitochondria. Once inside, the AM ester group is

cleaved leaving a negatively charged molecule trapped inside the organelle. This technique was used in combination with whole-cell patch clamping to remove any Rhod-2 remaining in the cytosol ensuring a mitochondrial specific Ca^{2+} signal. Simultaneously, patch clamping introduced the Ca^{2+} indicator OG488BD into the neurone.

Mitotracker green, which selectively stains the mitochondria, reveals the organelles to be distributed throughout the cytoplasm, with some even occupying the thin layer of cytoplasm between the nucleus and plasma membrane (as indicated by the white arrow in figure 7.1h).

The patterns of fluorescence from the mitotracker green imaging and the immunofluorescence imaging, described in section 2.6, were very similar (figure 7.1i, j) indicating that the mitotracker green positive organelles were indeed mitochondria. Any mismatch between the fluorescent patterns is likely to be due to movement of individual mitochondria while the cell was still alive and / or distortion of the cell during fixation and processing.

Depolarisation of the neurones for 50 msec to +10 mV resulted in a clear increase of fluorescence in both the OG488BD signal and the Rhod-2 signal (shown later in figure 7.2). At depolarisations of 1 second, the Rhod-2 fluorescent increase was more dramatic and clearly localised to the mitotracker green positive organelles (figure 7.1b,c and f,g).

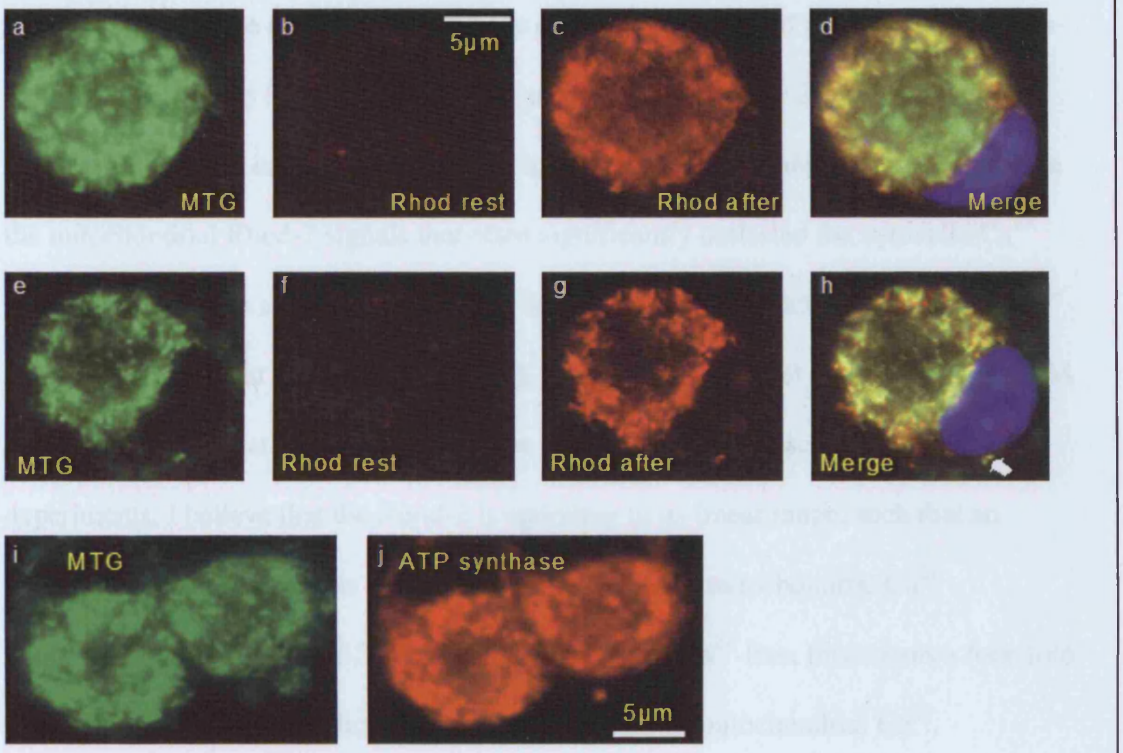

Figure 7.1 Small depolarisations evoke a Ca^{2+} signal in mitochondria

DRG neurones were incubated with mitotracker green (200 nM), Hoechst 33342 (2 µM) and Rhod-2 AM (5 µM) for 30 minutes at room temperature, then whole-cell patch clamped with a pipette in which the Ca^{2+} buffer was 100 µM BAPTA. Two representative cells are shown. One second depolarisations cause a clear rise in Rhod-2 fluorescence within discrete organelles (comparing panel c with b and panel g with f). Overlaying these post-depolarisation images with the relevant images of mitotracker staining shows a clear co-localisation of the areas of increased Rhod-2 fluorescence with the mitotracker positive organelles (panels d and h; nucleus labelled with Hoechst).

In order to demonstrate the selectivity of mitotracker dyes for loading mitochondria, DRG neurones were labelled with 200 nM mitotracker green and imaged whilst alive (panel i) then fixed and stained for mitochondrial ATP synthase using an Alexa 633 conjugated secondary antibody (panel j). These two images show clear co-localisation of antibody-stained areas with the mitotracker positive organelles, indicating that these organelles are indeed mitochondria and that the increases in Rhod-2 fluorescence indicate an increase in mitochondria Ca^{2+}.

Depolarisation of the neurones for 50 msec or 1 second produced inward Ca^{2+} currents that raised $[Ca^{2+}]_c$ by 90 ± 18 nM (n = 20) and 212 ± 33 nM (n = 21) respectively. Depolarisations that caused cytosolic Ca^{2+} to increase over 200 nM evoked increases in the mitochondrial Rhod-2 signals that often significantly outlasted the cytosolic Ca^{2+} elevation and whose amplitudes increased linearly with the amplitude of cytosolic Ca^{2+} (figure 7.2), such that an increase of $[Ca^{2+}]_c$ from the resting level of 129 nM to 500 nM evokes an approximately four-fold increase in the Rhod-2 fluorescence. In my experiments, I believe that the Rhod-2 is operating in its linear range, such that an increase in its fluorescence is proportional to increases in mitochondrial Ca^{2+} concentrations. Since Rhod-2 does not fluoresce when Ca^{2+}-free, this means a four-fold increase of fluorescence indicates a four-fold increase of mitochondrial Ca^{2+}. Fluorescence traces can give a severely distorted report of the timecourse of Ca^{2+} changes if the Ca^{2+} concentrations approach values that saturate the indicator (Milikan *et al.*, 2002). This would result in an artificial plateau in the reported increase of Ca^{2+} concentrations as the indicator would not get any brighter as the Ca^{2+} rises over saturating levels. Similarly, as the Ca^{2+} concentrations fall, this would not be reflected in the Ca^{2+} changes reported by the indicator until the Ca^{2+} fell below saturating levels. In order to check that this was not occurring with my Rhod-2 results, thus accounting for the increased recovery times in mitochondrial Ca^{2+} following higher cytosolic Ca^{2+} changes, a lower affinity indicator, Rhod-FF, was used for the same experiments. Ratio values of increases in OG488BD fluorescence against increases in Rhod-2 and Rhod-FF fluorescence fall well within the same linear pattern on a scatter plot indicating neither indicator is saturating and both are operating within their linear range (Figure 7.2b).

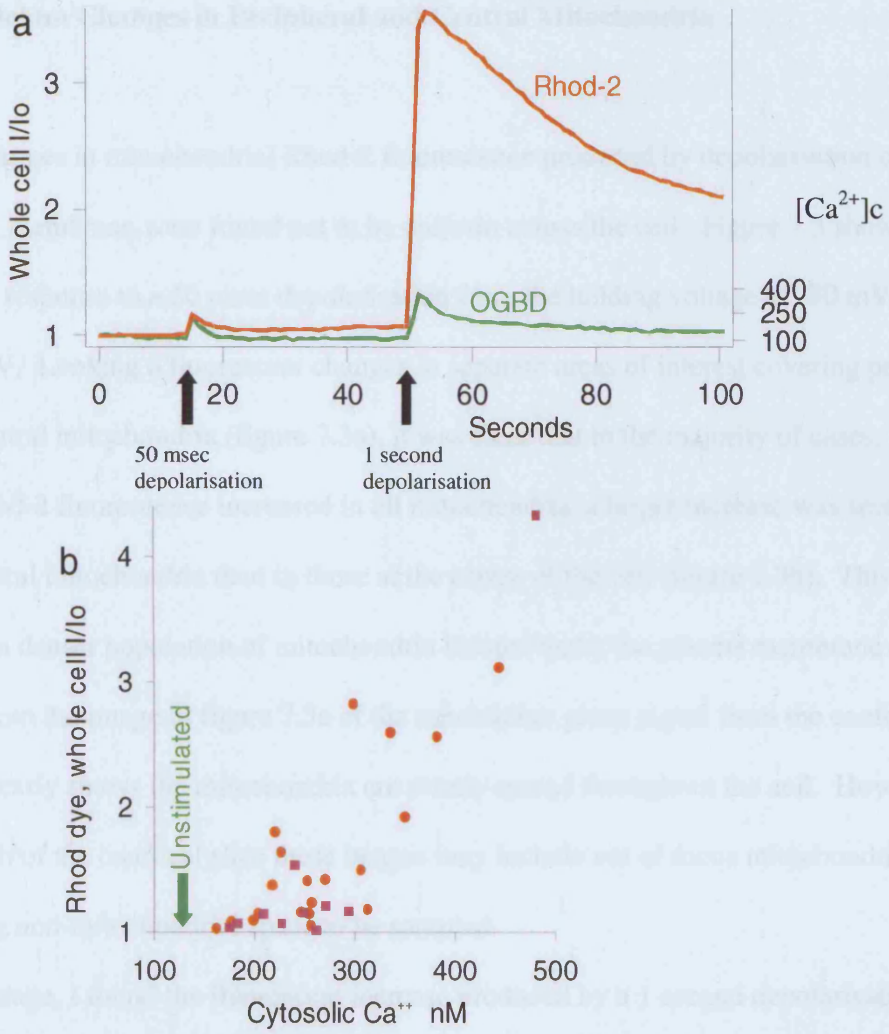

Figure 7.2 Small cytosolic Ca^{2+} elevations evoke significant mitochondrial Ca^{2+} changes

DRG neurones were incubated with Rhod-2 AM (5 μM) for 30 minutes at room temperature, then whole-cell patch clamped using a pipette containing 100 μM OG488BD. (a) shows the normalised Rhod-2 and OG488BD signals from one cell following successive depolarisations of 50 msec and 1 second. The right axis shows the cytosolic Ca^{2+} concentration corresponding to the measured OG488BD fluorescence, assuming a resting $[Ca^{2+}]_i$ of 129 nM as measured using Fura dextran in section 5.2.

(b) Shows the results from many experiments of the type shown in (a), where the peak changes in the Rhod-2 signals (red circles) and Rhod-FF signals (pink squares) are plotted against peak cytosolic Ca^{2+} changes, measured with OG488BD. As the results from both dyes fall within the same scatter plot, this shows that the Rhod-2 signal is not saturating when reporting changes in mitochondria Ca^{2+} and is still operating in its linear range. Only responses to the first applied depolarisation for each cell are plotted.

7.2 Calcium Changes in Peripheral and Central Mitochondria

The changes in mitochondrial Rhod-2 fluorescence produced by depolarisation of the plasma membrane were found not to be uniform across the cell. Figure 7.3 shows a typical response to a 50 msec depolarisation from the holding voltage of -70 mV to +10 mV. Looking a fluorescent changes in separate areas of interest covering peripheral and central mitochondria (figure 7.3a), it was clear that in the majority of cases, although the Rhod-2 fluorescence increased in all mitochondria, a larger increase was seen in the peripheral mitochondria than in those at the centre of the cell (figure 7.3b). This was not due to a denser population of mitochondria located under the plasma membrane as can be seen from the image in figure 7.3a of the mitotracker green signal from the confocal slice. This clearly shows the mitochondria are evenly spread throughout the cell. However, due to depth of the confocal slice these images may include out of focus mitochondria causing non-mitochondrial space to be sampled.

On average, I found the fluorescent increase produced by a 1 second depolarisation to be 54 ± 11 % larger in peripheral mitochondria (defined as those within 3 μm of the plasma membrane) than in the central mitochondria ($n = 18$; $P < 0.001$). The same effect was seen following a 50 msec depolarisation (figure 7.3b); where the post-depolarisation Rhod-2 signal in the peripheral mitochondria was found to be 51 ± 20 % larger than in the central ones ($n = 11$; $P < 5\%$).

In order to observe the timecourses of mitochondrial Ca^{2+} changes, images were taken on a Zeiss confocal microscope at intervals of 98 msec before and after depolarisation.

Following a 50 msec depolarisation, mitochondrial Ca^{2+} increased over 1 – 2 seconds before decaying back to baseline (figure 7.3b). Depolarisations of 1 second duration produced similar but larger elevations in mitochondrial Ca^{2+} but with slower recovery rates than for the smaller 50 msec-induced elevations, such that following the largest increases in mitochondrial Ca^{2+}, the fluorescence recovered with a half-time of many tens of seconds (figure 7.3c).

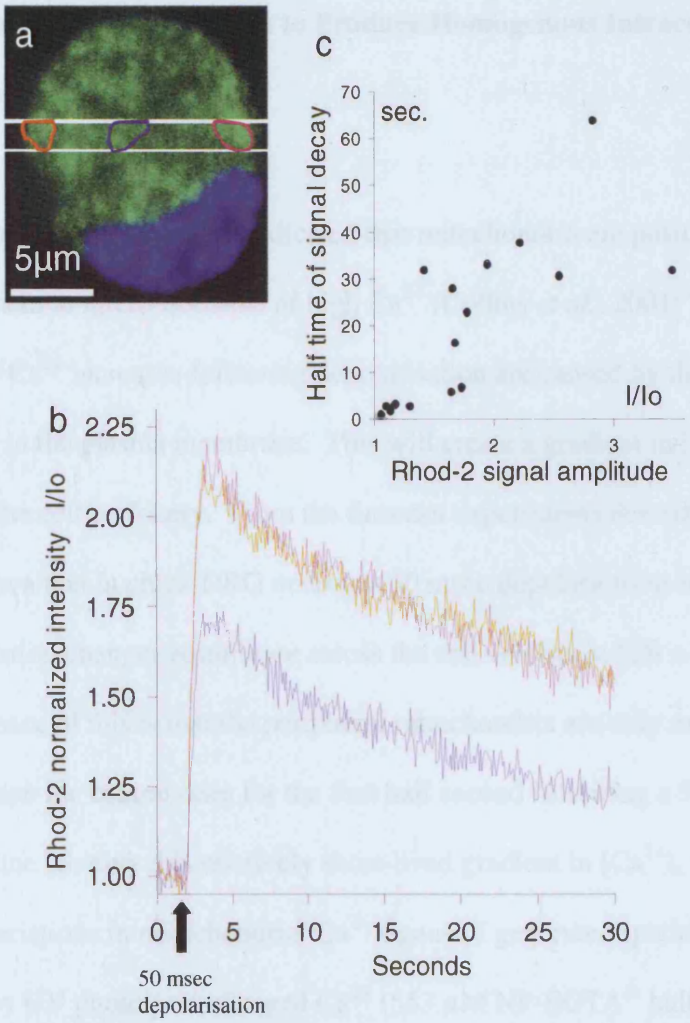

Figure 7.3 Mitochondrial Ca^{2+} signals are larger in peripheral mitochondria

Panel (a) shows a DRG neurone incubated with mitotracker green (200 nM), Hoechst (2 µM) and Rhod-2 AM (5 µM) for 30 minutes at room temperature, then patch clamped with a pipette containing 100 µM BAPTA. Using the mitotracker signal, an area was selected containing both peripheral and central mitochondria (white box) which was scanned for Rhod-2 fluorescence at a resolution of 512 x 50 every 98 msec. Panel (b) shows the normalised increase in mitochondrial Ca^{2+} as indicated by Rhod-2 fluorescence at the three areas indicated in panel (a). At the arrow the cell was depolarised to +10 mV for 50 msec. This clearly shows that the peripheral mitochondria, the red and purple areas, take up more Ca^{2+} from the cytosol following a 50 msec depolarisation than the central mitochondria, the blue area. Panel (c) shows a scatter plot of the amplitude of the global Rhod-2 signal against the half-time of recovery for the Rhod-2 signal back to baseline from many such experiments, using both 50 msec and 1 second depolarisations. This shows that the decay of Rhod-2 fluorescence back to baseline is much slower after large amplitude events.

7.3 Release of Caged Calcium to Produce Homogenous Intracellular Calcium Changes

Numerous publications have indicated that mitochondria are positioned in locations that expose them to micro-domains of high Ca^{2+} (Collins *et al.*, 2001; Park *et al.*, 2001). The cytosolic Ca^{2+} increases following depolarisation are caused by the opening of ion channels in the plasma membrane. This will create a gradient in $[Ca^{2+}]_c$ with the highest value at the cell periphery. From the linsecan experiments described in section 3.2, I have shown that in chick DRG neurones 50 msec depolarisation-induced Ca^{2+} concentration changes equilibrate across the cell volume in 559 ± 88 msec. The consequence of this is that the peripheral mitochondria are only exposed to a higher $[Ca^{2+}]_c$ than the central ones for the first half second following a 50 msec depolarisation. To examine whether this relatively short-lived gradient in $[Ca^{2+}]_c$ was responsible for the spatial variations in mitochondrial Ca^{2+} signals, I generated spatially uniform changes in $[Ca^{2+}]_c$ by UV photolysis of caged Ca^{2+} (553 μM NP-EGTA^{2-} half-saturated with Ca^{2+}; Sigma) loaded into chick DRG neurones via a patch pipette also containing OG488BD and in which the mitochondria were stained with mitotracker deep red (Molecular Probes) and loaded with Rhod-2. Photolytic release of Ca^{2+} evoked larger Ca^{2+} changes in peripheral mitochondria than central mitochondria, even though the cytosolic Ca^{2+} changes, as reported by OG488BD, were the same in both locations (figure 7.4). The Rhod-2 signals were found to be 50 ± 12 % larger in peripheral mitochondria than central ones ($P < 0.001$) while the OG488BD signal was only 4 ± 9 % larger (not significant). Furthermore, the extent to which the signal in the peripheral mitochondria

exceeded that of the central mitochondria almost exactly matched the results seen during the depolarisation-induced Ca^{2+} changes (54 ± 11 % and 51 ± 20 %) suggesting that the larger uptake into the peripheral mitochondria is a consequence of an inherently greater ability to take up Ca^{2+} and not due to exposure to higher concentrations of cytosolic Ca^{2+} concentrations.

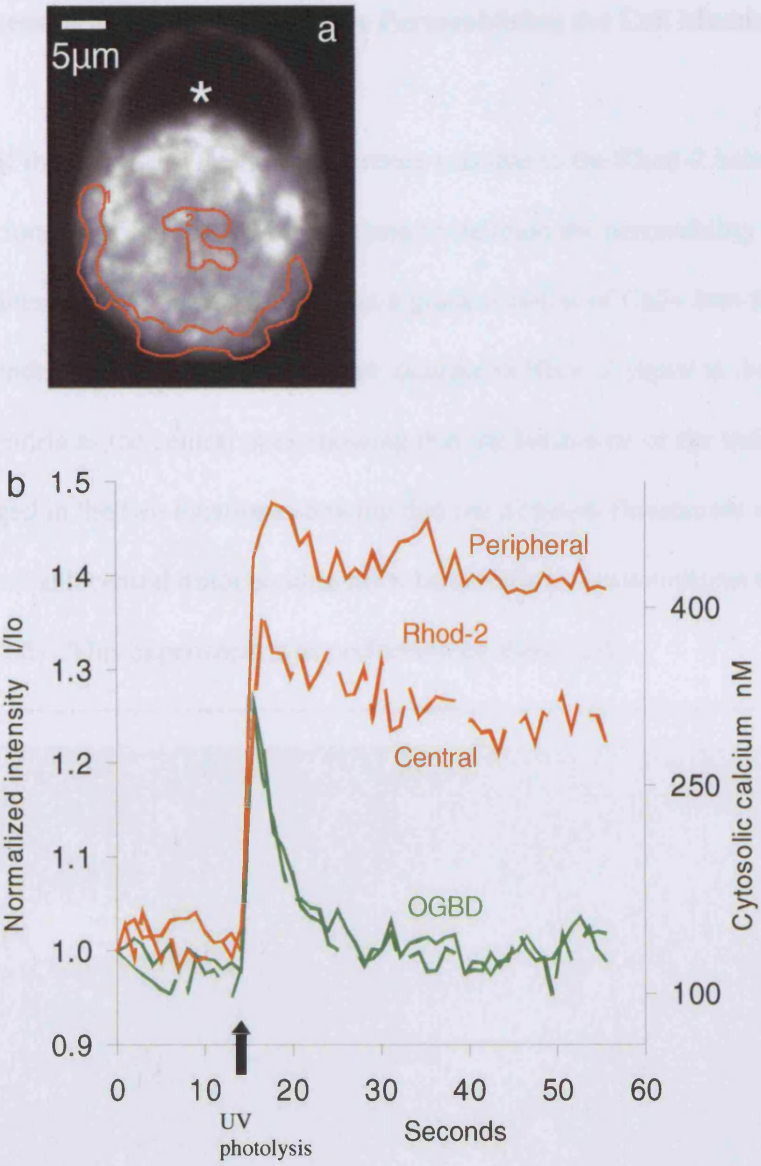

Figure 7.4 Peripheral mitochondria take up more Ca^{2+} when cytosolic Ca^{2+} change is uniform

DRG neurones were incubated with mitotracker deep red (300 nM) and Rhod-2 AM (5 µM) for 30 minutes at room temperature then whole-cell patch clamped using a pipette containing 100 µM OG488BD, 533 µM of the photolabile Ca^{2+} buffer NP-$EGTA^{2-}$ and 267 µM $CaCl_2$. Panel a shows the mitotracker deep red image allowing areas of interest to be selected covering peripheral and central mitochondria. The * symbol denotes the nucleus. A small fraction of the NP-$EGTA^{2-}$ was photolysed by 500 msec of UV light (nominally equal intensities at 351 nm and 364 nm), releasing Ca^{2+} uniformally throughout the neurone. Looking at the fluorescent changes in the two areas of interest for OG488BD and Rhod-2 (panel b), it is clear that while the cytosolic Ca^{2+} changes, reported by OG488BD, are similar in both locations, the mitochondrial Ca^{2+} changes, reported by Rhod-2, are larger at the periphery.

7.4 Increasing Cytosolic Calcium by Permeablising the Cell Membrane

To test if the peripheral / central difference was due to the Rhod-2 behaving differently in the two locations, I used 1 μM ionomycin to increase the permeability of all cell membranes to Ca^{2+}. Ionomycin causes a gradual influx of Ca2+ into the cell and mitochondria. This produced the same increase in Rhod-2 signal in the peripheral mitochondria as the central ones showing that the behaviour of the indicator dye is unchanged in the two locations showing that the different fluorescent signals observed in peripheral and central mitochondria must be an effect of non-uniform Ca^{2+} uptake (figure 7.5). This experiment was performed on three cells.

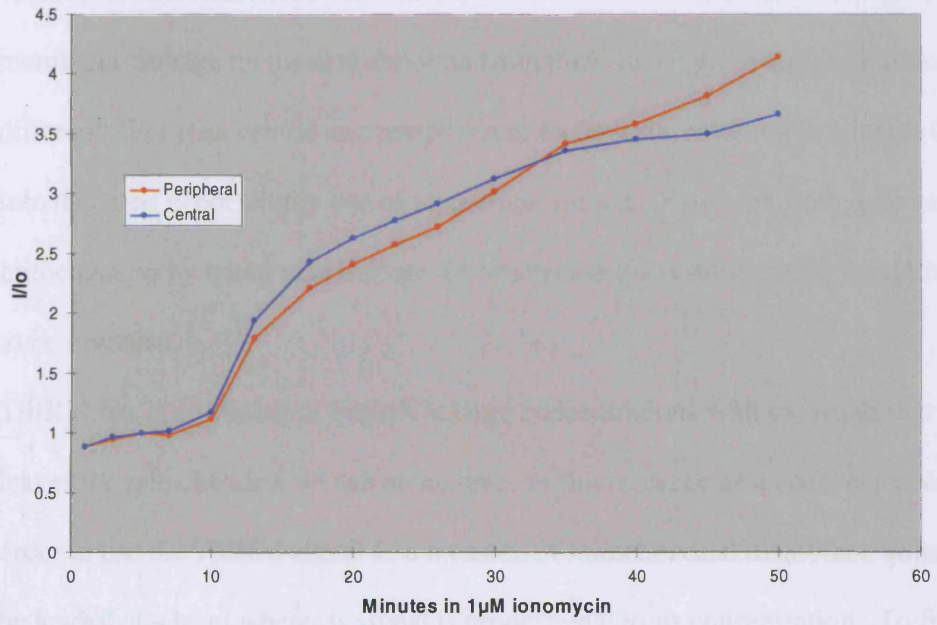

Figure 7.5 Increasing the permeability of the cell membranes to Ca^{2+} with ionomycin

To test that the Rhod-2 indicator dye was behaving in the same manner in both the peripheral and central locations, 1 μM ionomycin was used to increase the permeability of the cell membranes to Ca^{2+}. This resulted in an identical increase in Rhod-2 fluorescence in both peripheral and central mitochondria. The increasing signal reported by Rhod-2 further indicates that the dye is not saturating.

7.5 Mitochondrial Membrane Voltage Measurements

One possible explanation for the greater uptake of Ca^{2+} into peripheral mitochondria is that they have a greater membrane voltage than central mitochondria. To try and reveal this, I co-loaded DRG neurones with the mitochondrial membrane voltage indicator TMRM and mitotracker deep red. TMRM loads mitochondria in direct relation to their membrane potential, such that more energised mitochondria will fluoresce more brightly than less electrically polarised ones. The ratio of TMRM fluorescence to mitotracker deep red fluorescence was not different in the different cell regions (figure 7.6). In ten cells, the value of the ratio I_{TMRM} / I_{MTDR} in peripheral mitochondria was 99 ± 1 % of the value in central mitochondria. One explanation of this is that there is no graduation of membrane voltage on the mitochondria from these two regions suggesting that the difference between central and peripheral mitochondria, resulting in a larger Ca^{2+} uptake into the later, is not simply one of membrane voltage. However, both dyes may load the mitochondria by membrane voltage, in which case the resulting ratio would be expected to be invariant.

TMRM has been shown to quench at large concentrations with the result that as the dye leaves the mitochondria we see an increase in fluorescence as its concentration falls. In order to use the TMRM signal as a measure of mitochondrial membrane voltage it must be loaded at a level where its signal is proportional to its concentration. To find this value, I loaded DRG neurones with incrementally lower concentrations of TMRM, treating them with 10 μM FCCP to depolarise the mitochondrial membrane. If the TMRM was quenching, this depolarisation would result in an initial rise in fluorescence

followed by a fall as the dye leaves the mitochondria. In independent experiments, three cells loaded with 0.2 nM TMRM showed no dequenching upon application of FCCP, unlike cells loaded at 2 or 20 nM TMRM.

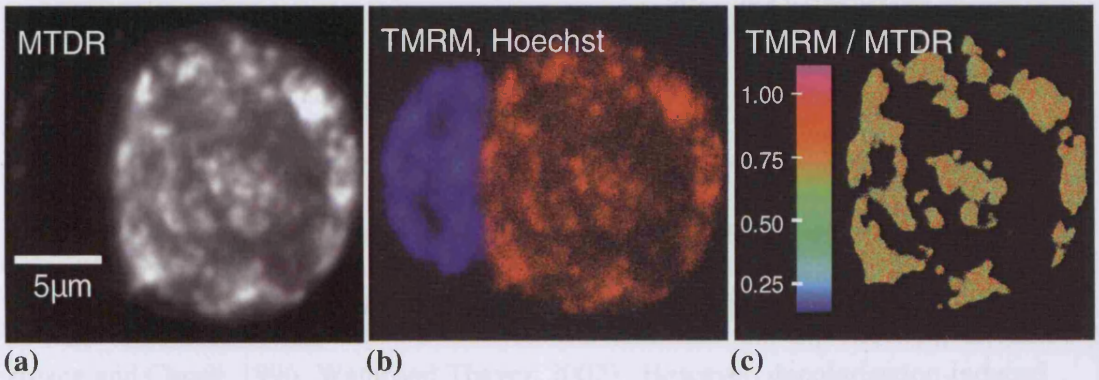

Figure 7.6 TMRM/mitotracker ratio shows no spatial variance in the energised state of mitochondria
In order to see if there was any spatial variation in the energised state of the mitochondria within a resting DRG neurone, cells were incubated with mitotracker deep red (300 nM), the mitochondrial membrane potential indicator tetramethylrhodamine ester (TMRM, 0.2 nM) and Hoechst 33342 (2 µM) for 30 minutes at room temperature then imaged. The mitotracker and TMRM images had background intensities, estimated from regions outside the cell, subtracted (panels a and b) and were then divided pixel by pixel (panel c). The colour in panel c represents the resulting ratio as indicated by the spectral bar. The absolute value of the ratio is a consequence of the laser intensities and detector sensitivities and as such has no biological significance.

7.6 Blocking Mitochondrial Calcium Uptake

7.6.1 Blocking the Mitochondrial Uniporter

Many previous studies have indicated that the mitochondrial membrane potential, generated by a large inside-negative voltage, is the main driving force for Ca^{2+} accumulation into the mitochondria via an as yet unidentified, low-affinity uniporter. This uniporter has been shown to be fully blocked by 100 nM ruthenium red in both avian and mammalian systems (Selles and Boland, 1990; Thayer and Miller, 1990; Huang and Chueh, 1996; Wang and Thayer, 2002). However, depolarisation-induced mitochondrial Ca^{2+} signals in chick DRG neurones were found not to be reduced when the patch pipette contained 1 μM or even 100 μM ruthenium red (figure 7.7).

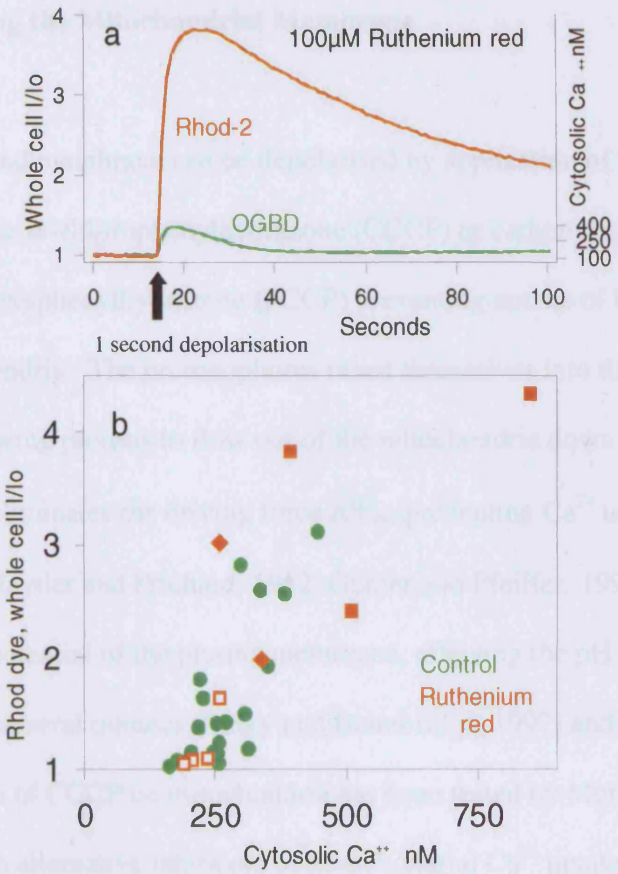

Figure 7.7 Ruthenium red does not inhibit mitochondria Ca^{2+} signals in chick sensory neurones
In an attempt to block mitochondrial Ca^{2+} uptake via the uniporter, neurones incubated with either Rhod-2 AM or Rhod-FF AM (5 μM) for 30 minutes at room temperature were whole-cell patch clamped using a pipette containing 100 μM OG488BD and ruthenium red at either 1 or 100 μM. Panel a shows an example cell patched with a pipette containing 100 μM ruthenium red and depolarised for 1 second at the arrow. The OG488BD and Rhod-2 fluorescent signals, indicating cytosolic and mitochondrial Ca^{2+} changes respectively, are plotted against time, clearly showing an increase in both signals following depolarisation of the neurone. The right-hand axis plots $[Ca^{2+}]_c$, assuming a resting $[Ca^{2+}]_c$ of 129 nM. Panel b displays the results from a number of depolarisation experiments performed with and without the presence of ruthenium red in the patch pipette. The amplitude of the peak Rhod signal is plotted against the peak cytosolic Ca^{2+} change measured with OG488BD. Green dots: control = Rhod-2, no ruthenium red; Hollow red squares = Rhod-2, 1 μM ruthenium red; solid red squares = Rhod-2, 100 μM ruthenium red; solid red diamonds = Rhod-FF, 100 μM ruthenium red. This plot clearly shows that the inclusion of ruthenium red in the patch pipette, at either 1 μM or 100 μM, has no effect on the uptake of Ca^{2+} from the cytosol into the mitochondria following a short depolarisation. Only responses to the first depolarisation are plotted.

7.6.2 Uncoupling the Mitochondrial Membrane

The mitochondrial membrane can be depolarised by application of the protonophores Carbonyl cyanide *m*-chlorophenylhydrazone (CCCP) or carbonyl cyanide *p*-trifluoromethoxyphenylhydrazone (FCCP) preventing uptake of Ca^{2+} from the cytosol into the mitochondria. The protonophores insert themselves into the mitochondrial inner membrane, allowing protons to flow out of the mitochondria down the electrochemical gradient. This eliminates the driving force $\Delta\Psi_m$, preventing Ca^{2+} uptake into the mitochondria (Heytler and Prichard, 1962; Gunter and Pfeiffer, 1990). While CCCP can also act on the potential of the plasma membrane, effecting the pH and ATP levels in cells, this takes several minutes (Sidky and Baimbridge, 1997) and the specificity of a brief application of CCCP on mitochondria has been tested by Murchison *et al.* by direct comparison with alternative inhibitors of mitochondrial Ca^{2+} uptake, rotenone and oligomycin, showing statistically identical results (Murchison *et al.*, 2003).
It has been shown that 1 μM FCCP is sufficient to depolarise the mitochondria and eliminate Ca^{2+} influx through the uniporter (Billups and Forsyhe, 2002).

Cells were loaded with 5 μM Rhod-2 and patched in the normal way with a pipette containing OG488BD. After 3 minutes whole-cell, the cell was depolarised for 50 msec and the resulting Ca^{2+} changes measured. 10 μM FCCP was puffed onto the cell for around 20 seconds before the cell was depolarised again for 50 msec. A third depolarisation of 1 second was performed at the end of the experiment. Depolarisation of

the mitochondria with FCCP did not noticeably reduce the depolarisation-induced Rhod-2 signal.

Figure 7.8a shows a representative example of four experiments performed in this way. This clearly shows an increase in $[Ca^{2+}]_c$ resulting from a depolarisation of the plasma membrane and a corresponding increase in mitochondrial Ca^{2+} both before and after the application of 10 μM FCCP. Furthermore, the application of 10 μM FCCP did not noticeably reduce the amplitude of Rhod-2 signal (figure 7.8b).

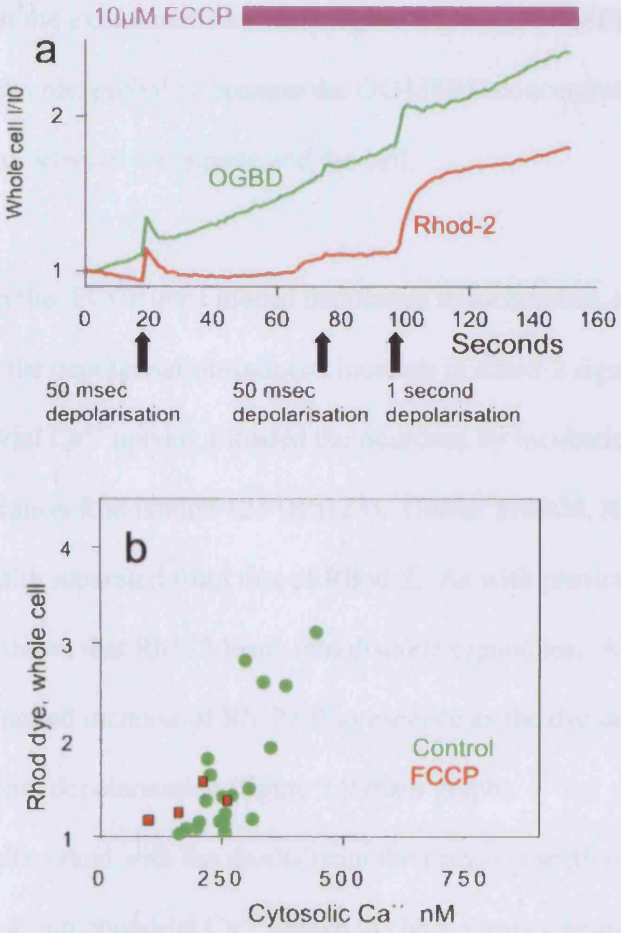

Figure 7.8 Depolarisation of the mitochondrial membrane voltage does not inhibit mitochondrial Ca^{2+} signals

In order to observe the effect of depolarising the mitochondrial membrane on the uptake of Ca^{2+} from the cytosol into the mitochondria, DRG neurones were incubated in 5 μM Rhod-2 for 30 minutes then whole-cell patch clamped using a pipette containing 100 μM OG488BD. Normalised Rhod-2 and OG488BD signals from the entire confocal section are plotted as successive depolarisations of 50 msec, 50 msec and 1 second were applied as indicated by the arrows. During the time indicated by the pink bar, the cell was exposed to 10 μM of the mitochondrial uncoupler FCCP to depolarise the mitochondrial membrane. The third depolarisation, performed in the presence of FCCP, evoked a cytosolic Ca^{2+} elevation similar in amplitude to the first, FCCP-free, depolarisation with a corresponding increase in Rhod-2 signal indicating an uptake of Ca^{2+} into the mitochondria. Panel b shows the amplitude of the peak Rhod-2 signal plotted against the peak cytosolic Ca^{2+} change measured with OG488BD. This plot shows no reduction in the amplitude of the Rhod-2 signal for similar increases in cytosolic Ca^{2+} between depolarisations performed in the presence of 10 μM FCCP (red squares) and control experiments (green circles).

Throughout the experiment shown in figure 7.8, the OG488BD signal was drifting steadily upwards, probably because the OG488BD concentrations had not yet equilibrated between the pipette and the cell.

To confirm that FCCP does indeed depolarise mitochondria, and that under these conditions the depolarisation-induced increase in Rhod-2 signal actually does represent a mitochondrial Ca^{2+} uptake, I loaded the neurones by incubation with 2 nM of the lipophilic cation Rhodamine 123 (Rh123). Unlike TMRM, Rh123 has an emission that can be readily separated from that of Rhod-2. As with previous mitochondrial indicators, figure 7.9 shows that Rh123 loads into discrete organelles. Application of 10 μM FCCP caused a marked increase of Rh123 fluorescence as the dye dequenched upon mitochondrial depolarisation (figure 7.9 main graph).

These results, taken with the results from the previous section using ruthenium red, indicate that mitochondrial Ca^{2+} uptake in chick sensory neurones is not achieved via the uniporter.

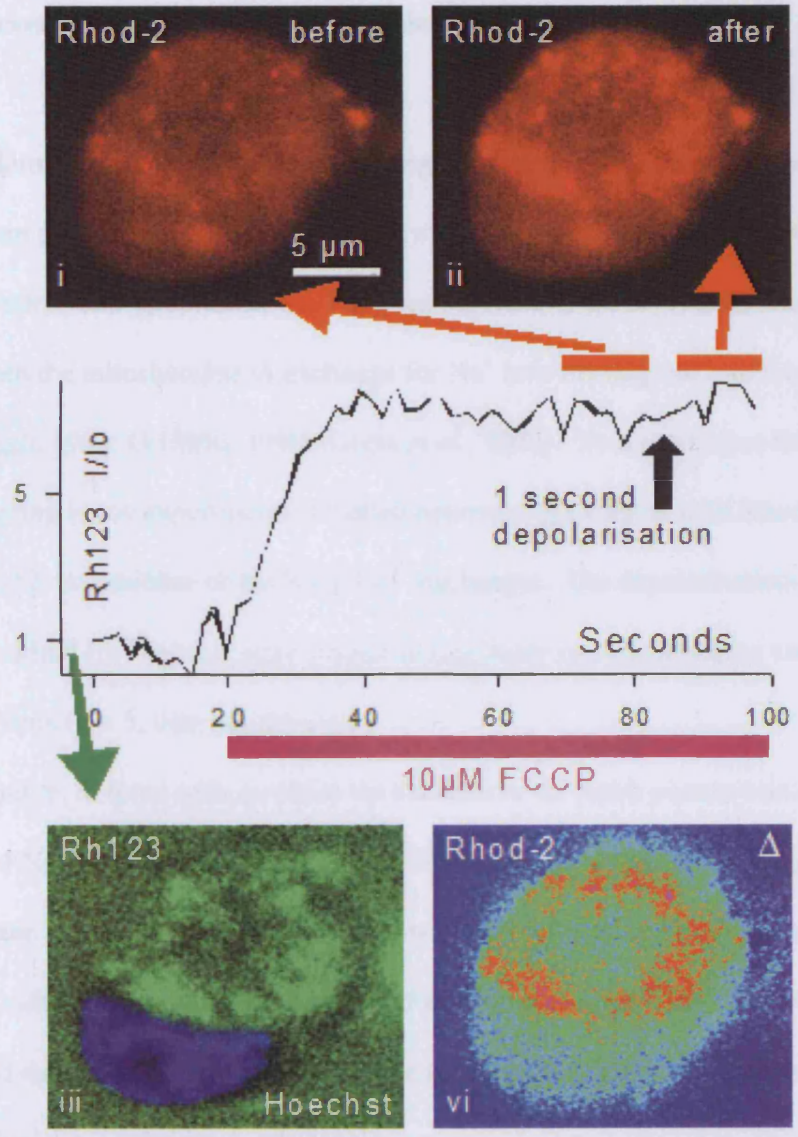

Figure 7.9 FCCP does depolarise the mitochondrial membrane voltage

Panels I and II show the Rhod-2 fluorescence before and after a 1 second depolarisation of the plasma membrane of a neurone bathed in 10 µM FCCP. Panel IV, a difference image, shows that the pattern of Rhod-2 signal evoked by plasma membrane depolarisation matched the pre-FCCP Rh123 image. Any mismatch between the patterns is likely to be due to small changes in the focal plane and / or movement of individual mitochondria. A marked increase in the Rh123 fluorescence is seen upon application of 10 µM FCCP as the dye dequenches with mitochondrial depolarisation (main graph). This indicates that FCCP does act to depolarise the mitochondrial membrane voltage.

This result was representative of four experiments.

7.6.3 Reverse Mode of the Sodium / Calcium Exchanger

The sodium / calcium (Na^+ / Ca^{2+}) exchanger is the pathway associated with removal of Ca^{2+} from the mitochondria back into the cytosol by direct exchange of Na^+ ions for Ca^{2+} ions. Under some conditions, this has been reported to act in reverse, allowing Ca^{2+} to move into the mitochondria in exchange for Na^+ ions moving out into the cytosol (Lipp and Niggli, 1994; Griffiths, 1999; Smets *et al.*, 2004). To test whether this process could be occurring in my experiments, I bathed neurones, pre-loaded with Rhod-2, in 10 μM CGP37157, an inhibitor of the Na^+ / Ca^{2+} exchanger. The depolarisation-induced mitochondrial Ca^{2+} signals were similar in amplitude to corresponding control experiments (n = 5; data not shown).

Furthermore, in three cells in which the caesium in the patch pipette was replaced by 125 mM Na^+, resulting in a large, inward Na^+ gradient across the mitochondrial membrane that will bias the exchanger towards its forward mode, depolarisation-evoked mitochondrial Ca^{2+} signals were observed as normal (figure 7.10). The Na^+ had certainly replaced the cytosolic potassium since the large outward potassium current that would otherwise be recorded upon cell depolarisation was absent after three minutes in the whole-cell configuration (figure 7.3 insert).

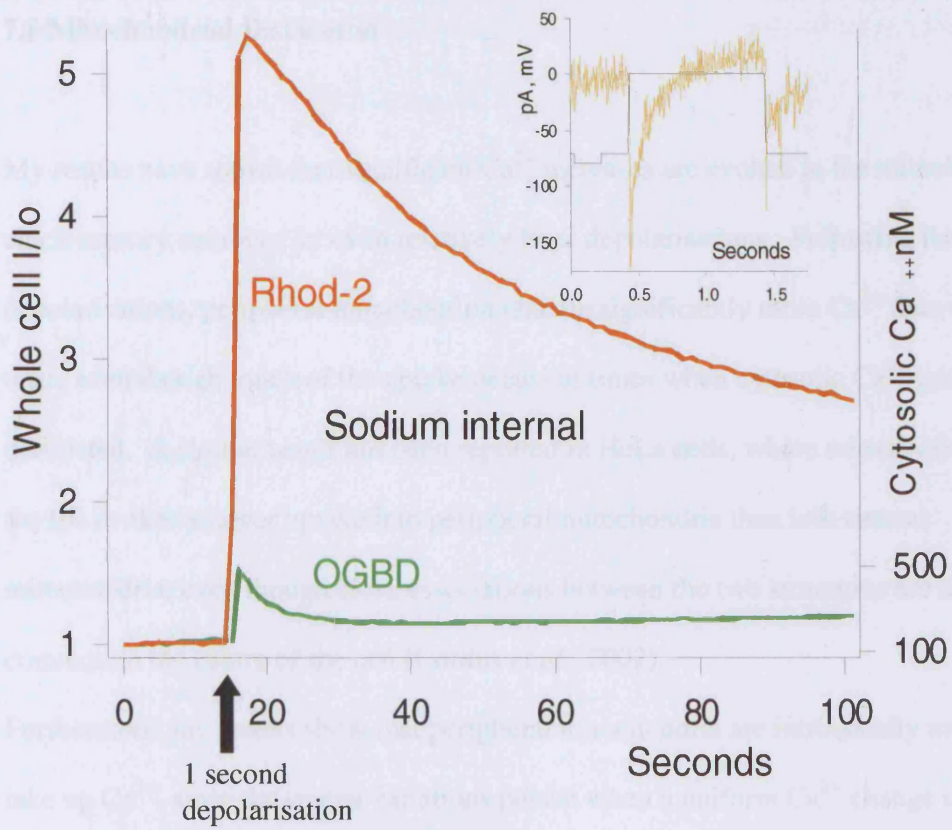

Figure 7.10 Mitochondrial Ca^{2+} signals are normal when cytosolic sodium is high

DRG neurones were incubated with Rhod-2 (5 μM) for 30 minutes. To try and bias the Na^+ / Ca^{2+} exchanger towards its forward mode of removing Ca^{2+} from the mitochondrial matrix in direct exchange from Na^+ ions from the cytosol, these cells were then whole-cell patch clamped with pipettes containing 100 μM OG488BD and in which 125 mM NaCl replaced the standard 125 mM CsCl used in previous experiments. This would set up a high Na^+ gradient across the mitochondrial membrane inhibiting the exchanger from acting in reverse mode. The main graph shows normalised Rhod-2 and OG488BD signals from the entire confocal cell section. At the arrow, the cell was depolarised for 1 second resulting in clear rises in both Rhod-2 and OG488BD fluorescence, indicating increases in cytosolic and mitochondrial Ca^{2+} levels. The right-hand axis plots $[Ca^{2+}]_c$ corresponding to the measured OG488BD fluorescence, assuming resting $[Ca^{2+}]_c$ of 129 nM.

The inset shows the whole-cell current recorded during the 1 second depolarisation. The fact that an inward Ca^{2+} current can be easily detected indicates that intracellular potassium, which would otherwise generate a large outward potassium current, has been removed.

7.8 Mitochondrial Discussion

My results have shown that significant Ca^{2+} increases are evoked in the mitochondria of chick sensory neurones by even relatively brief depolarisations. Following these brief depolarisations, peripheral mitochondria take up significantly more Ca^{2+} than central ones, even though much of the uptake occurs at times when cytosolic Ca^{2+} gradients have dissipated. A similar result has been reported in HeLa cells, where release of Ca^{2+} from the ER evokes a larger uptake into peripheral mitochondria than into central mitochondria, even though close associations between the two structures are more common in the centre of the cell (Collins *et al.*, 2002).

Furthermore, my results show that peripheral mitochondria are intrinsically more able to take up Ca^{2+}, since the spatial variations persist when a uniform Ca^{2+} change is evoked by photolysis of caged Ca^{2+}. The difference cannot simply be one of mitochondrial membrane voltage, since the mitochondrial Ca^{2+} uptake I have observed is not affected by changes of mitochondrial membrane voltage by FCCP. Indeed, comparison of TMRM and mitotracker deep red fluorescence indicated that there was no difference in mitochondrial membrane voltage between peripheral and central mitochondria.

Attempts to block this uptake by either specific inhibition of the mitochondrial uniporter, with ruthenium red, and the Na^{+} / Ca^{2+} exchanger, with CGP37157, or depolarising the mitochondria with FCCP did not affect the mitochondrial Ca^{2+} accumulation indicating that the uptake is not occurring via either of these routes.

A separate pathway for Ca^{2+} accumulation into the mitochondria has been identified in rat liver mitochondria. Labelled the rapid uptake mode (RaM), this has been shown to operate early in a Ca^{2+} challenge, sequestering Ca^{2+} into the mitochondria (Sparagna *et al.*, 1995). However, the RaM has been shown to be blocked by 0.5 μM ruthenium red. Thus, if this was the pathway for Ca^{2+} accumulation into the mitochondria following depolarisation of the plasma membrane it should have been blocked along with the uniporter. The uptake I have observed is therefore likely to occur via a novel pathway. Since the uptake is not strongly affected by the mitochondrial membrane voltage, it is likely to be more or less electroneutral.

The mitochondria make up only 1.5 % by volume of the total cytoplasm (McLain and Weinstein, 1993) and experience Ca^{2+} concentration changes of a similar amplitude as the surrounding cytosol. While these mitochondrial Ca^{2+} changes might be sufficient to account for the differences between my modelled results and the experimental data, it seems more likely that they are too small to significantly affect cytosolic Ca^{2+} dynamics. Rather, they may act as a signal system allowing the mitochondria of the neurone cell body to adjust their metabolism to match physiologically relevant changes of electrical activity. In order to test their effects on Ca^{2+} dynamics, I have included a mitochondrial uptake and release system in my cellular models as described in the following chapter.

8 MODELLING THE EFFECTS OF MITOCHONDRIAL CALCIUM UPTAKE

From the experiments in the previous chapter I have shown that the mitochondria in chick DRG neurones take up Ca^{2+} from the cytosol following 50 msec and 1 second depolarisations. To see the effects this has on intracellular Ca^{2+} dynamics, I included mitochondria in the cytoplasmic domain of my model.

8.1 Mitochondrial Parameters

Mitotracker green images (such as figure 7.1) have shown that mitochondria are distributed more or less uniformly throughout the cytoplasm. Measurements on dorsal root ganglion neurones indicated that mitochondria occupy 1.5 % of the total volume (McLain and Weinstein, 1993). I have therefore modelled the mitochondria as distinct, membrane enclosed, sub-domains distributed uniformly throughout the cytoplasm and occupying 1.5 % of the total volume. There is no quantification of mitochondrial distribution in this cell type and the assumption of a homogenous distribution has been made for simplicity in modelling. However, as I shall show later this provides a good approximation to the patterns of mitochondrial Ca^{2+} uptake in embryonic chick DRG neurones.

Measurements I have made from electron microscopy images of neuronal chick mitochondria published by Perkins *et al.* show that the mitochondria can be well modelled as simple spheroidal structures with a minor axis of 325 nm and a major axis of

450 nm (Perkins *et al.*, 1997), values that agree with those previously measured in other cell types such as mitochondria in mouse embryonic stem cells with diameters of around 0.5 μm (Chen *et al.*, 2005). Using the standard equations for volume and surface area of a spheroid, results in a surface to volume ratio of roughly 10 μm^{-1}. Fluxes into and out of the mitochondria were expressed in terms of this simple area term, that is the extra area generated by the mitochondrial cristae was ignored. For simplicity, I have based the mitochondria in my models on the two-dimensional images provided by electron microscopy and do not take into account the complex network of mitochondria present in three-dimensions.

I have modelled Ca^{2+} taken up into the mitochondria via a population of channels and released back into the cytosol via a population of pumps.

Villalobos *et al.* have previously shown that Ca^{2+} uptake and efflux from the mitochondria follow second order Michaelis-Menton kinetics as shown below (Villalobos *et al.*, 2002).

$$J_{uptake} = CaC\_mitochondria * V_{max\_in}^{mito} * \frac{\left([Ca^{2+}]_c - [Ca^{2+}]_{rest}\right)^2}{K_{mito\_in}{}^2 + [Ca^{2+}]_{mito}{}^2}$$

Equation 8.1

$$J_{release} = CaP\_mitochondria * V_{max\_out}^{mito} * \frac{\left([Ca^{2+}]_{mito} - [Ca^{2+}]_{mito\_rest}\right)^2}{K_{mito\_out}{}^2 + [Ca^{2+}]_{mito}{}^2}$$

Equation 8.2

Where $CaC\_mitochondria$ and $CaP\_mitochondria$ represent the concentration of channels and pumps respectively in the mitochondrial membrane, $V^{mito}_{max\_in}$ and $V^{mito}_{max\_out}$ define the maximum flux flowing in and out of the mitochondria, K_{mito_in} and K_{mito_out} are the Michaelis constants for the channels and pumps respectively and $[Ca^{2+}]_{rest}$ and $[Ca^{2+}]_{mito\_rest}$ are the resting concentrations of Ca^{2+} in the cytosol and mitochondria. The resting concentration for Ca^{2+} in the cytosol was taken as the previously measured value of 129 nM (section 5.2). The resting concentration for Ca^{2+} in the mitochondria has been taken from the previously published value of 250 nM by Pitter *et al.* (Pitter *et al.*, 2002). This value is measured at a cytosolic Ca^{2+} level of 140 nM which is close to my measured resting $[Ca^{2+}]_c$.

Values for K_{mito_in} and K_{mito_out} have been taken from previously published values of 23 μM and 217 μM respectively (Villalobos *et al.*, 2002).

8.2 Mitochondria Modelled with a Three-Fold Calcium Uptake

From my experiments in the previous chapter using Rhod-2 to indicate mitochondrial Ca^{2+} changes, I have seen that following a 50 msec depolarisation, the Rhod-2 fluorescence increases by a maximum of roughly 3-fold. As Rhod-2 has been shown to be operating within its linear range, and does not fluoresce at zero Ca^{2+} levels, this corresponds to a 3-fold increase in mitochondrial Ca^{2+} concentration. In order to see if these small increases in mitochondrial Ca^{2+}, from a resting concentration of 250 nM up to

roughly 750 nM, have any effect on the intracellular Ca^{2+} dynamics, I included the mitochondria in two of my existing cellular models with a 3-fold Ca^{2+} uptake from the cytosol into the mitochondria. The diffusion constant of the endogenous buffer was set to 100 $\mu m^2 s^{-1}$ in order to match the propagation of the Ca^{2+} signal to the centre of the cell with the experimental data, as described in section 6.11.3. No other parameters were altered in the models.

The time taken for the mitochondrial Ca^{2+} concentration to return to resting levels varied from cell to cell. However, there was a general, positive, linear relationship in the half-time of this decay with the size of the increase in Rhod-2 fluorescence. This is shown in figure 7.3 where the amplitude of the Rhod-2 signals were plotted against the half-time of recovery for the Rhod-2 signal back to baseline from experiments using both 50 msec and 1 second depolarisations. The resulting scatter plot shows a linear relationship such that the decay of Rhod-2 fluorescence back to resting levels is much slower after large amplitude events.

From this plot, where the mitochondrial Ca^{2+} concentration increased by 3-fold from its resting concentration it would have a half-time of recovery of roughly 40 seconds.

Keeping the concentration of channels and pumps in the mitochondrial membrane constant, the only parameters used to adjust the mitochondrial Ca^{2+} accumulation and release are $V^{mito}_{max\_in}$ and $V^{mito}_{max\_out}$.

In order that the mitochondria accumulate 3-times their resting Ca^{2+} concentration and subsequently release this back into the cytosol with a half-time of roughly 40 seconds $V^{mito}_{max\_in}$ and $V^{mito}_{max\_out}$ were set at -30 $\mu M\ s^{-1}$ and 150 $\mu M\ s^{-1}$ respectively for cell 240604

and -50 $\mu M\ s^{-1}$ and 100 $\mu M\ s^{-1}$ respectively for cell 190105. By convention, negative values indicate inward fluxes.

The mitochondrial Ca^{2+} accumulation for one exemplar cell, following a 50 msec depolarisation is shown in figure 8.1.

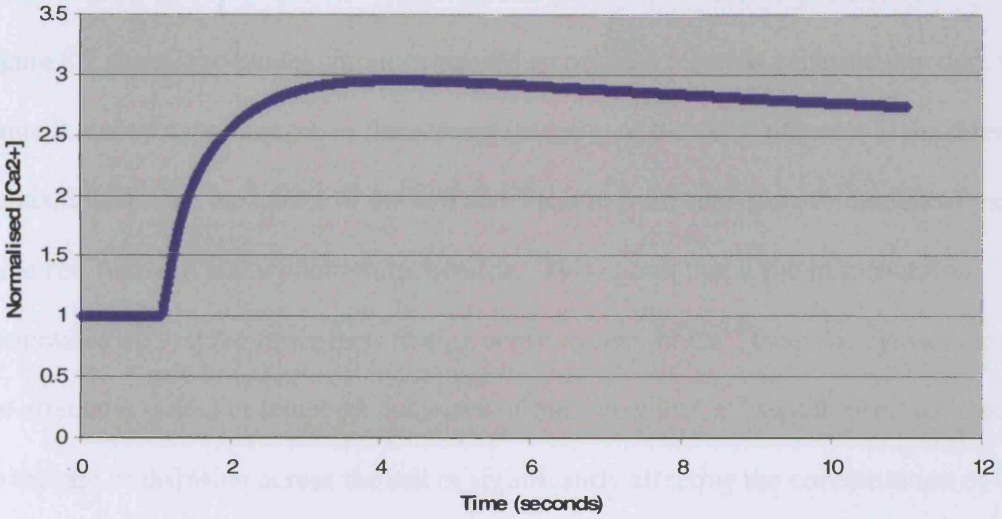

Figure 8.1 Mitochondrial Ca^{2+} uptake

This plot shows the temporal evolution of normalised mitochondrial Ca^{2+} in the model of cell 190105 following a simulated 50 msec depolarisation. The diffusion constant of the endogenous buffer was set at 100 $\mu m^2\ s^{-1}$ to fit the propagation of the Ca^{2+} signal to the centre of the cell, as measured in the experimental data. Mitochondria were included in the model taking up 1.5 % of the cytosolic volume and accumulating 3 times their resting Ca^{2+} concentration of 250 nM from the cytosol as reported by the Rhod-2 experiments. This was released back in the cytosol with a half-time of around 40 seconds.

8.2.1 Effect of a Three-Fold Increase in Mitochondrial Calcium on Cytosolic Calcium Dynamics

When I compared the cytosolic Ca^{2+} dynamics predicted by the models run with and without the presence of mitochondria, this small mitochondrial Ca^{2+} uptake had very little effect on propagation of the Ca^{2+} signal resulting from a 50 msec depolarisation. Figure 8.2 shows the model output compared against the relevant experimental data while figure 8.3 shows the changes in fluorescent intensity of the Ca^{2+} indicator at the three standard locations; the centre of the cell and 3 μm in from each side, in models of the same cell run with and without mitochondria. This shows that if the mitochondria accumulate up to three times their resting concentration of Ca^{2+} from the cytosol they do not affect the spatial or temporal dynamics of the cytosolic Ca^{2+} signal by either speeding up the rate of diffusion across the cell or significantly affecting the concentration of Ca^{2+} bound to the mobile buffers. In fact, the presence of the mitochondria in my models slightly increases the amount Ca^{2+} available to the mobile buffers as the space they occupy in the cytosol increases the density of Ca^{2+} ions by an amount that is not balanced by the mitochondrial accumulation of Ca^{2+}.

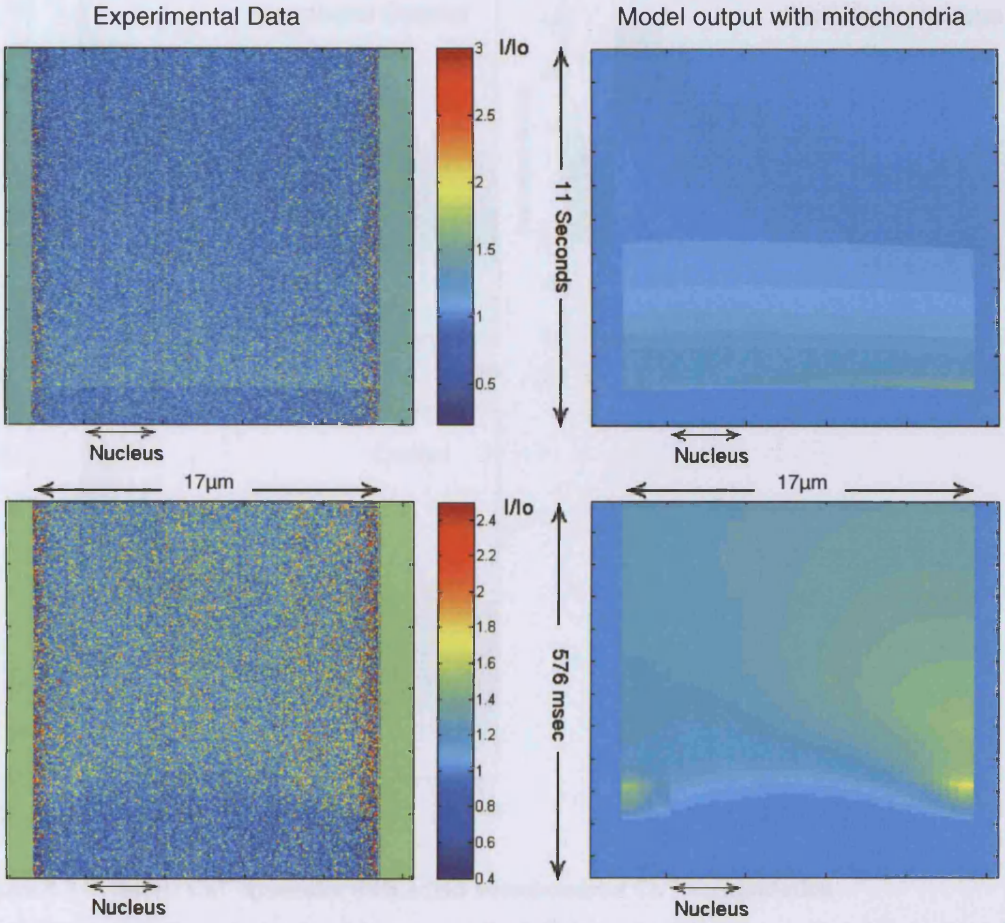

Figure 8.2 Effect of a 3-fold Ca^{2+} accumulation into the mitochondria

In order to see the affect of mitochondria on intracellular Ca^{2+} dynamics following small depolarisations, I included these organelles in my cellular models taking up three times their resting concentration of Ca^{2+} from the cytosol as indicated by my results using the indicator dye Rhod-2. The normalised model output from cell 190105 modelled with the mitochondria is shown here along side the relevant normalised experimental data, for the full 11 seconds of experiment and the 576 msec around the 50 msec depolarisation.

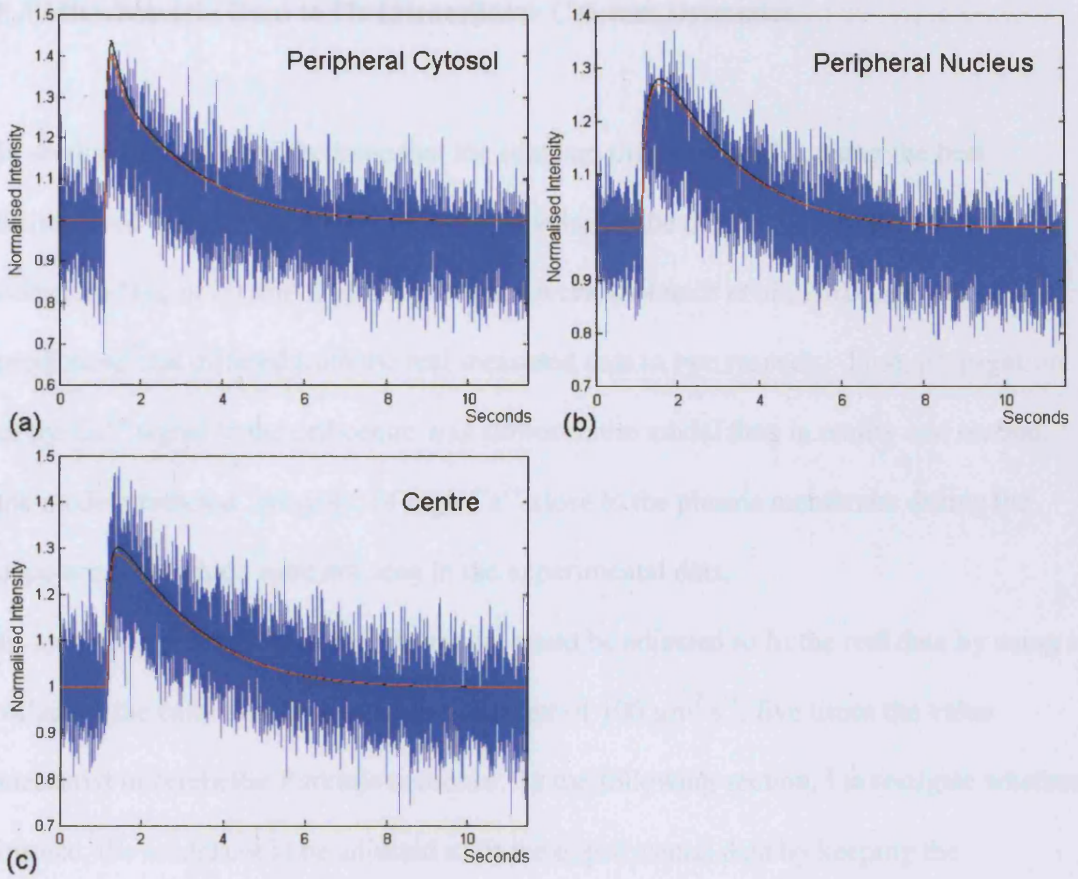

Figure 8.3 Cytosolic Ca^{2+} dynamics with 3-fold mitochondrial Ca^{2+} accumulation

In order to see the affect of mitochondria on cytosolic Ca^{2+} dynamics following small depolarisations, I included these organelles in my cellular models taking up three times their resting concentration of Ca^{2+} from the cytosol as reported by the indicator dye Rhod-2. Results shown here from cell 190105 display the normalised OG488BD fluorescence intensity changes at the centre of the cell and 3 μm in from the plasma membrane on each side from the experimental data, the blue trace, and the model output, the red and black traces. The model output from my previous model with no mitochondria and the diffusion constant of the endogenous buffer set at 100 $\mu m^2 s^{-1}$ (red trace) is displayed along with the output from a second model, identical apart from the inclusion of mitochondria taking up three times their resting concentration of Ca^{2+} (black trace). These show no significant difference in the cytosolic Ca^{2+} dynamics. Including the mitochondria does result in a small increase in cytosolic Ca^{2+} concentration as the mitochondria occupy space in the cytosol that would otherwise be available to species such as free Ca^{2+} and Ca^{2+} bound to indicator dye. This increases the concentration of these species in the remainder of the cell.

8.3 Mitochondria Used to Fit Intracellular Calcium Dynamics

In section 6.11, I raised the issue that the standard diffusion model, using the best estimates of cellular parameters including a value of the diffusion constant for calbindin-D_{28k} of 20 $\mu m^2 s^{-1}$ from published work (Schmidt *et al.*, 2005), generated predictions that differed from the real measured data in two respects. First, propagation of the Ca^{2+} signal to the cell centre was slower in the model than in reality and second, the model predicted 'hotspots' of high Ca^{2+} close to the plasma membrane during the depolarisation which were not seen in the experimental data.

In section 6.11.3, I showed that the model could be adjusted to fit the real data by using a value for the calbindin-D_{28k} diffusion constant of 100 $\mu m^2 s^{-1}$, five times the value measured in cerebellar Purkinje neurones. In the following section, I investigate whether, instead, the model could be adjusted to fit the experimental data by keeping the calbindin-D_{28k} diffusion constant at 20 $\mu m^2 s^{-1}$ and including mitochondria in my model, with very high Ca^{2+} buffering capacities, allowing them to take up very large concentrations of free Ca^{2+} from the cytosol. This, in turn, would allow me to include less endogenous buffer in my models. As I have shown previously in chapter 6, the endogenous buffer is a dominant factor in the communication of the Ca^{2+} signal across the cell. By reducing the concentration of endogenous buffer, the speed of propagation of the Ca^{2+} signal to the centre of the cell is increased. The endogenous buffer concentration was reduced to the level required to remove any mismatch between the diffusion of the Ca^{2+} signal to the centre of the cell in the model output and the experimental data. The mitochondrial Ca^{2+} uptake was in turn adjusted to buffer the

increased levels of free Ca^{2+} in the cell and return these concentrations back to the levels seen in the experimental data.

This was done in two cells; 246040 and 190105. The model for cell 190105 contained the largest concentration of endogenous buffer out of my five exemplar cells and as a result displayed the largest mismatch between the timecourses of diffusion to the centre of the cell in my model and the experimental data.

8.3.1 Reducing the Endogenous Buffer to Speed up Diffusion

In order to speed up the diffusion of the Ca^{2+} signal to the centre of the cell sufficiently to match the experimental data, the total concentration of endogenous buffer in the model of cell 190105 had to be reduced from over 360 μM to just over 90 μM, a 4-fold decrease. The model of cell 240604, on the other hand, had to have its entire endogenous buffer removed to fit the experimental data. In both cases this resulted in a large increase of free Ca^{2+} and of Ca^{2+} bound to the indicator dye. To reduce these concentrations to the levels measured in the centre of the cell from the experimental data, the mitochondria had to take up almost 9000 times and 4456 times their resting concentration for cells 190105 and 240604 respectively. This corresponds to the mitochondrial Ca^{2+} concentration increasing from the resting value of 250 nM to 2.2 mM and 1.1 mM respectively. As no data is available for the half-time of recovery for mitochondrial Ca^{2+} increases of these magnitudes, and to continue the linear relationship between the size of the increase of

mitochondrial Ca^{2+}, as indicated by Rhod-2 fluorescence, and the half-time of recovery to resting levels would result in half-times of over a day, I have assumed the mitochondrial Ca^{2+} concentration would return to resting levels with a similar timecourse as that seen for a 3-fold increase.

The results from this model are shown in figure 8.4, showing the changes in fluorescent intensity of the Ca^{2+} indicator following a 50 msec depolarisation at the three standard points within the cell; the centre and 3 μm in from each side, compared against the experimental data. In order to achieve this, $V_{max\_in}^{mito}$ and $V_{max\_out}^{mito}$ were set at -1.2×10^9 μM s^{-1} and 0.8 μM s^{-1} respectively for cell 240604 and -2×10^9 μM s^{-1} and 1 μM s^{-1} respectively for cell 190105; a negative value defines an inward flux.

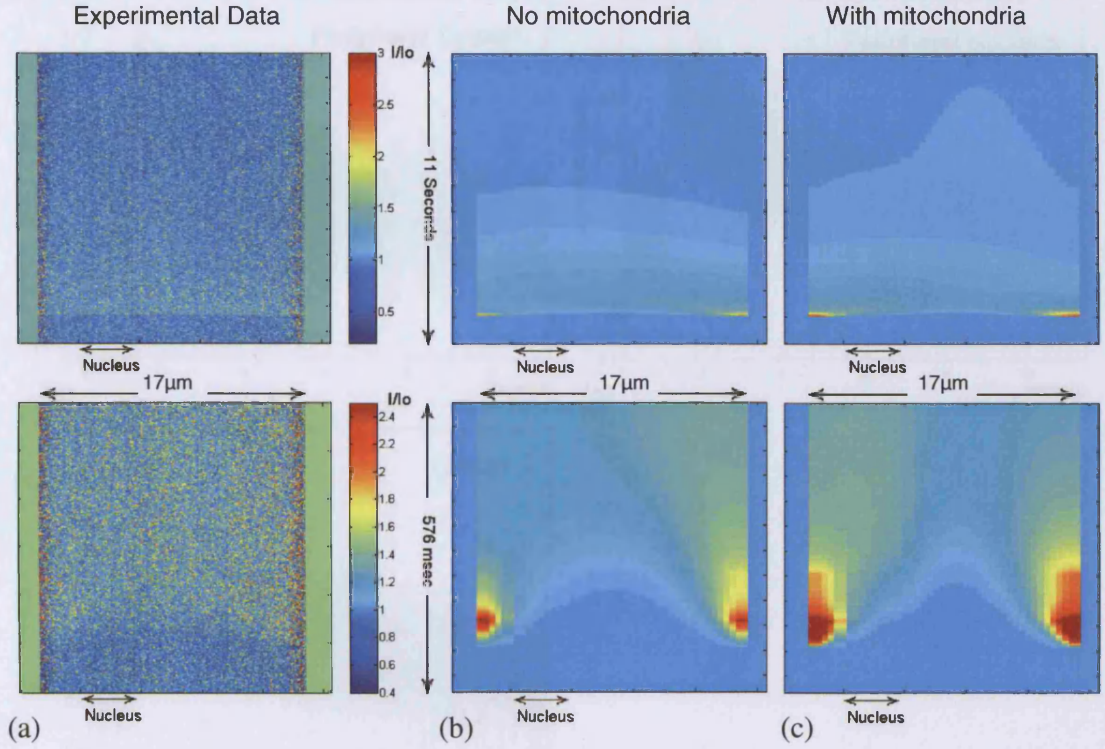

Figure 8.4 Use of mitochondrial Ca^{2+} uptake to modulate intracellular Ca^{2+} signals

In an attempt to use mitochondrial Ca^{2+} uptake as the main variable to modulate the amplitude and rate of diffusion of the Ca^{2+} signals in my cellular models, the endogenous buffer concentrations were reduced to speed up diffusion of the signal to the centre of the cell. The resulting increase in concentration of free Ca^{2+} and Ca^{2+} bound to the indicator dye was buffered by mitochondrial Ca^{2+} uptake. The normalised model outputs from cell 190105 with no mitochondria and the original concentration of endogenous buffer used to fit the experimental data in the section 6.8 (b) and with reduced concentrations of endogenous buffer and mitochondrial Ca^{2+} uptake (c) are shown here along side the relevant normalised experimental data (a), for the full 11 seconds of experiment and the 576 msec around the 50 msec depolarisation. Both models use the standard buffer diffusion constant of 20 $\mu m^2 s^{-1}$. The results from the model using mitochondria to modulate the intracellular Ca^{2+} dynamics shows a clear increase in the 'hotspots' under the plasma membrane as well as a change in the dynamics of the intracellular Ca^{2+} signal.

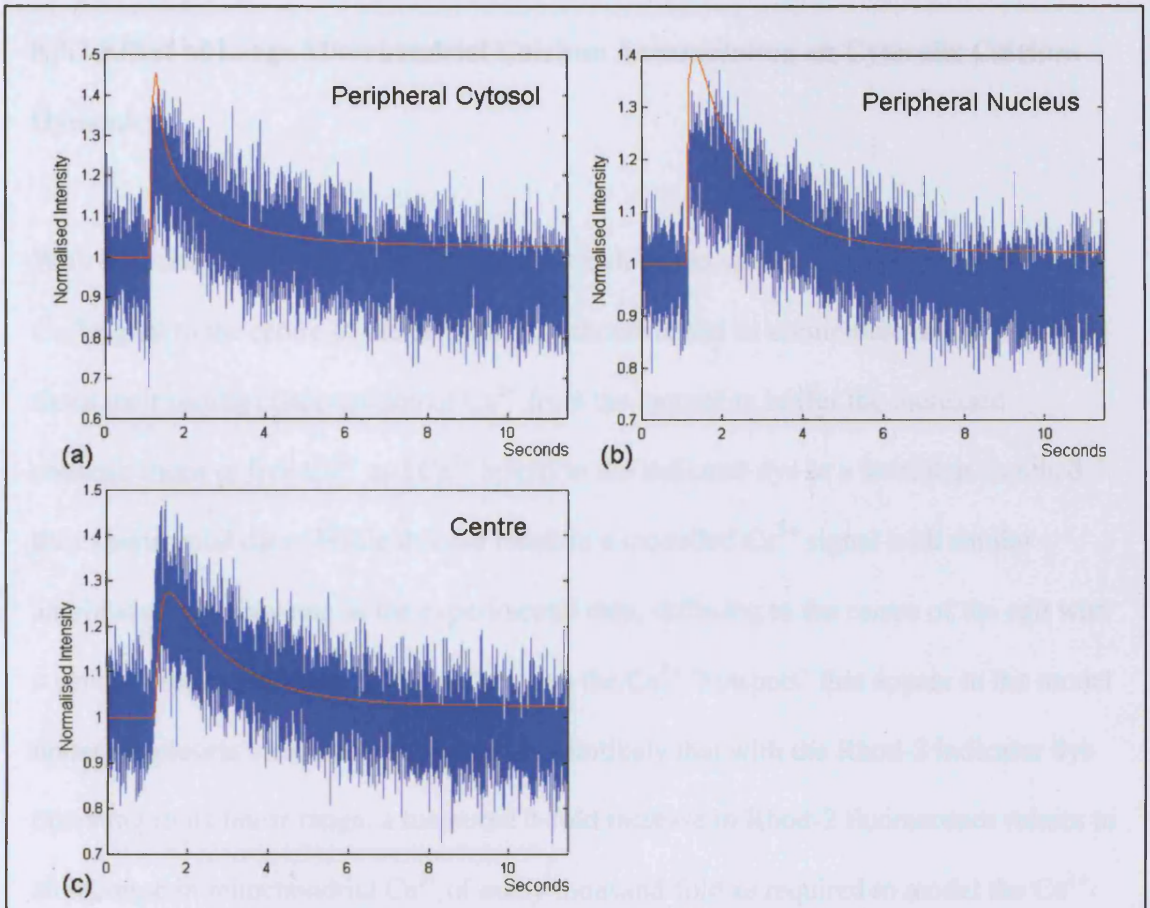

Figure 8.5 Intracellular Ca^{2+} dynamics modulated by mitochondrial Ca^{2+} uptake
Results shown here from cell 190105 display the normalised fluorescent intensity changes at the centre of the cell and 3 μm in from the plasma membrane on each side from the experimental data (blue trace). The model output with the concentration of endogenous buffer reduced to speed up the diffusion of the Ca^{2+} signal to the centre of the cell and the inclusion of mitochondria taking up sufficient Ca^{2+} to reduce the amplitude of the Ca^{2+} signal at the centre of the cell to that matching the experimental data is overlaid (red trace). From this, it can be seen that while this method of using mitochondrial Ca^{2+} accumulation to modulate the dynamics of intracellular Ca^{2+} signals can be used to fit the Ca^{2+} dynamics at the centre of the cell, matching the amplitude of the Ca^{2+} signal and its rate of propagation, it results in large concentration spikes at the edges of the cell which clearly do not fit the experimental data.

8.3.2 Effect of Large Mitochondrial Calcium Accumulation on Cytosolic Calcium Dynamics

With the concentration of endogenous buffer reduced to speed up the propagation of the Ca^{2+} signal to the centre of the cell, the mitochondria had to accumulate many thousand times their resting concentration of Ca^{2+} from the cytosol to buffer the increased concentrations of free Ca^{2+} and Ca^{2+} bound to the indicator dye to a level that matched the experimental data. While this did result in a modelled Ca^{2+} signal with similar amplitude and decay rate as the experimental data, diffusing to the centre of the cell with a similar propagation time, it did not remove the Ca^{2+} 'hotspots' that appear in the model under the plasma membrane. It is also very unlikely that with the Rhod-2 indicator dye operating in its linear range, a measured 3-fold increase in Rhod-2 fluorescence relates to an increase in mitochondrial Ca^{2+} of many thousand-fold as required to model the Ca^{2+} dynamics in this way. The result of this is that while I have shown that the intracellular Ca^{2+} dynamics could be modelled in this way, a far better and more justifiable fit is obtained by a simple increase of the diffusion constant of the endogenous buffer.

8.4 Discussion of Modelling Mitochondrial Calcium Accumulation

These modelling experiments have shown that a mitochondrial Ca^{2+} accumulation increasing the mitochondrial Ca^{2+} concentration to three times their resting levels, as reported by my Rhod-2 experiments, is not sufficient to affect the cytosolic Ca^{2+} dynamics and does not significantly affect the propagation of the Ca^{2+} signal. These results add weight to my hypothesis that the function of this mitochondrial Ca^{2+} uptake is rather to act as a signalling system, allowing the mitochondria to adjust their metabolism to match physiologically relevant changes of electrical activity.

My experiments with Rhod-2 only report the concentrations of unbuffered Ca^{2+} in the mitochondria and do not take into account the large Ca^{2+} buffering capabilities of these organelles. I have shown that when the mitochondrial Ca^{2+} uptake is allowed to increase to millimolar concentrations it can significantly affect the intracellular Ca^{2+} dynamics. However, these models do not fit the Ca^{2+} signals measured with OG488BD.

9 GENERAL DISCUSSION AND CONCLUSIONS

Neuronal Ca^{2+} signalling is involved in a number of cellular events ranging from growth, differentiation and proliferation to apoptosis (Augustine *et al.*, 2003). In order for Ca^{2+} to control this diverse array of cellular processes, intracellular Ca^{2+} signals vary in amplitude and spread depending on their point of origin, whether they are induced through depolarisation of the plasma membrane or by agonist and whether they are amplified by CICR.

My work has focused on examining the dynamics of Ca^{2+} signals produced by short, 50 msec, depolarisations of the plasma membrane in the cell bodies of chick sensory neurones.

9.1 Imaging Intracellular Calcium signals

In order to observe the intracellular Ca^{2+} dynamics following 50 msec depolarisations, I have used patch clamp experiments on DRG neurones, isolated from 12 day chick embryos, in combination with confocal imaging.

From these experiments I have shown that, following a 50 msec depolarisation, Ca^{2+} signals originating at the plasma membrane propagate to the centre of chick DRG neurones within 24 ± 2 msec (n = 20) raising the intracellular Ca^{2+} concentration by 0.96 ± 0.17 μM (n = 32), consistent with previously measured values (Bootman *et al.*, 2001a). This implies that electrical activity would be communicated throughout the cell

without the need for calcium-induced calcium release, rapidly reaching the Ca^{2+} sensors found throughout the cell body.

I have gone on to specifically show that the intracellular Ca^{2+} signals in chick DRG neurones are not propagated by CICR by exposing the neurones to thapsigargin and caffeine in independent experiments. This is the case even when intracellular Ca^{2+} levels are raised significantly over values previously reported to activate CICR in other cell types (Bootman *et al.*, 2001a) by means of long depolarisations or chains of 50 msec depolarisations.

9.1.1 The Nuclear Envelope as a Barrier to Passive Calcium Diffusion

Previous studies have suggested that the nuclear membrane presents a significant barrier to Ca^{2+} diffusion delaying the Ca^{2+} signal (Genka *et al.*, 1999); a barrier that increases as cytosolic Ca^{2+} levels rise (al-Mohanna *et al.*, 1994). Furthermore, there have been reports of the nuclear envelope completely isolating the nucleus from cytoplasmic Ca^{2+} changes (Badminton *et al.*, 1995; Badminton *et al.*, 1996a). Results I have shown in this thesis have shown that nuclear Ca^{2+} levels rise rapidly after increases in $[Ca^{2+}]_c$. I have measured a delay incurred by the Ca^{2+} signal crossing nuclear envelope of 9 ± 2 msec ($n = 38$). This value is consistent with passive diffusion of Ca^{2+} ions into the nucleus through NPCs and indicates that while the nuclear envelope presents a slight barrier to the propagation of the Ca^{2+} signal it is not isolating the nucleus from cytoplasmic Ca^{2+} changes.

9.2 Modelling Intracellular Calcium Dynamics

In order to observe any effect the inclusion of a Ca^{2+} indicator dye has on the intracellular Ca^{2+} dynamics, I generated a mathematical diffusion model using the modelling environment The Virtual Cell. Using values I have measured for resting Ca^{2+} concentrations and the diffusion constant of the indicator dye Oregon Green 488 BAPTA-1 dextran I created models based on five exemplar cells.

By adjusting various parameters in my model I have shown that the endogenous buffer, based on calbindin-D_{28k}, plays a dominant role in the dynamics of the propagation of the intracellular Ca^{2+} signal. Altering the diffusion constant of the endogenous buffer significantly affected the propagation speed of the Ca^{2+} signal into the centre of the cell. The diffusion constant of the endogenous buffer had to be increased to 100 $\mu m^2 s^{-1}$ in order to fit the experimental data, a value five-fold larger than published values of 20 $\mu m^2 s^{-1}$ (Schmidt *et al.*, 2005). While this is consistent with the cells I have been using having a less dense cytoskeleton than those used to measure the original diffusion constant, it seems likely that other fast diffusing, small molecular weight proteins play a significant role in communicating the Ca^{2+} signal throughout the chick DRG neurone.

By comparing the modelled Ca^{2+} dynamics with and without the presences of a species representing the exogenous Ca^{2+} indicator dye, I have shown that while the inclusion of an indicator dye to observe and measure the Ca^{2+} signalling events affects the amplitude of the Ca^{2+} transients, it has very little effect on the temporal and spatial dynamics of intracellular Ca^{2+} such that measurements made using these techniques portray an accurate representation of intracellular Ca^{2+} signals.

9.3 Mitochondrial Calcium Uptake

Mitochondria have previously been reported to take up significant concentrations of cytoplasmic Ca^{2+} following Ca^{2+} influx across the plasma membrane. AM-loading chick DRG neurones with Rhod-2 AM enabled me to observe mitochondrial Ca^{2+} changes following 50 msec depolarisations of the plasma membrane. Using this in combination with patch clamping techniques removes cytosolic Rhod-2 and enabled me to introduce the Ca^{2+} indicator OG488BD into the cell.

Short plasma membrane depolarisations of both 50 msec and 1 second resulted in clear increases in fluorescence of both OG488BD and Rhod-2 signals indicating increases in intracellular and mitochondrial Ca^{2+} concentrations respectively. The areas of Rhod-2 fluorescence increases co-localised with mitotracker green positive organelles, showing that they were indeed mitochondria.

Increases of cytosolic calcium from the resting value of 129 nM to 500 nM evoked approximately four-fold increases of Rhod-2 fluorescence. As the Rhod-2 indicator dye is operating in its linear range this represents increases in mitochondrial Ca^{2+} concentration from resting levels of 250 nM to 1 μM. While these increases are not large, they will significantly increase mitochondrial metabolism (Pitter *et al.*, 2002) and therefore allow energy production to be matched to cellular energy demands.

9.3.1 Mitochondrial Substrates

The patch solution did not contain mitochondrial substrates, with the result that these and other solutes could be lost from the cell during experiments. However, with the inclusion of 5 mM pyruvate and 5 mM malate in the patch pipette depolarisation of the plasma membrane produced increases in mitochondrial Ca^{2+}, as indicated by Rhod-2 fluorescence, of comparable amplitude to those from control experiments (9 cells; data not shown).

To further confirm that the possible loss of cell constituents up the patch pipette did not affect the results, cells were depolarised within 5 seconds of going whole-cell and again after 3 minutes in the whole-cell configuration. Comparison of the two depolarisation-induced responses showed no significant differences (7 cells; data not shown).

9.3.2 Spatial Variance of Mitochondrial Calcium Uptake

Following a brief depolarisation, peripheral mitochondria take up significantly more Ca^{2+} than central ones, even though much of the uptake occurs at times when cytosolic Ca^{2+} gradients have dissipated. This result is similar to ones reported in frog sympathetic neurones (Pivovarova *et al.*, 1999) and also in HeLa cells, where release of Ca^{2+} from the endoplasmic reticulum evokes a larger uptake into peripheral than into central mitochondria, even though close contacts of the ER with mitochondria are more common

in the cell centre (Collins *et al.*, 2002). My results show that peripheral mitochondria are intrinsically more able to take up Ca^{2+}, since the mismatch persists when a uniform Ca^{2+} change is evoked by photolysis of caged Ca^{2+}. The difference between peripheral and central mitochondria cannot simply be one of membrane voltage, since the mitochondrial Ca^{2+} uptake I observe is not affected by changes of mitochondrial membrane voltage. Attempts to block the mitochondrial Ca^{2+} uptake through the uniporter following short depolarisations in chick sensory neurones using FCCP to uncouple the mitochondrial membrane resulted in no obvious changes in the mitochondrial Ca^{2+} accumulation. Similarly, blocking the uniporter with ruthenium red did not prevent increases in mitochondrial Ca^{2+} concentration. This indicates that the mitochondrial Ca^{2+} uptake is not via this pathway. I considered two other pathways, the rapid uptake mode (RaM) and the reverse mode of the sodium / Ca^{2+} exchanger. However, work by Sparagna *et al.* has shown that the RAM is blocked by 0.5 μM ruthenium red (Sparagna *et al.*, 1995) while the uptake we observe persists in 100μM ruthenium red. Specific inhibition of the exchanger with CGP37157 did not prevent the mitochondria from accumulating Ca^{2+} from the cytosol.

These results point to the existence of a novel pathway for Ca^{2+} uptake into the mitochondria. Since the uptake is not strongly affected by mitochondrial membrane voltage it is likely to be more or less electroneutral.

9.4 Modelling the Effects of Mitochondrial Calcium Uptake on Intracellular Calcium Dynamics

The mitochondrial Ca^{2+} uptake I report here may have two possible roles. A first possibility is that it represents a signal system that allows the mitochondria of the neurone cell body to adjust their metabolism to match physiologically relevant changes of electrical activity. Calcium changes of the order of those generated by tens of action potentials evoke Ca^{2+} increases in mitochondria large enough to significantly affect metabolism. The mitochondrial Ca^{2+} elevations significantly outlast the cytosolic ones, allowing mitochondria to integrate the signals and therefore adjust their energy production to the time-averaged cellular energy load.

Previous work done in other cell types has shown that the mitochondria present a significant barrier to Ca^{2+} diffusion. In the case of pancreatic acinar cells the mitochondria present a barrier preventing the spread of IP_3-induced Ca^{2+} release in the apical pole, containing the secretory granules, into the basolateral region containing the nucleus (Tinel *et al.*, 1999). In order to confirm that the mitochondrial Ca^{2+} uptake has no significant effect on the intracellular Ca^{2+} dynamics in chick sensory neurones, I included these organelles in my mathematical diffusion model.

The results from these models, simulating the mitochondrial Ca^{2+} accumulation from a 50 msec depolarisation of the plasma membrane, showed that insufficient Ca^{2+} is taken up by the mitochondria to significantly affect the intracellular Ca^{2+} dynamics.

However, I am only modelling the free mitochondrial Ca^{2+} as reported by my Rhod-2 experiments. Previous studies have shown that the mitochondria have a buffering capacity several orders of magnitude larger than for the cytosol and thus are capable of buffering very large quantities of Ca^{2+}, which would not be reported by the Rhod-2 signal (Rutter *et al.*, 1993; Gunter *et al.*, 1994). Therefore, a second possibility is that I am vastly underestimating the magnitude of the mitochondrial Ca^{2+} influx. In order to include the effect of mitochondrial Ca^{2+} buffers in my model I increasing the modelled mitochondrial Ca^{2+} uptake by several orders of magnitude. This leads to millimolar increases in mitochondrial Ca^{2+}. In order for the Rhod-2 signal to report a four-fold increase there would need to be millimolar concentrations of Ca^{2+} buffer in the mitochondria. Through this I have shown that it is possible to affect both the amplitude and propagation speed of the intracellular Ca^{2+} signal in these cells. However, the output from models run with this mitochondrial Ca^{2+} influx do not fit the experimental data obtained with OG488BD.

The final conclusion to my work is that in sharp contrast to other cell types, Ca^{2+} signals in chick sensory neurones appear to be very simple, reflecting passive diffusion modulated by mobile buffers.

APPENDIX A

DERIVATION OF THE ONE-DIMENSIONAL DIFFUSION EQUATION IN CARTESIAN COORDINATES

To describe Brownian motion mathematically, we first assume each molecule moves a distance Δx in a random direction for every time step Δt.

Hence, when considering a large population of molecules, in one time step, Δt, from t_k to t_{k+1}, the average change in the number of molecules at position *i* (Δn_i^k) is given by the probability of the molecules in the volume elements either side of element *i* moving into element *i* minus the probability of the molecules in element *i* moving into the neighbouring elements. Looking only in one-dimension, with probabilities that the molecules will move to the left or the right given by P_l and P_r respectively, Δn_i^k is given by:

$$\Delta n_i^k = n_i^{k+1} - n_i^k = P_l n_{i+1}^k - (P_l + P_r) n_i^k + P_r n_{i-1}^k$$

Equation A1

In the absence of any external fields, $P_l = P_r = ½$.

Hence

$$\Delta n_i^k = \frac{1}{2} n_{i+1}^k - n_i^k + \frac{1}{2} n_{i-1}^k$$

Equation A2

Multiplying both sides by $\frac{\Delta x^2}{\Delta t}$ allows us to rearrange the equation in terms of the diffusion constant of the molecules

$$\frac{\Delta n_i^k}{\Delta t} = \frac{\Delta x^2}{2\Delta t} \frac{n_{i+1}^k - 2n_i^k + n_{i-1}^k}{\Delta x^2}$$

Equation A3

Where the diffusion constant, $D = \frac{(\Delta x)^2}{2\Delta t}$.

The number of molecules can be converted to concentrations by dividing both sides by Avogadro's number (6.022×10^{23} mol^{-1}) and by the volume.

In the limit $\Delta x \Rightarrow 0$ and $\Delta t \Rightarrow 0$ we get the one-dimensional diffusion equation as a parabolic partial differential equation in Cartesian coordinates.

$$\frac{\partial C(x,t)}{\partial t} = D \frac{\partial^2 C(x,t)}{\partial x^2}$$

Equation A4

This can easily be extended into three dimensions to give

$$\frac{\partial C(x,y,z,t)}{\partial t} = D\left[\frac{\partial^2 C(x,y,z,t)}{\partial x^2} + \frac{\partial^2 C(x,y,z,t)}{\partial y^2} + \frac{\partial^2 C(x,y,z,t)}{\partial z^2}\right]$$

Equation A5

This is more commonly written as

$$\frac{\partial C(x,y,z,t)}{\partial t} = \nabla \cdot (D \cdot \nabla \cdot C(x,y,z,t))$$

Equation A6

Where $\nabla = \frac{\partial}{\partial x} + \frac{\partial}{\partial y} + \frac{\partial}{\partial z}$.

APPENDIX B – MODEL PARAMETERS

Geometry Definitions in The Virtual Cell

Geometries of the five exemplar cell were defined explicitly based on z-stack images. These were created as inequalities defining the outer limit of the domain, or in physiological terms the membrane enclosing the domain. The following equations were used to define the geometries of the five exemplar cells in The Virtual Cell:

120504

Plasma membrane

$$(x)^2 + (y)^2 + (z)^2 < 45$$

Nuclear membrane

$$0.0625 * \left(-0.9 - \left(100 - y^2\right)^{\frac{1}{2}} + x \right)^2 + 0.015625 * y^2 + 0.04 * z^2 < 0.5$$

240604

Plasma membrane

$$(x)^2 + (y)^2 + (z)^2 < 45$$

Nuclear membrane

$$0.4*\left(-1.5-\left(\left(112.5-y^2\right)-z^2\right)^{\frac{1}{2}}+x\right)^2+0.018*y^2+0.021*z^2<0.5$$

221204

Plasma membrane

$$\left(0.275*(x)^2+0.415*(y)^2+0.23*(z)^2<20\right)*(z>=12.86)$$

Nuclear membrane

$$\left(0.0625*\left(4.8-\left(\left(104+y^2\right)+z^2\right)^{\frac{1}{2}}+x\right)^2+0.015625*y^2+0.05*z^2<0.5\right)*(z>=14)$$

140105

Plasma membrane

$$0.31*(x)^2+0.407*(y)^2+0.24*(z)^2<15$$

Nuclear membrane

$$0.0625*\left(3.5-\left(\left(64-y^2\right)-z^2\right)^{\frac{1}{2}}+x\right)^2+0.015625*y^2+0.01*z^2<0.4$$

190105

Plasma membrane

$$\left(0.275*(x)^2+0.415*(y)^2+0.13*(z)^2<20\right)*(z>=17)$$

Nuclear membrane

$$\left(0.0625*\left(4.8-\left(\left(104+y^2\right)+z^2\right)^{\frac{1}{2}}+x\right)^2+0.015625*y^2+0.03*(-12.5-x+z)^2<0.3\right)$$
$$*(z>=18)*(z<31)$$

Influx and Efflux Parameters in The Virtual Cell

The Ca^{2+} influxes following 50 msec depolarisations were modelled using a standard exponential-based equation (equation B1).

$$I_{ca}=CaC\_Plasmalemma*A*(1-e^{-(t-1.052)*k\_on})*e^{-(t-1.052)*k\_off}*(t>1.052)*(t<=1.102)$$
$$+(A\_tail*CaC\_Plasmalemma*e^{-(t-1.103)*k\_off\_tail})*(t>=1.103)*(t<1.2)$$

Equation B1

The equation parameters were adjusted to fit the inward Ca^{2+} current measured through experiment. The parameters for each of the five exemplar cells are shown below in table B1.

Ca^{2+} removal across the plasma membrane is achieved through a population of Ca^{2+}-ATPase pumps defined by equation B2.

$$I_{pump} = CaP\_Plasmalemma * V_{max\_pump} * \frac{[Ca^{2+}]_c^{\,n}}{[Ca^{2+}]_c^{\,n} + K^n}$$

Equation B2

The rate of outpumping in each exemplar cell is controlled by one parameter, V_{max_pump}, whose value (table B1) is adjusted to fit the relevant experimental data.

Cell	CaC_Plasmalemma	A (pA)	k_{on} (s^{-1})	k_{off} (s^{-1})	A_{tail} (pA)	k_{off_tail} (s^{-1})	V_{max_pump} ($\mu M\ s^{-1}$)
120504	10	-13	2000	55	-55	1300	120
240604	10	-12	1200	80	-527	700	140
221204	10	-8	400	40	-53	800	80
14105	10	-71	1200	50	-60	570	50
190105	10	-19	800	50	-77	550	280

Table B1 Model Parameters

By convention, a negative value is used to signify an inward flux, while a positive value refers to an outwards flux.

10 BIBLIOGRAPHY

Albrecht, M. A., Colegrove, S. L., Hongpaisan, J., Pivovarova, N. B., Andrews, S. B. and Friel, D. D., 2001. Multiple modes of calcium-induced calcium release in sympathetic neurons I: attenuation of endoplasmic reticulum Ca(2+) accumulation at low [Ca(2+)]i during weak depolarization. *J-Gen-Physiol.* **118**, 83-100.

Allbritton, N. L., Meyer, T. and Stryer, L., 1992. Range of messenger action of calcium ion and inositol 1,4,5-trisphosphate. *Science.* **258**, 1812-1815.

al-Mohanna, F. A., Caddy, K. W. and Bolsover, S. R., 1994. The Nucleus is Insulated From Large Cytosolic Calcium Ion Changes. *Nature.* **367**, 745-750.

Andrade, R., Arlucea, J., Alonso, R. and Arechaga, J., 2001. Nucleoplasmin binds to nuclear pore filaments and accumulates in specific regions of the nucleolar cortex. *Chromosoma.* **109**, 545-550.

Ashby, M. C., Craske, M., Park, M. K., Gerasimenko, O. V., Burgoyne, R. D., Petersen, O. H. and Tepikin, A. V., 2002. Localized Ca2+ uncaging reveals polarized distribution of Ca2+-sensitive Ca2+ release sites: mechanism of unidirectional Ca2+ waves. *J Cell Biol.* **158**, 283-292.

Augustine, G. J., Santamaria, F. and Tanaka, K., 2003. Local Calcium Signalling in Neurons. *Neuron.* **40**, 331-346.

Ayar, A. and Scott, R., 1999. The actions of ryanodine on Ca^{2+}-activated conductances in rat cultured DRG neurones; evidence for Ca^{2+}-induced Ca^{2+} release. *Naunyn Schmiedebergs Arch Pharmacol.* **359**, 81-91.

Bading, H., Ginty, D. D. and Greenberg, M. E., 1993. Regulation of Gene Expression in Hippocampal Neurons by Distict Calcium Signaling Pathways. *Science.* **260**, 181-186.

Badminton, M. N., Campbell, A. K. and Rembold, C. M., 1996a. Differential Regulation of Nuclear and Cytosolic Ca2+ in HeLa Cells. *J Biol Chem.* **271**, 31210-31214.

Badminton, M. N., Kendall, J. M., Sala-Newby, G. and Campbell, A. K., 1995. Nucleoplasmin-Targeted Aequorin Provides Evidence for a Nuclear Calcium Barrier. *Experimental Cell Research.* **216**, 236-243.

Badminton, M. N., Sala-Newby, G., Kendall, J. M. and Campbell, A. K., 1996b. Differential regulation of nuclear and cytosolic Ca^{2+} in HeLa cells. *J Biol Chem.* **271**, 31210-31214.

Barritt, G. J., 1999. Receptor-activated Ca^{2+} inflow in animal cells: a variety of pathways tailored to meet different intracellular Ca^{2+} signalling requirements. *Biochem J.* **337**, 153-169.

Baylor, S. M. and Hollingworth, S., 1998. Model of Sarcomeric Ca^{2+} Movements, Including ATP Ca^{2+} Binding and Diffusion, during Activation of Frog Skeletal Muscle. *J Gen Physiol.* **112**, 297-316.

Bean, B. P., 2001. Calcium Channels. *Encyclopedia of Life Sciences.*

Berggård, T., Miron, S., Önnerfjord, P., Thulin, E., Åkerfeldt, K. S., Enghild, J. J., Akke, M. and Linse, S., 2002. Calbindin D_{28K} Exhibits Properties Characteristic of a Ca^{2+} Sensor. *J Biol Chem.* **19**, 16662-16672.

Bernardi, P., 1999. Mitochondrial transport of cations: channels, exchangers, and permeability transition. *Physiol Rev.* **79**, 1127-1155.
Berridge, M. J., 1993. Inositol trisphosphate and calcium signalling. *Nature.* **361**, 315-325.
Berridge, M. J., 1998. Neuronal Calcium Signaling. *Neuron.* **21**, 13-26.
Berridge, M. J., Lipp, P. and Bootman, M. D., 1999. Calcium signalling. *Current Biology.* **9**, R157-R159.
Berridge, M. J., Lipp, P. and Bootman, M. D., 2000. The Versatility and Universality of Calcium Signalling. *Molecular Cell Biology.* **1**, 11-21.
Bevan, S. and Szolcsanyi, J., 1990. Sensory neuron-specific actions of capsaicin: Mechanisms and applications. *TRENDS PHARMACOL SCI.* **11**, 330-333.
Biden, T. J., Wollheim, C. B. and Schlegel, W., 1986. Inositol 1,5,5-trisphosphate and intracellular Ca^{2+} homeostasis in clonal pituitary cells (GH3). Translocation of Ca^{2+} into mitochondria from a functionally discrete portion of the nonmitochondrial store. *J Cell Biol.* **261**, 7223-7229.
Billups, B. and Forsyhe, I. D., 2002. Presynaptic mitochondrial calcium sequestration influences transmission at mammalian central synapses. *J Neurosci.* **22**, 5840-5847.
Bolsover, S. R., Kater, S. B. and Guthrie, P. B., 1996. Spatial gradients of cytosolic calcium concentration in neurones during paradoxical activation by calcium. *Cell Calcium.* **20**, 373-379.
Bootman, M. D. and Berridge, M. J., 1995. The Elemental Principles of Calcium Signaling. *Cell.* **83**, 675-678.
Bootman, M. D., Berridge, M. J. and Roderick, H. L., 2002. Calcium Signalling: More Messengers, More Channels, More Complexity. *Current Biology.* **12**, R563-R565.
Bootman, M. D., Collins, T. J., Peppiatt, C. M., Prothero, L. S., MacKenzie, L., De Smet, P., Travers, M., Tovey, S. C., Seo, J. T., Berridge, M. J., Ciccolini, F. and Lipp, P., 2001a. Calcium Signalling - an overview. *Semin Cell Dev Biol.* **12**, 3-10.
Bootman, M. D., Lipp, P. and Berridge, M. J., 2001b. The organisation and functions of local Ca^{2+} signals. *J Cell Sci.* **114**, 213-2222.
Brand, M. D., 1985. The stoichiometry of the exchange catalysed by the mitochondrial calcium/sodium antiporter. *Biochem J.* **229**, 161-166.
Brierley, G. P., Baysal, K. and Jung, D. W., 1994. Cation transport systems in mitochondria: Na^{+} and K^{+} uniports and exchangers. *J Bioenerg Biomembr.* **26**, 519-526.
Brown, E. M. and Macloed, R. J., 2001. Extracellular calcium sensing and extracellular calcium signaling. *Physiol Rev.* **81**, 239-297.
Cancela, J. M., Coppenolle, F. V., Galione, A., Tepikin, A. V. and Petersen, O. H., 2002. Transformation of local Ca^{2+} spikes to global Ca^{2+} transients: the combinatorial roles of multiple Ca^{2+} releasing messengers. *EMBO J.* **21**, 909-919.
Carafoli, E., 1987. Intracellular calcium homeostasis. *Annu Rev Biochem.* **56**, 395-433.
Carafoli, E., 2003. Calcium - a universal carrier of biological signals. *FEBS Journal.* **272**, 1073-1089.
Catterall, W. A., 2000. Structure and regulation of voltage-gated Ca^{2+} channels. *Annu Rev Cell Dev Biol.* **16**, 521-555.

Chen, Y., Cai, J., Zhao, T., Wang, C., Dong, S., Luo, S. and Chen, Z. W., 2005. Atomic force microscopy imaging and 3-D reconstruction of thin sections of a single cell and its interior structures. *Ultramicroscropy*. **103**, 173-182.

Chin, D. and Means, A. R., 2000. Calmodulin: a prototypical calcium sensor. *TRENDS Cell Biol.* **10**, 322-328.

Churchill, G. C., Okada, Y., Thomas, J. M., Genazzani, A. A., Patel, S. and Galione, A., 2002. NAADP Mobilizes Ca^{2+} from Reserve Granules, Lysosome-Related Organelles, in Sea Urchin Eggs. *Cell.* **111**, 703-708.

Clapham, D. E., 1995. Calcium Signalling. *Cell.* **80**, 259-268.

Colegrove, S. L., Albrecht, M. A. and Friel, D. D., 2000. Dissection of Mitochondrial Ca^{2+} Uptake and Release Fluxes In Situ after Depolarization-evoked $[Ca^{2+}]_i$ Elevations in Sympathetic Neurons. *J Gen Physiol.* **115**, 351-369.

Collins, T. J., Berridge, M. J., Lipp, P. and Bootman, M. D., 2002. Mitochondria are morphologically and functionally heterogeneous within cells. *EMBO J.* **21**, 1616-1627.

Collins, T. J., Lipp, P., Berridge, M. J. and Bootman, M. D., 2001. Mitochondrial Ca^{2+} uptake depends on the spatial and temporal profile of cytosolic Ca^{2+} signals. *J Biol Chem.* **276**, 26411-26420.

Crompton, M., Kunzi, M. and Carafoli, E., 1977. The calcium-induced and sodium-induced effluxex of calcium from heart mitochondria. Evidence for a sodium-calcium carrier. *Eur J Biochem.* **79**, 549-558.

Deisseroth, K., Heist, E. K. and Tsien, R. W., 1998. Translocation of calmodulin to the nucleus supports CREB phosphorylation in hippocampal neurons. *Nature.* **392**, 198-202.

Denton, R. M., Richards, D. A. and Chin, J. G., 1978. Calcium ions and the regulation of NAD^+-linked isocitrate dehydrogenase from the mitochondria of rat heart and other tissues. *Biochem J.* **176**, 899-906.

Denton, R. R., Randle, P. J. and Martin, B. R., 1972. Stimulation by calcium ions of pyruvate dehydrogenase phosphate phosphatase. *Biochem J.* **128**, 161-163.

Desmadryl, G., Chambard, J. M., Valmier, J. and Sans, A., 1997. Multiple Voltage-Dependent Calcium Currents in Acutely Isolated Mouse Vestibular Neurons. *Neuroscience.* **78**, 511-522.

Desmadryl, G., Hilaire, C., Vigues, S., Diochot, S. and Valmier, J., 1998. Developmental regulation of T-, N- and L-type calcium currents in mouse embryonic sensory neurones. *Eur J Neurosci.* **10**, 545-552.

Dhalla, N. S., 1969. Excitation-contraction coupling in heart. I. Comparison of calcium uptake by the sarcoplasmic reticulum and mitochondria of the rat heart. *Arch Int Physiol Biochem.* **77**, 916-934.

Diochot, S., Richard, S. and Valmier, J., 1995. Diversity of Voltage-Gated Calcium Currents in Large Diameter Embryonic Mouse Sensory Neurons. *Neuroscience.* **69**, 627-641.

Dolman, N. J., Gerasimenko, J. V., Gerasimenko, O. V., Voronina, S. G., Petersen, O. H. and Tepikin, A. V., 2005. Stable Golgi-Mitochondria Complexes and Formation of Golgi Ca^{2+} Gradients in Pancreatic Acinar Cells. *J Biol Chem.* **280**, 15794-15799.

Dolmetsch, R. E., Pajvani, U., Fife, K., Spotts, J. M. and Greenberg, M. E., 2001. Signaling to the Nucleus by an L-type Calcium Channel-Calmodulin Complex Through the MAP Kinase Pathway. *Science.* **294**, 333-339.

Dolphin, A. C., 2001. Calcium Channel Diversity. *Encyclopedia of Life Sciences.*

Duchen, M. R., 1992. Ca^{2+}-dependent changes in the mitochondrial energetics of single mouse sensory neurones. *Biochem J.* **283**, 41-50.

Duchen, M. R., 2000. Mitochondria and calcium: from cell signalling to cell death. *J Physiol.* **529**, 57-68.

Eberhard, M. and Erne, P., 1994. Calcium and magnesium binding to rat parvalbumin. *FEBS Journal.* **222**, 21-26.

Fields, R. D., Eshete, F., Stevens, B. and Itoh, K., 1997. Action potential-dependent regulation of gene expression: temporal specificity in Ca^{2+}, cAMP-responsive element binding proteins, and mitogen-activated protein kinase signaling. *J Neurosci.* **17**, 7252-7266.

Fiskum, G. and Lehninger, A. L., 1979. Regulated release of Ca^{2+} from respiring mitochondria by $Ca^{2+}/2H^{+}$ antiport. *J Biol Chem.* **254**, 6236-6239.

Fox, A. P., Nowycky, M. C. and Tsien, R. W., 1987a. Kinetic and pharmacological properties distinguishing three types of calcium current in chick sensory neurones. *J Physiol.* **394**, 149-172.

Fox, A. P., Nowycky, M. C. and Tsien, R. W., 1987b. Single-channel recordings of three types of calcium channels in chick sensory neurones. *J Physiol.* **394**, 173-200.

Friel, D. D., 1995. $[Ca^{2+}]_i$ oscillations in sympathetic neurons: an experimental test of a theoretical model. *Biophys J.* **68**, 1752-1766.

Friel, D. D., 2000. Mitochondria as regulators of stimulus-evoked calcium signals in neurons. *Cell Calcium.* **28**, 307-316.

Friel, D. D. and Tsien, R. W., 1992. A Caffeine- and Ryanodine-sensitive Ca^{2+} Store in Bullfrog Sympathetic Neurones Modulates Effects of Ca^{2+} Entry on $[Ca^{2+}]i$. *Journal of Physiology.* **450**, 217-246.

Friel, D. D. and Tsien, R. W., 1994. An FCCP-sensitive Ca^{2+} store in bullfrog sympathetic neurons and its participation in stimulus-evoked changes in $[Ca^{2+}]_i$. *J Neurosci.* **14**, 4007-4024.

Genka, C., Ishida, H., Ichimori, K., Hirota, Y., Tanaami, T. and Nakazawa, H., 1999. Visualization of biphasic Ca2+ diffusion from cytosol to nucleus in contracting adult rat cardiac myocytes with an ultra-fast confocal imaging system. *CELL CALCIUM.* **25**, 199-208.

Gerasimenko, O. V., Gerasimenko, J. V., Tepikin, A. V. and Petersen, O. H., 1995. ATP-dependent accumulation and inositol trisphosphate- or cyclic ADP-ribose-mediated release of Ca^{2+} from the nuclear envelope. *Cell.* **80**, 439-444.

Gerasimenko, O. V., Gerasimenko, J. V., Tepikin, A. V. and Petersen, O. H., 1996. Calcium transport pathways in the nucleus. *Pflugers Arch.* **432**, 1-6.

Gil, A., Segura, J., Pertusa, J. A. G. and Soria, B., 2000. Monte Carlo Simulation of 3-D Buffered Ca^{2+} Diffusion in Neuroendocrine Cells. *Biophysical Journal.* **78**, 13-33.

Gold, S. L. M., 2005. Intracellular calcium regulation among subpopulations of rat DRG neurons. *American Pain Society, Boston 2005*, Poster #608.

Greber, U. F. and Gerace, L., 1995. Depletion of calcium from the lumen of the endoplasmic reticulum reversibly inhibits passive diffusion and signal-mediated transport into the nucleus. *J Cell Biol.* **128**, 5-14.

Griffiths, E. J., 1999. Reversal of mitochondrial Na/Ca exchange during metabolic inhibition in rat cardiomyocytes. *FEBS Letters.* **453**, 400-404.

Gunter, T. E., Gunter, K. K., Sheu, S. S. and Gavin, C. E., 1994. Mitochondrial calcium transport: physiological and pathological relevance. *Am J Physiol.* **267**, C313-339.

Gunter, T. E. and Pfeiffer, D. R., 1990. Mechanisms by which mitochondria transport calcium. *Am J Physiol Cell Physiol.* **258**, C755-C786.

Hamill, O. P., Marty, A., Neher, E., Sakmann, B. and Sigworth, F. J., 1981. Improved patch-clamp techniques for high-resolution current recording from cells and cell-free membrane patches. *Pflugers Arch.* **391**, 85-100.

Hardingham, G. E., Chawla, S., Johnson, C. M. and Bading, H., 1997. Distinct functions of nuclear and cytoplasmic calcium in the control of gene expression. *Nature.* **385**, 260-265.

Harris, E. J. and Berent, C., 1969. Calcium ion-induced uptakes and transformations of substrates in liver mitochondria. *Biochem J.* **115**, 645-652.

Haynes, L. P., Tepikin, A. V. and Burgoyne, R. D., 2004. Calcium-binding protein 1 is an inhibitor of agonist-evoked, inositol 1,4,5-trisphosphate-mediated calcium signaling. *J Biol Chem.* **279**, 547-555.

Heinemann, S. H., 2001. Sodium, Calcium and Potassium Channels. *Encyclopedia of Life Sciences.*

Heytler, P. G. and Prichard, W. W., 1962. A new class of uncoupling agents--carbonyl cyanide phenylhydrazones. *Biochem Biophys Res Commun.* **7**, 272-275.

Hilgemann, D. W., Feng, S. and Nasuhoglu, C., 2001. The Complex and Intriguing Lives of PIP_2 with Ion Channels and Transporters. *Sci STKE.* **111**, RE19.

Hofer, A. M., 2005. Another dimension to calcium signaling: a look at extracellular calcium. *J Cell Sci.* **118**, 855-862.

Hofer, A. M. and Brown, E. M., 2003. Extracellular calcium sensing and signalling. *Nat Rev Mol Cell Biol.* **4**, 530-538.

Holliday, J., Adams, R. J., Sejnowski, T. J. and Spitzer, N. C., 1991. Calcium Induced Release of Calcium Regulates Differentiation of Cultured Spinal Neurons. *Neuron.* **7**, 787-796.

Honda, C. N., 1995. Differential distribution of calbindin-D28k and parvalbumin in somatic and visceral sensory neurons. *Neuroscience.* **68**, 883-892.

Hongpaisan, J., Pivovarova, N. B., Colegrove, S. L., Leapman, R. D., Friel, D. D. and Andrews, S. B., 2001. Multiple modes of calcium-induced calcium release in sympathetic neurons II: A $[Ca^{2+}]_i$ - and location-dependent transition from endoplasmic reticulum calcium accumulation to net calcium release. *J-Gen-Physiol.* **118**, 83-100.

Hou, T. T., Johnson, J. D. and Rall, J. A., 1992. Effect of temperature on relaxation rate and Ca^{2+}, Mg^{2+} dissociation rates from parvalbumin of frog muscles fibres. *J Physiol.* **449**, 399-410.

Huang, W. C. and Chueh, S. H., 1996. Calcium mobilization from the intracellular mitochondrial and nonmitochondrial stores of the rat cerebellum. *Brain Res.* **718**, 151-158.

Jacobson, J. and Duchen, M. R., 2004. Interplay between mitochondria and cellular calcium signalling. *Molecular and Cellular Biochemistry.* **256/257**, 209-218.

Johnson, P. R., Tepikin, A. V. and Erdemli, G., 2002. Role of mitochondria in Ca^{2+} homeostasis of mouse pancreatic acinar cells. *Cell Calcium.* **32**, 59-69.

Jouaville, L. S., Ichas, F., Holmuhamedov, E. L., Camacho, P. and Lechleiter, J. D., 1995. Synchronization of calcium waves by mitochondrial substrates in Xenopus laevis oocytes. *Nature.* **377**, 438-441.

Jouaville, L. S., Pinton, P., Bastianutto, C., Rutter, G. A. and Rizzuto, R., 1999. Regulation of mitochondrial ATP synthesis by calcium: evidence for a long-term metabolic priming. *Proc Natl Acad Sci.* **96**, 13807-13812.

Kasai, H. and Petersen, O. H., 1994. Spatial dynamics of second messengers: IP3 and cAMP as long-range and associative messengers. *TRENDS in Neurosciences.* **17**, 95-101.

Kennedy, H. J. and Meech, R. W., 2002. Fast Ca^{2+} Signals at Mouse Inner Hair Cell Synapse: a Role for Ca^{2+}-induced Ca^{2+} Release. *Journal of Physiology.* **539**, 12-23.

Klingauf, J. and Neher, E., 1997. Modeling buffered Ca^{2+} diffusion near the membrane: implications for secretion in neuroendocrine cells. *Biophysical Journal.* **72**, 674-690.

Kosk-Kosicka, D. and Inesi, G., 1985. Cooperative calcium binding and calmodulin regulation in the calcium-dependent adenosine triphosphatase purified from the erythrocyte membrane. *FEBS-lett.* **189**, 67-71.

Lacinova, L. and Hofmann, F., 2005. Ca^{2+}- and voltage-dependent inactivation of the expressed L-type $Ca_v1.2$ calcium channel. *Archives of Biochemistry and Biophysics.* **437**, 42-50.

Lehninger, A. L., 1969. Acid-base changes in mitochondria and medium during energy-dependent and energy independent binding of Ca^{2+}. *Annal NY Acad Sci.* **147**, 816-823.

Li, Y. N., Sakamoto, H., Kawate, T., Cheng, C. X., Li, Y. C., Shimada, O. and Atsumi, S., 2005. An immunocytochemical study of calbindin-D28K in laminae I and II of the dorsal horn and spinal ganglia in the chicken with special reference to the relation to substance P-containing primary afferent neurons. *Arch Histol Cytol.* **68**, 27-70.

Lide, D. R., 1993-1994. Diffusion coefficients of strong electrolytes., Handbook of Chemistry and Physics. Boca Raton. FL: CRC Press, pp. 5-90.

Lipp, P. and Niggli, E., 1994. Sodium current-induced calcium signals in isolated guinea-pig ventricular myocytes. *J Physiol.* **474**, 439-446.

Lipp, P., Thomas, D., Berridge, M. J. and Bootman, M. D., 1997. Nuclear calcium signalling by individual cytoplasmic calcium puffs. *EMBO J.* **16**, 7166-7173.

Llano, I., Dipolo, R. and Marty, A., 1994. Calcium-induced Calcium Release in Cerebellar Purkinje Cells. *Neuron.* **12**, 663-673.

Loew, L. M. and Schaff, J. C., 2001. The Virtual Cell: a software environment for computational cell biology. *TRENDS in Biotechnology.* **19**, 401-406.

Luebke, J. I., Dunlap, K. and Turner, T. J., 1993. Multiple calcium channel types control glutamatergic synaptic transmission in the hippocampus. *Neuron.* **11**, 895-902.

Lytton, J., Westlin, M., Burk, S. E., Shull, G. E. and MacLennan, D. H., 1992. Functional comparisons between isoforms of the sarcoplasmic or endoplasmic reticulum family of calcium pumps. *J Biol Chem.* **267**, 14483-14489.

Mahoney, M., Slakey, L., Hepler, P. and Gross, D., 1993. Independent modes of propagation of calcium waves in smooth muscle cells. *J Cell Sci.* **104**, 1101-1107.

Markram, H., Roth, A. and Helmchen, F., 1998. Competitive calcium binding: implications for dendritic calcium signaling. *J Comput Neurosci.* **5**, 331-348.

McDonough, S. I., Cseresnyes, Z. and Schneider, M. F., 2000. Origin Sites of Calcium Release and Calcium Oscillations in Frog Sympathetic Neurons. *J Neurosci.* **20**, 9059-9070.

McLain, R. F. and Weinstein, J. N., 1993. Morphometric model of normal rabbit dorsal root ganglia. *Spine.* **18**.

Mermelstein, P. G., Deisseroth, K., Dasgupta, N., Isaksen, A. L. and Tsien, R. W., 2001. Calmodulin priming: nuclear translocation of a calmodulin complex and the memory of prior neuronal activity. *Proc Natl Acad Sci.* **98**, 15342-15347.

Meyer, T., Holowka, D. and Stryer, L., 1988. Highly cooperative opening of calcium channels by inositol 1,4,5-trisphosphate. *Science.* **240**, 653-656.

Meyer, T. and Stryer, L., 1988. Molecular model for receptor-stimulated calcium spiking. *Proc Natl Acad Sci.* **85**, 5051-5055.

Milikan, J. M., Carter, T. D., Horne, J. H., Tzortzopoulos, A., Török, K. and Bolsover, S. R., 2002. Integration of calcium signals by calmodulin in rat sensory neurons. *European Journal of Neuroscience.* **15**, 661-670.

Mitchell, P., 1961. Coupling of phosphorylation to electron and hydrogen transfer by a chemiosmotic type of mechanism. *Nature.* **191**, 144-148.

Murchison, D., Zawieja, D. C. and Griffith, W. H., 2003. Reduced mitochondrial buffering of voltage-gated calcium influx in aged rat basal froebrain neurons. *Cell Calcium.* **36**, 61-75.

Nägerl, U. V., Novo, D., Mody, I. and Vergara, J. L., 2000. Binding Kinetics of Calbindin-D_{28k} Determined by Flash Photolysis of Caged Ca^{2+}. *Biophys J.* **79**, 3009-3018.

Naraghi, M. and Neher, E., 1997. Linearized buffered Ca^{2+} diffusion in microdomains and its implications for calculation of $[Ca^{2+}]$ at the mouth of a calcium channel. *J Neurosci.* **17**, 6961-6973.

Nathanson, M. H., Burgstahler, A. D. and Fallon, M. B., 1994. Multistep mechanism of polarized Ca2+ wave patterns in hepatocytes. *Am J Physiol Gastrointest Liver Physiol.* **267**, G338-349.

Neher, E. and Augustine, G. J., 1992. Calcium gradients and buffers in bovine chromaffin cells. *J Physiol.* **450**, 273-301.

Neher, E. and Sakmann, B., 1976. Single-channel currents recorded from membrane of denervated frog muscle fibres. *Nature.* **260**, 799-801.

Nowycky, M. C., Fox, A. P. and Tsien, R. W., 1985. Three types of neuronal calcium channel with different calcium agonist sensitivity. *Nature.* **316**, 440-443.

Nowycky, M. C. and Pinter, M. J., 1993. Time courses of calcium and calcium-bound buffers following calcium influx in a model cell. *Biophysical Journal.* **64**, 77-91.

Park, M. K., Ashby, M. C., Erdemli, G., Petersen, O. H. and Tepikin, A. V., 2001. Perinuclear, perigranular and sub-plasmalemmal mitochondria have distinct functions in the regulation of cellular calcium transport. *EMBO-J.* **20**.

Perez Terzic, C., Pyle, J., Jaconi, M., Stehno Bittel, L. and Clapham, D. E., 1996. Conformational states of the nuclear pore complex induced by depletion of nuclear Ca2+ stores. *Science.* **273**, 1875-1877.

Perkins, G., Renken, C., Martones, M. E., Young, S. J., Ellisman, M. and Frey, T., 1997. Electron Tomography of Neuronal Mitochondria: Three-Dimensional Structure and Organization of Cristae and Membrane Contacts. *J Struct Biol.* **119**, 260-272.

Peters, R., 2005. Translocation Through the Nuclear Pore Complex: Selectivity and Speed by Reduction-of-Dimensionality. *Traffic.* **6**, 421-427.

Petersen, O. H. and Cancela, J. M., 1999. New Ca^{2+}-releasing messengers: are they important in the nervous system? *TRENDS in Neurosciences.* **22**, 488-494.

Petersen, O. H., Petersen, C. C. H. and Kasai, H., 1994. Calcium and hormone action. *Annual Review of Physiology.* **56**, 297-319.

Petersen, O. H., Tepikin, A. V. and Park, M. K., 2001. The endoplasmic reticulum: one continuous or several separate Ca^{2+} stores? *TRENDS in Neurosciences.* **24**, 271-276.

Pinton, P., Brini, M., Bastianutto, C., Tuft, R. A., Pozzan, T. and Rizzuto, R., 1998a. New light on mitochondrial calcium. *Biofactors.* **8**, 243-253.

Pinton, P., Pozzan, T. and Rizzuto, R., 1998b. The Golgi apparatis is an inositol 1,4,5-trisphosphate-sensitive Ca^{2+} store, with functional properties distinct from those of the endoplasmic reticulum. *EMBO J.* **17**, 5298-5308.

Pitter, J. G., Maechler, P., Wollhein, C. B. and Spat, A., 2002. Mitochondria respond to Ca^{2+} already in the submicromolar range: correlation with redox sate. *Cell Calcium.* **31**, 97-104.

Pivovarova, N. B., Hongpaisan, J., Andrews, S. B. and Friel, D. D., 1999. Depolarization-Induced Mitochondrial Ca^{2+} Accumulation in Sympathetic Neurons: Spatial and Temporal Characteristics. *Journal of Neuroscience.* **19**, 6372-6384.

Pumain, R. and Heinemann, U., 1985. Stimulus- and amino acid-induced calcium and potassium changes in rat neocortex. *J Neurophysiol.* **53**, 1-16.

Putney, J. W., Jr., 1998. Calcium Signaling: Up, Down, Up, Down...What's the Point? *Science.* **279**, 191-192.

Reder, C., 1988. Metabolic control theory: a structural approach. *J Theor Biol.* **135**, 175-201.

Redmond, L. and Ghosh, A., 2005. Regulation of dendritic development by calcium signaling. *Cell Calcium.* **37**, 411-416.

Ribbeck, K. and Gorlich, D., 2001. Kinetic analysis of translocation through nuclear pore complexes. *EMBO J.* **20**, 1320-1330.

Ringer, S., 1883. A further contribution regarding the influence of the different constituents of the blood on the contraction of the heart. *J Physiol.* **4**, 29-43.

Rintoul, G. L., Raymond, L. A. and Baimbridge, K. G., 2001. Calcium buffering and protection from excitotoxic cell death by exogenous calbindin-D28k in HEK 293 cells. *Cell Calcium.* **29**, 277-287.

Rizzuto, R., 2001. Intracellular Ca^{2+} Pools in Neuronal Signalling. *Current Opinion in Neurobiology.* **11**, 306-311.

Rizzuto, R., Bernardi, P. and Pozzan, T., 2000. Mitochondria as all-round players of the calcium game. *J Physiol.* **529**, 37-47.

Rizzuto, R., Brini, M., Murgia, M. and Pozzan, T., 1993. Microdomains with high Ca^{2+} close to IP_3-sensitive channels that are sensed by neighbouring mitochondria. *Science.* **262**, 744-747.

Rizzuto, R., Duchen, M. R. and Pozzan, T., 2004. Flirting in Little Space: The ER/Mitochondria Ca^{2+} Liaison. *Sci STKE.* **215**.

Rossi, C. S., Carafoli, E. and Lehninger, A. L., 1967. Active ion transport by mitochondria. *Protoplasma.* **63**, 90-94.

Rutter, G., Theler, J., Murgia, M., Wollheim, C., Pozzan, T. and Rizzuto, R., 1993. Stimulated Ca2+ influx raises mitochondrial free Ca2+ to supramicromolar levels in a pancreatic beta-cell line. Possible role in glucose and agonist-induced insulin secretion. *J Biol Chem.* **268**, 22385-22390.

Sala, F. and Hernández-Cruz, A., 1990. Calcium diffusion modelling in a spherical neuron. Relevance of buffering properties. *Biophysical Journal.* **57**, 313-324.

Satoh, H., Hayashi, H., Blatter, L. A. and Bers, D. M., 1997. BayK 8644 increases resting calcium spark frequency in ferret ventricular myocytes. *Heart Vessels.* **12**, 58-61.

Scarpa, A. and Graziotti, P., 1973. Mechanisms for intracellular calcium regulation in heart. I. Stopped-flow measurements of Ca^{2+} uptake by cardiac mitochondria. *J Gen Physiol.* **62**, 756-772.

Schaff, J. C., Slepchenko, B. M., Choi, Y. S., Wagner, J., Resasco, D. and Loew, L. M., 2001. Analysis of nonlinear dynamics on arbitrary geometries with The Virtual Cell. *Chaos.* **11**, 115-131.

Schatten, G. and Thoman, M., 1978. Nuclear Surface Complex as Observed With the High Resolution Scanning Electron Microscope. *J Cell Biol.* **77 (2)**, 517-535.

Schmidt, H., Brown, E. B., Schwaller, B. and Eilers, J., 2003. Diffusional mobility of parvalbumin in spiny dendrites of cerebellar Purkinje neurons quantified by fluorescence recovery after photobleaching. *Biophys J.* **84**, 2599-2608.

Schmidt, H., Schwaller, B. and Eilers, J., 2005. Calbindin D28K targets *myo*-inositol monophosphatase in spines and dendrites of cerebellar Purkinje neurons. *PNAS.* **102**, 5850-5855.

Schwaller, B., 2001. Calcium-binding Proteins. *Encyclopedia of Life Sciences.*

Schwamborn, K., Albig, W. and Doenecke, D., 1998. The Histone $H1^{\circ}$ Contains Multiple Sequence Elements for Nuclear Targeting. *Experimental Cell Research.* **244**, 206-217.

Selles, J. and Boland, R. L., 1990. In vitro calcium transport properties of skeletal muscle mitochondria from vitamin D-deficient and 1,25-dihydroxy-vitaminD3-treated chicks. *Calcif Tissue Int.* **47**, 46-50.

Shaywitz, A. J. and Greenberg, M. E., 1999. CREB: A Stimulus-Induced Transcription Factor Activated By A Diverse Array Of Extracellular Signals. *Annu Rev Biochem.* **68**, 821-861.

Shears, S. B. and Kirk, C. J., 1984. Determination of mitochondrial calcium content in hepatocytes by a rapid cellular fractionation technique. Vasopressin stimulates mitochondrial Ca^{2+} uptake. *Biochem J.* **220**, 417-421.

Shishkin, V., Potapenko, E., Kostyuk, E., Girnyk, O., Voitenko, N. and Kostyuk, P., 2002. Role of mitochondria in intracellular calcium signaling in primary and secondary sensory neurones of rats. *Cell Calcium.* **32**, 121-130.

Shmigol, A., Kostyuk, P. and Verkhratsky, A., 1995a. Dual Action of Thapsigargin on Calcium Mobilization in Sensory Neurons: Inhibition of Ca^{2+} Uptake by Caffeine-sensitive Pools and Blockade of Plasmalemmal Ca^{2+} Channels. *Neuroscience.* **65**, 1109-1118.

Shmigol, A., Svichar, N., Kostyuk, P. and Verkhratsky, A., 1996. Gradual Caffeine-induced Ca^{2+} release in Mouse Dorsal Root Ganglion Neurones is Controlled by Cytoplasmic and Luminal Ca^{2+}. *Neuroscience.* **73**, 1061-1067.

Shmigol, A., Verkhratsky, A. and Isenberg, G., 1995b. Calcium-induced Calcium Release in Rat Sensory Neurons. *Journal of Physiology.* **489**, 627-636.

Sidky, A. O. and Baimbridge, K. G., 1997. Calcium homeostatic mechanisms operating in cultured postnatal rat hippocampal neurons following flash photolysis of nitrophenyl-EGTA. *J Physiol.* **504**, 579-590.

Slepchenko, B. M., Schaff, J. C. and Choi, Y. S., 2000. Numerical Approach to Fast Reactions in Reaction-Diffusion Systems: Application to Buffered Calcium Waves in Bistable Models. *J Comp Physics.* **162**, 186-218.

Slepchenko, B. M., Schaff, J. C., Macara, I. and Loew, L. M., 2003. Quantitative cell biology with The Virtual Cell. *TRENDS in Cell Biology.* **13**, 570 - 576.

Smets, I., Caplanusi, A., Despa, S., Molnar, Z., Radu, M., vandeVen, M., Ameloot, M. and Steels, P., 2004. Ca2+ uptake in mitochondria occurs via the reverse action of the Na+/Ca2+ exchanger in metabolically inhibited MDCK cells. *Am J Physiol Renal Physiol.* **286**, F784-794.

Snow, D. M., Atkinson, P. B., Hassinger, T. D., Letourneau, P. C. and Kater, S. B., 1994. Chondroitin Sulfate Proteoglycan Elevates Cytoplasmic Calcium in DRG Neurons. *Developmental Biology.* **166**, 87-100.

Solà, C., Barrón, S., Tusell, J. M. and Serratosa, J., 2001. The Ca^{2+}/calmodulin system in neuronal hyperexcitability. *The International Journal of Biochemistry & Cell Biology.* **33**, 439-455.

Sparagna, G. C., Gunter, K. K., Sheu, S. S. and Gunter, T. E., 1995. Mitochondrial Calcium Uptake from Physiological-type Pulses of Calcium. *J Biol Chem.* **270**, 27510-27515.

Stehno Bittel, L., Perez Terzic, C. and Clapham, D. E., 1995. Diffusion across the nuclear envelope inhibited by depletion of the nuclear Ca2+ store. *Science.* **270**, 1835-1838.

Strübing, C. and Clapham, D. E., 1999. Active nuclear import and export is independent of lumenal Ca2+ stores in intact mammalian cells. *Journal of General Physiology.* **113**, 239-248.

Szabadkai, G., Pitter, J. G. and Spät, A., 2001. Cytoplasmic Ca^{2+} at low submicromolar concentration stimulates mitochondrial metabolism in rat luteal cells. *Pflugers Arch.* **441**, 678-685.

Thastrup, O., Cullen, P., Drøbak, B., Hanley, M. and Dawson, A., 1990. Thapsigargin, a tumour promoter, discharges intracellular Ca^{2+} store by specific inhibition of the endoplasmic reticulum. *Biochemistry.* **87**, 2466-2470.

Thayer, S. A. and Miller, R. J., 1990. Regulation of the intracellular free calcium concentration in single rat dorsal root ganglion neurones in vitro. *J Physiol.* **425**, 85-115.

Tinel, H., Cancela, J. M., Mogami, H., Gerasimenko, J. V., Gerasimenko, O. V., Tepikin, A. V. and Petersen, O. H., 1999. Active mitochondria surrounding the pancreatic acinar granule region prevent spreading of inositol trisphosphate-evoked local cytosolic Ca^{2+} signals. *EMBO J.* **18**, 4999-5008.

Tovey, S. C., Smet, P., Lipp, P., Thomas, D., Young, K. W., Missiaen, L., De Smedt, H., Parys, J. B., Berridge, M. J., Thuring, J., Holmes, A. and Bootman, M. D., 2001. Calcium puffs are generic InsP(3)-activated elementary calcium signals and are downregulated by prolonged hormonal stimulation to inhibit cellular calcium responses. *J Cell Sci.* **114**, 3979-3989.

Tsien, R. Y., Pozzan, T. and Rink, T. J., 1982. Calcium Homeostasis in Intact Lymphocytes: Cytoplasmic Free Calcium Monitored With a New, Intracellularly Trapped Fluorescent Indicator. *J Cell Biol.* **94**, 325-334.

Usachev, Y., Schmigol, A., Pronchuk, N., Kostyuk, P. and Verkhratsky, A., 1993a. Caffeine-induced calcium release from internal stores in cultured rat sensory neurons. *Neuroscience.* **57**, 845-859.

Usachev, Y., Shmigol, A., Pronchuk, N., Kostyuk, P. and Verkhratsky, A., 1993b. Caffeine-induced Calcium Release from Internal Stores in Cultured Rat Sensory Neurons. *Neuroscience.* **57**, 845-859.

Varadi, A., Cirulli, V. and Rutter, G. A., 2004. Mitochondrial localization as a determinant of capacitative Ca^{2+} entry in HeLa cells. *Cell Calcium.* **36**, 499-508.

Verkhratsky, A. and Shmigol, A., 1996. Calcium-induced Calcium Release in Neurons. *Cell-Calcium.* **19**, 1-14.

Villalobos, C., Nunez, L., Montero, M., Garcia, A. G., Alonso, M. T., Chamero, P., Alvarez, J. and Garcia-Sancho, J., 2002. Redistribution of Ca^{2+} among cytosol and organella during stimulation of bovine chromaffin cells. *FASEB J.* **16**, 343-353.

Wagner, J. and Keizer, J., 1994. Effects of rapid buffers on Ca^{2+} diffusion and Ca^{2+} oscillations. *Biophys J.* **67**, 447-456.

Walther, T. C., Alves, A., Pickersgill, H., Loiodice, I., Hetzer, M., Galy, V., Hulsmann, B. B., Kocher, T., Wilm, M. and Allen, T., 2003. The Conserved Nup107-160 Complex Is Critical for Nuclear Pore Complex Assembly. *Cell.* **113**, 195-206.

Wanaverbecq, N., Marsh, S. J., Al-Qatari, M. and Brown, D. A., 2003. The plasma membrane calcium-ATPase as a major mechanism for intracellular calcium regulation in neurones from the rat superior cervical ganglion. *J Physiol.* **550.1**, 83-101.

Wanaverbecq, N., Marsh, S. J. and Brown, D. A., 2001. Dominant role for the plasma membrane calcium pump in calcium extrusion from rat sympathetic neurons. Society for Neuroscience Abstracts. Proceedings of the Society for Neuroscience Annual Meeting, San Diego, 27, pp. Program Number 707.713.

Wang, G. J. and Thayer, S. A., 2002. NMDA-Induced Calcium Loads Recycle Across the Mitochondrial Inner Membrane of Hippocampal Neurons in Culture. *J Neurophysiol.* **87**, 740-749.

Wang, H. and Clapham, D., 1999. Conformational Changes of the in Situ Nuclear Pore Complex. *Biophysical Journal.* **77**, 241-247.

Wei, X., Henke, V. G., Strübing, C., Brown, E. B. and Clapham, D. E., 2003. Real-time imaging of nuclear permeation by EGFP in single intact cells. *Biophys J.* **84**, 1317-1327.

Winslow, J. L., Duffy, S. N. and Charlton, M. P., 1994. Homosynaptic facilitation of transmitter release in crayfish is not affected by mobile calcium chelators: implications for the residual ionized calcium hypothesis from electrophysiological and computational analyses. *J Neurophysiol.* **72**, 1769-1793.

Yang, J., McBride, S., Mak, D., -O., Vardi, N., Palczewski, F. H. and Foskett, J. K., 2002. Identification of a family of calcium sensors as protein ligands of inositol trisphophate receptor Ca^{2+} release channels. *Proc Natl Acad Sci.* **99**, 7711-7716.

Zador, A. and Koch, C., 1994. Linearized models of calcium dynamics: formal equivalence to the cable equation. *J Neurosci.* **14**.

Zador, A., Koch, C. and Brown, T., 1990. Biophysical Model of a Hebbian Synapse. *PNAS.* **87**, 6718-6722.

Zenisek, D. and Matthews, G., 2000. The role of mitochondria in presynaptic calcium handling at a ribbon synapse. *Neuron.* **25**, 229-237.

Zimmermann, B., 2000. Control of $InsP_3$-induced Ca^{2+} oscillations in permeabilized blowfly salivary gland cells: contribution of mitochondria. *J Physiol (Lond).* **525.3**, 707-719.

Zimprich, F., Torok, K. and Bolsover, S. R., 1995. Nuclear calmodulin responds rapidly to calcium influx at the plasmalemma. *Cell Calcium.* **17**, 233-238.

Zühlke, R. D., Pitt, G. S., Deisseroth, K., Tsien, R. W. and Reuter, H., 1999. Calmodulin supports both inactivation and facilitation of L-type calcium channels. *Nature.* **399**, 159-162.